Near-surface transport of polymer solutions and time-dependent soft microfluidics

Gabriel Guyard

▶ **To cite this version:**

Gabriel Guyard. Near-surface transport of polymer solutions and time-dependent soft microfluidics. Soft Condensed Matter [cond-mat.soft]. Université Paris-Saclay, 2022. English. NNT : 2022UP-ASP142 . tel-03990347

HAL Id: tel-03990347

https://theses.hal.science/tel-03990347v1

Submitted on 15 Feb 2023

HAL is a multi-disciplinary open access archive for the deposit and dissemination of scientific research documents, whether they are published or not. The documents may come from teaching and research institutions in France or abroad, or from public or private research centers.

L'archive ouverte pluridisciplinaire **HAL**, est destinée au dépôt et à la diffusion de documents scientifiques de niveau recherche, publiés ou non, émanant des établissements d'enseignement et de recherche français ou étrangers, des laboratoires publics ou privés.

université PARIS-SACLAY

Near-surface transport of polymer solutions and time-dependent soft microfluidics

Transport interfacial de polymères en solution et dynamique en microfluidique déformable

Thèse de doctorat de l'université Paris-Saclay

École doctorale n° 564: Physique en Île-de-France – EDPIF
Spécialité de doctorat: Physique
Graduate School : Physique. Référent : Faculté des Sciences d'Orsay

Thèse préparée dans les unités de recherche **Laboratoire de Physique des Solides** (Université Paris-Saclay) et **Gulliver** (Université Paris Sciences & Lettres – ESPCI-Paris), sous la direction de **Frédéric RESTAGNO**, directeur de recherche, et la co-direction de **Joshua D. McGRAW**, chargé de recherche.

Thèse soutenue à Paris-Saclay, le 13 Décembre 2022, par

Gabriel GUYARD

Composition du jury

Membres du jury avec voix délibérative

Giuseppe FOFFI Professeur, Université Paris-Saclay	Président
Karin JACOBS Professeure, Universität des Saarlandes	Rapporteur & Examinatrice
Christophe YBERT Directeur de recherche, CNRS - Université Claude Bernard	Rapporteur & Examinateur
Anne JUEL Professeure, The University of Manchester	Examinatrice

THESE DE DOCTORAT
NNT : 2022UPASP142

Acknowledgments

As I write these lines I have just been rewarded with the title of doctor, concluding nine years of a busy yet exiting student life. While I am certainly proud of this achievement, I also feel extremely grateful for having always been surrounded by caring people throughout my academic career. Therefore, I wish to make a few acknowledgments.

I would like to address my first words to my supervisors Joshua McGraw and Frédéric Restagno, who taught me so much over the past three years. Their trust, dedication, patience and kindness allowed me to work in sane and stimulating conditions. Additionally, their constant scientific support and numerous feedbacks were key to this project.

Because research is a team work, many thanks to Alexandre Vilquin, who not only had a tremendous scientific input on my research, but was also incredibly cheerful and helpful. In the same spirit, Stéphane Jouenne and Nicolas Sanson are warmly acknowledged for their fine expertise and smart suggestions. I am also thankful to all the engineers I had the chance to work with, in particular Élian Martin and Alexandra Baron-Ledez, who brilliantly drove the life of the laboratory.

I express my sincere gratitude to Prof. Dr. Karin Jacobs, Dr. Christophe Ybert, Prof. Giuseppe Foffi, Prof. Anne Juel, who reviewed this thesis and accepted to be part of my defense committee.

I am finally thankful to the *Agence Nationale de la Recherche* and to *TotalEnergies* for the generous funding, and to the *Institut Pierre-Gilles de Gennes* for the facilities.

On a more personal note, I wish to have a kind word for the research teams IndySoft, LBE, and MMN, who I have been sharing my everyday life with. I will for sure miss the animated lunch breaks and passionate discussions. Among these many people, Caroline Kopecz-Muller holds a special spot, for she enlightened my everyday life and provided vital emotional support.

I am also deeply indebted to my family. I will never be grateful enough for having been raised with such love and dedication, and for the opportunity to do long studies.

Last but definitely not least, I would like to mention my friends from ESPCI: Adrien, Antoine, Apolline, Baptiste, Caroline, Flora-Maud, Noémie, Miguel, Simon, Thibaut, Vincent, and Yohann. Over the years they have become truly important to me. May we keep creating good memories together.

Contents

Purpose of this manuscript

Flows at microscopic scales are ubiquitous in nature, from oil in porous rocks to biological materials in blood vessels. From a technological point of view, continuous race toward downsizing also pave the way towards artificial micro- and nanoscale flow devices. Manipulating liquids at such scales allows for cheap, quick and efficient characterization of chemicals and biological objects, and was made possible thanks to the development of microfabrication processes, often relying on the use of elastomers as core material.

Hydrodynamics theory offers a reliable framework to rationalize flows at small scales. In the general case, solving the flow equations requires two important ingredients: the mechanical behavior of the fluid, and the boundary condition at surrounding interfaces. The former relates to a bulk property, and may vary significantly between different fluids: water, dense colloidal suspensions or pastes for example are not governed by the same constitutive laws. Concerning the latter, physicists have often adopted an empirical approach: close to a solid surface, the tangential fluid velocity must be equal to that of the interface, that is zero in the case of fixed boundaries. This "sticky" or "no-slip" boundary condition has historically proven successful, but does not rely on any fundamental principle. With the growing interest for the microscale, and for complex fluids, many counterexamples have violated this no-slip boundary condition. While the effect of such discrepancy remains limited at macroscopic scales, its consequences may become considerable when the surface to volume ratio gets large.

To this regard, polymeric liquids are fascinating materials. On the one hand, their bulk mechanics have been known for years to be non-Newtonian: the stress is a non-linear or time dependent function of the strain rate. On the other hand, polymers have been shown to display non-trivial behaviors at boundaries, with phenomena such as adsorption, depletion or slip at the wall. These features, combined with a wide range of applications, make polymer flows at the microscale a dynamic field.

In this experimental work, we used microfluidic technologies and a lab-made evanescent wave microscope to study flows of polyacrylamide solutions, with focus on the semi-dilute regime, within a submicron-thick layer in the direct vicin-

ity of a glass surface. Our method allowed to simultaneously measure the rheology and characterize the hydrodynamic boundary condition of any transparent liquid under a pressure-driven flow. On the way toward more confinement, attention was paid to the specificities of flows within thin elastomer-made microchannels. In these systems, the coupling between a pressure-driven flow and the elasticity of the surrounding soft walls was the source of two notable complex effects. First the pressure-dependent conduit geometry makes the flow throughput a non-linear function of the driving pressure. Second the excess volume of liquid stored in the channel volume acts as a capacity, and results in a finite relaxation time scale upon sudden changes of pressure. By real-time monitoring of the flow-rate and pressure at channel inlet we were able to characterize these phenomena.

The present manuscript is organized as follow. In the first chapter, we recall the main physical concepts needed to address the question of polymer solution flows at microscopic scales. Attention is also given to the state of the art on hydrodynamic boundary conditions. The second chapter is dedicated to the careful description of the experimental tools and protocols used in this study, including microfluidics and microfabrication procedures, evanescent wave microscopy setup, and data treatment. The following two chapters examine the results of this work: first, the near-surface flow analysis of polyacrylamide solutions and then the elasto-hydrodynamic coupling in deformable microchannels. Finally, as a perspective, an experiment combining the two aforementioned tools is proposed and preliminary results are given.

We found that the hydrodynamic boundary condition for semi-dilute polyacrylamide solutions flowing over a glass surface is governed by electrostatic effects. While uncharged polymers permanently adsorb at the wall, leaving a chain-sized immobile layer, anionic polymers are repelled from the surface. The latter results in the presence of a low-viscosity lubrication layer that can be interpreted as an apparent slip at the wall, with associated slip lengths ranging up to the micrometric scale. Concerning soft microfluidics, we showed that the flow rate may be greatly enhanced by channel deformation, and the pressure gradient along the flow direction is no-longer constant. We also propose a theoretical model that rationalizes the relaxation time scale of these objects at all pressures.

Chapter 1

Introduction

1.1 Fluid dynamics for microfluidics

Hydrodynamics is the science of fluid motion. With such a general definition, it is not surprising to find that this topic in a plethora of situations, covering a wide range of time and length scales, and materials. One could name, among others, ocean streams, bacterial swimming, ice caps motion or biological flows as relevant fields. Hydrodynamic theory results from the work of renowned physicists such as Euler, Navier, Stokes and G.I. Taylor, to name a few. With three centuries of continuous development, the subject is rich, and in the present work, we shall use a fraction of the vast phenomenology described so far.

The framework for this study is microfluidics – the science and engineering of liquid manipulation in micrometer-sized channels – and the goal of this section is to recall the main governing laws that will help to describe the results of our experiments. Many of the results presented here are adapted from the textbook *Physical hydrodynamics* by Guyon, Hulin, Petit and Mitescu [1]. In this first section we will derive the fundamental flow equations at play in microfluidics and soft hydraulics, and recall the main results regarding transport in viscosity dominated situations.

1.1.1 Equation of motion for fluids

Momentum and mass conservation

Equations of motion often boil down to Newton's second law for point-like objects. When working with a finite-size system, the latter holds for each small element of volume composing the system. In the case of a liquid or a gas, these elements are named particle of fluid, and they are subject to both internal and

external stresses. In addition to Newton's law for momentum, the other important equation is mass conservation.

Unlike solids, where the variable of interest is typically a deformation field, flows are best described by a velocity field. For the latter, we will use Euler's description, that is $\boldsymbol{v}(\boldsymbol{r}, t)$ is the velocity of the particle of fluid located at position $\boldsymbol{r}$ at time t. In Cartesian coordinates, we denote $\boldsymbol{v} = \left[v_x\,,\ v_y\,,\ v_z\right]$ the components of the aforementioned field. With this framework, the momentum and mass conservation read, in their general form:

$$\rho \frac{\mathrm{D}\boldsymbol{v}}{\mathrm{D}t} = \boldsymbol{f} - \boldsymbol{\nabla} p + \boldsymbol{\nabla} \cdot \underline{\sigma} \tag{1.1}$$

$$\frac{\partial \rho}{\partial t} + \boldsymbol{\nabla} \cdot (\rho \boldsymbol{v}) = 0\,. \tag{1.2}$$

Here ρ denotes the density of the fluid, $\underline{\sigma}$ the deviatoric part of the internal stress tensor, p the pressure field (*i.e.* the diagonal part of the stress tensor), and $\boldsymbol{f}$ any other volume force applied to the particle of fluid – gravity or electromagnetic forces for example. The operator $\boldsymbol{\nabla}$ is the standard notation for $[\partial/\partial x\,,\ \partial/\partial y\,,\ \partial/\partial z]$, and the operator $\mathrm{D}/\mathrm{D}t$ means the derivative in the sens of Lagrange.

We will now simplify this set equations assuming first incompressible flows, meaning that ρ is a constant in space and time. This hypothesis works well for liquids, and even for gas as long as the velocity is small compared to the sound velocity. Second we need a constitutive equation for the stress tensor. In the general case, the latter is fluid-dependent, yet a large range of simple fluids, called Newtonian fluids, follow a linear relation between the local shear stress and the local velocity gradient. Therefore in the simple case of a shear flow of the form $\boldsymbol{v} = v_x(z)\boldsymbol{u_x}$, the shear stress reads:

$$\sigma_{xz} = \eta \frac{\partial v_x}{\partial z} = \eta \dot{\gamma}\,, \tag{1.3}$$

where we introduced the shear rate $\dot{\gamma} = \partial v_x/\partial z$, and the constant of proportionality η, called the viscosity. As will become clear later, this choice for the definition of the shear rate is natural for flows in rectangular microfluidic devices.

The general expression of the tensor $\underline{\sigma}$ for Newtonian fluids can be found in textbooks [1], yet equation 1.3 provides some physical insight on the quantity η. The viscosity quantifies the ability of a moving particle of fluid to put its neighbors in motion. More precisely, one shows that the quantity $\nu_0 = \eta/\rho$, called the kinematic viscosity, is a diffusion coefficient for the transport of momentum within the fluid. From an energetic point of view, viscous stress is a way to dissipate the kinetic energy of the fluid. Consequently viscosity is also associated

to friction: in viscosity-dominated flows, the drag force on a moving object is indeed proportional to η, as we will see in section 1.1.3.

In the case of incompressible Newtonian flows, the equation of motion takes the form of the Navier-Stokes equation:

$$\rho\left(\frac{\partial \boldsymbol{v}}{\partial t} + (\boldsymbol{v}\cdot\nabla)\boldsymbol{v}\right) = \eta\nabla^2\boldsymbol{v} - \nabla p + \boldsymbol{f} \tag{1.4}$$

$$\nabla\cdot\boldsymbol{v} = 0\,. \tag{1.5}$$

Because it applies to a large variety of situations, the Navier-Stokes equation has a central place in hydrodynamics. It is also a fascinating problem in applied mechanics, so far, no general solution was found. The difficulty of this equation is due to the non-linear term $(\boldsymbol{v}\cdot\nabla)\boldsymbol{v}$, arising from the Lagrangian derivative.

The Reynolds number

Let us place ourselves in the case where $\boldsymbol{f} = 0$. There are still four terms remaining in the Navier-Stokes equation. To simplify the resolution, it is common to make approximations by neglecting terms of less significance. This is done by evaluating dimensionless numbers that compare the relative orders of magnitude of relevant terms. For the Navier-Stoked equation, the Reynolds number Re compares the inertia term $\rho(\boldsymbol{v}\cdot\nabla)\boldsymbol{v}$ to the viscous term $\eta\nabla^2\boldsymbol{v}$. For a flow of typical size $\tilde{L}$ and typical velocity $\tilde{v}$, the Reynolds number reads:

$$\mathrm{Re} = \frac{\rho\tilde{v}\tilde{L}}{\eta} = \frac{\tilde{v}\tilde{L}}{\nu_0}\,. \tag{1.6}$$

When the Reynolds number is either small or large compared to unity, the Navier-Stokes equation simplifies. At large Reynolds number, the viscous term can be neglected, leading to Euler's equation, which provides a framework to study turbulent and ideal liquids flows. Conversely, at low Reyolds number, viscous effects dominate inertia, leading to the Stokes' equation. This latter equation is of great interest at microscopic scales, and describes laminar flows. With this framework in mind, we move on to the resolution of the equation of motion for flows in microfluidic channels.

1.1.2 Flows in microfluidic channels

From Stokes' equation to Poiseuille flow

Let us start by computing Reynolds number for a flow in a microchannel. With $\eta = 1.0\times10^{-3}$ Pa s, $\rho = 1.0\times10^{3}$ kg/m^3, $\tilde{v} = 1.0$ mm/s and $\tilde{L} = 10$ µm, we obtain

$\mathrm{Re} = 10^{-2} \ll 1$. In these conditions, and without other volume force, the flow is governed by Stokes' equation:

$$\eta \nabla^2 \boldsymbol{v} = \nabla p \,. \tag{1.7}$$

We mention the interesting result that, in the case of a flow between two infinite parallel plates, the non-linear term of the Navier-Stokes equation is rigorously zero, regardless of the Reynolds number. Note that here we dropped the time-dependent term $\rho \partial \boldsymbol{v}/\partial t$. While no steady state assumption is made *a priori*, the quasi-static assumption often proves a good approximation. This is justified by the fast transport of momentum by diffusion. In water, with $\nu_0 \approx 10^6$ μm^2/s, and $\tilde{L} \approx 10$ μm, the characteristic time for momentum to diffuse across the entire channel is $\tilde{L}^2/\nu_0 \approx 10^{-4}$ s, much shorter than any relevant time scale in the systems we will encounter.

We now solve Stokes' equation in the lubrication approximation [2], a situation describing thin films of fluids, and depicted in figure 1.1 (a). The flow takes place in a channel of length L and width w. While the bottom wall remains flat, the top surface has a profile $h(x, t)$, slowly varying in x, *i.e.* with $|\partial h/\partial x| \ll 1$. Furthermore we assume Hele-Shaw conditions, that is $h \ll w \ll L$, ensuring, invariance in the transverse y direction as long as the observations are made far away from the walls, which will alway be the case here. The flow is driven by a pressure difference Δp, applied between the inlet and the outlet of the channel. Note that in this study, pressures are given by convention relative to the atmospheric pressure p_{atm}.

Let us now evaluate the dominant terms to further simplify Stokes' equation. In this two-dimensional situation, the geometry imposes $v_z \ll v_x$, and derivatives with respect to x are negligible compared to derivatives with respect to z.

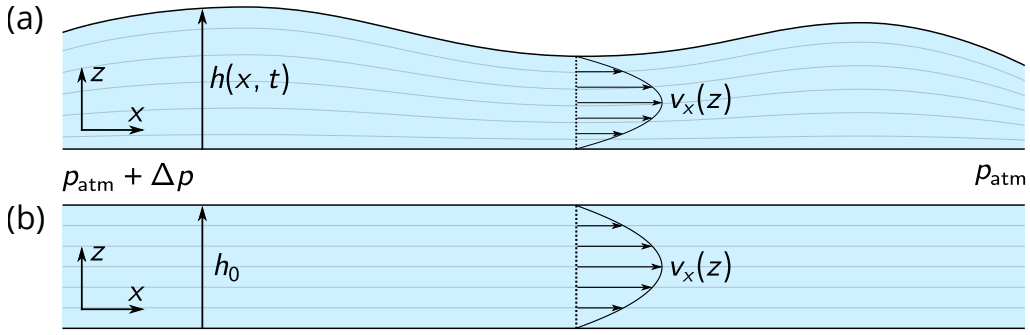

Figure 1.1: Schematics of a flow between two surfaces in the lubrication limit, for (a) a fluctuating top surface, and (b) for a flat top surface. Gray lines indicate the stream lines.

With that in mind, Stokes' equation simplifies as follow:

$$\frac{\partial p}{\partial x} = \eta \frac{\partial^2 v_x}{\partial z^2} \tag{1.8}$$

$$\frac{\partial p}{\partial y} = 0\,. \tag{1.9}$$

With a pressure field that is only x-dependent, equation 1.8 can be integrated twice with respect to z. The no-slip boundary condition imposes $v_x(z = 0) = 0$ and $v_x(z = h) = 0$. The relevance of this hypothesis will be discussed in section 1.1.2. We obtain:

$$v_x(x, z) = -\frac{1}{2\eta}\frac{\partial p}{\partial x} z\,(h(x, t) - z)\,. \tag{1.10}$$

The flow profile in the x-direction is parabolic with respect to z, and is maximum in the middle of the channel. To accommodate the x-dependence of h, the velocity field necessarily has a component in z, which could be calculated using the incompressibility condition of equation 1.5.

Let us now compute the flow rate q, defined as the integral of the velocity field along the cross section of the flow:

$$q(x, t) = w \int_0^h v_x(x, z)\mathrm{d}z = -\frac{w}{12\eta} h(x, t)^3 \frac{\partial p}{\partial x}\,. \tag{1.11}$$

On the other hand, volume conservation – a valid hypothesis in the incompressible limit– reads:

$$\frac{\partial q}{\partial x} = -w\frac{\partial h}{\partial t}\,. \tag{1.12}$$

This last equation reveals that, at steady state, q is a conserved quantity: if a channel narrows the flow accelerates and *vice versa*. Combining equations 1.11 and 1.12, we finally obtain Reynolds' lubrication equation [2]:

$$\frac{\partial h}{\partial t} = \frac{1}{12\eta}\frac{\partial}{\partial x}\left(h^3 \frac{\partial p}{\partial x}\right)\,. \tag{1.13}$$

Let us now apply this result to a rectangular channel, that is with a constant height profile $h(x, t) = h_0$, a situation known as Poiseuille flow and depicted in figure 1.1 (b). From equation 1.13, it comes $\partial^2 p/\partial x^2 = 0$, and with the boundary conditions $p(x = 0) = \Delta p$ and $p(x = L) = 0$, we obtain the linear pressure profile $p(x) = \Delta p\,(1 - x/L)$. Equation 1.10 then becomes:

$$v_x(z) = \frac{\Delta p}{2\eta L} z\,(h_0 - z)\,. \tag{1.14}$$

Note that the parabolic shape of the velocity profile generalizes to other geometries geometries [3]. Equation then 1.11 becomes:

$$q = \frac{w h_0^3}{12\eta L}\Delta p = \frac{\Delta p}{r_c}\,, \tag{1.15}$$

where we introduce the hydraulic resistance $r_c = 12\eta L/w h_0^3$. The name of this last quantity refers to Ohm's law in electronics. Indeed there exist many similarities between microfluidics and electronics [4, 5]. In this framework the fluid volume is analogous to the electric charge, the flow rate to the current, and the pressure to the voltage. The comparison holds well, since volume and charge are both conserved extensive quantities, the flux of which is driven by the gradient of an intensive quantity. This analogy provides a convenient framework for quick prototyping of microfluidic devices, and will be developed in section 4.3.1.

Toward soft hydraulics

The lubrication equation (1.13) allows to resolve flows in channels of fluctuating geometries. This situation may happen for example when the channel is made of a soft material, like a blood vessel or an elastomer-made microfluidic device. A properly-applied linear elasticity theory enables to connect the local height to the pressure field. This example of elasto-hydrodynamic coupling is known as soft hydraulics and it has been the subject to several recent studies. One particularly relevant review is the one by Christov [6].

In a compliant system, the externally applied pressure has two effects: driving the flow and deforming the channel. Regarding the flow rate, the two effects are concomitant: higher pressure means stronger driving force for the fluid and lower resistance – recall that r_c decreases with the cross section of the channel. The result is a superlinear increase of the flow rate with respect to the pressure, as documented in the literature [7, 8]. This effect is always present when working with elasomter-made microfluidic devices, and may bias the data if not taken into account. For this reason, a careful analysis of the elasto-hydrodynamic coupling between microfluidic flows and deformable boundaries, in both static and time-dependent regimes, is provided in chapter 4.

1.1.3 Transport at low Reynolds number

In this section we provide several of important results related to motion at low-Reynolds number, that will we useful throughout this document. The first one is the viscous drag generated by a spherical object of radius R_0 moving at velocity $\boldsymbol{u}$ in a solvent of viscosity η. By solving Stokes' equation in an infinite space with the

appropriate boundary conditions, Stokes showed that the drag force $\boldsymbol{F_d}$ reads [9]:

$$\boldsymbol{F_d} = -6\pi\eta R_0 \boldsymbol{u}\,. \tag{1.16}$$

When the drag force is proportional to the velocity of the moving object, one defines the friction coefficient ζ such that, $\boldsymbol{F_d} = -\zeta \boldsymbol{u}$. For Stokes' drag we thus have $\zeta = 6\pi\eta R_0$.

The second important result is related to diffusion, the transport mechanism encountered in section 1.1.1 for momentum, and that more generally describes random walks, Brownian motion, or heat transport within a material. Diffusion follows scaling laws that are different from ballistic transport, namely, for a diffusion coefficient D_0, the time τ to diffuse over a length d is approximately d^2/D_0. An important result from statistical physics is that, in the over-damped regime, the diffusion coefficient is given by the fluctuation-dissipation theorem [10]:

$$D_0 = \frac{k_\mathrm{B}\Theta}{\zeta}\,, \tag{1.17}$$

where k_B is the Boltzmann constant, Θ is the absolute temperature ($k_\mathrm{B}\Theta$ is the thermal energy, approximately 4×10^{-21} J at room temperature). For Stokes' drag, this result is known as the Stokes-Einstein relation:

$$D_0 = \frac{k_\mathrm{B}\Theta}{6\pi\eta R_0}\,. \tag{1.18}$$

In this section we have recalled the governing equations and framework to describe the motion of a fluid. Applying this theory in the context of microfluidics, we derived important results, such as the Reynolds lubrication equation (1.13), the parabolic Poiseuille flow profile in a rectangular channels (1.14), and the linear Ohm-like relation between pressure and flow rate (1.15). We also recalled two main equations related to transport at low Reynolds number: Stokes drag (1.16) and the fluctuation theorem (1.17). These two last results will be useful to study polymer chain dynamics, the topic of the next section.

1.2 Physics of polymers in solution

Polymers – long chain-like macromolecules – are encountered in many contexts: material science, chemistry, biology... For physicists, the central question about polymer focuses on finding universal laws connecting the molecular structure to macroscopic properties. Polymers became a dedicated field of study in the 20th century, when chemists mastered their synthesis and powerful characterization tools became available.

In this section we will recall the physical ingredients and theories to rationalize polymer chain conformation and dynamics in solution. Most of the results presented here were adapted from the textbook *Polymer physics* by Rubinstein and Colby [11]. To start, we will go through the ideal and real chain models for single polymer conformation. Then we will focus on solutions, where many chains may interact, with special attention for polyelectrolytes. Finally we will cover the relaxation dynamics of chains in solution, and use these results to rationalize the widely-observed shear-thinning mechanics of polymer solutions.

1.2.1 Single chain conformation

The ideal chain

The question we ask here is the following: for a linear polymer containing N monomers of size a, what is the size R of the chain ? Polymer chains are microscopic objects, subject to thermal noise and fluctuations. Therefore R is necessarily a random variable, and we have to use a statistical approach. Let us describe the monomers as a series of vectors $\{\vec{a_i}\}_{i=1,...,N}$ of same norm a, and define the end-to-end vector as $\overrightarrow{R_{ee}} = \sum \vec{a_i}$. Assuming uncorrelated orientation of $\vec{a_i}$, we have $\langle \overrightarrow{R_{ee}} \rangle = \vec{0}$, where $\langle ... \rangle$ mean the statistical average. To define R properly we thus use the second moment of the $\overrightarrow{R_{ee}}$ distribution. Doing so, we have:

$$R = \sqrt{\langle \overrightarrow{R_{ee}}^2 \rangle} = aN^{1/2} \,. \tag{1.19}$$

This first scaling is a famous result for random walks, which is not surprising: in the ideal case described above, a chain is indeed a random walk of monomers. A more interesting result is that this scaling holds even with monomer orientation correlation, as long as the latter is short-ranged.

This simple case illustrates a central concept in polymer physics: the details of the monomers local chemistry and interaction matter only up to a prefactor. In other words, up to a renormalization, the local structure can be neglected. This justifies the scaling law approach, popularized by de Gennes [12], in which

prefactors are dropped. Throughout this document we will use the symbol "~", meaning that the quantities are equal up to a dimensionless prefactor of order unity, and the symbol "$\propto$" when the prefactor has a dimension.

The polymer described above is called the ideal chain, in which no monomer-monomer or monomer-solvent was taken into account. We now go deeper into this model by giving the entropy S of such objects, the detailed calculation of which can be found in textbooks [11]. A standard approach consists in considering a random walk on a square lattice in three dimensions, and listing all the configurations associated to a given end-to-end vector, and a given number of steps N. Using Boltzmann definition for the entropy we obtain:

$$S(N, R) = S_0(N) - k_B \frac{3R^2}{2Na^2}, \tag{1.20}$$

where S_0 depends only on N. We can then compute the free energy F, which, in the absence of interaction energy, simply reads $F = -k_B\Theta$:

$$F(N, R) = F_0(N) + k_B\Theta \frac{3R^2}{2Na^2}. \tag{1.21}$$

The scaling $R \propto N^{1/2}$ is encoded in this expression of the free energy. The quadratic shape of the free energy with respect to R recalls the potential of a spring. This elastic behavior remarkably arises only from entropy, which is the reason why the ideal chain is sometimes referred to as an entropic spring.

The real chain

We now complexify the problem by adding monomer-monomer interactions. To do so we use Flory's approach, assuming excluded volume interactions [13]. With such repulsion, the chain undergoes a self-avoiding random walk, accounting for the fact that two monomers cannot overlap. With this constraint the chain size is expected to be swollen compared to a traditional random walk.

We define the excluded volume interaction parameter $\mathcal{V}$, which has the dimension of a volume. We consider a polymer chain of volume R^3, in which there are N monomers, supposed homogeneously distributed. The monomer concentration within this coil is thus $\tilde{c} = N/R^3$. For each monomer, the interaction energy is the proportional to the probability of finding another monomer within the volume $\mathcal{V}$, that is $\mathcal{V}\tilde{c} = \mathcal{V}N/R^3$. Since there are N monomers, and each interaction is assumed of energy $k_B\Theta$, the total interaction energy within the coil finally reads $k_B\Theta\mathcal{V}N^2/R^3$. Adding this interaction energy to the entropic term derived in the previous section (equation 1.21), we obtain a new expression for

the free energy:

$$F(N,R) \sim k_B\Theta\left(\mathcal{V}\frac{N^2}{R^3} + \frac{R^2}{Na^2}\right). \tag{1.22}$$

Note that we dropped the constant F_0, as well as all numerical prefactors. Minimizing free energy with respect to R, and assuming $\mathcal{V} \sim a^3$, we finally obtain a new scaling for R:

$$R \sim aN^{3/5}. \tag{1.23}$$

Compared to the ideal chain, where $R \sim aN^{1/2}$, the chain pervades a much larger volume: we say that the chain is swollen.

Here we assumed that excluded volume interaction was purely repulsive. More generally, $\mathcal{V}$ is the result of monomer-monomer steric repulsion and solvent mediated monomer-monomer attraction. One writes $\mathcal{V} = a^3(1-2\chi)$, were χ is the temperature-dependent Flory interaction parameter, that contains the information on monomer-monomer, monomer-solvent and solvent-solvent interactions. When assuming $\mathcal{V} > 0$, *i.e.* with a net repulsive excluded volume interaction, the situation is called good solvent condition. However it is possible to have $\mathcal{V} < 0$, a poor solvent condition, in which the chain follows the scaling $R \sim N^{1/3}$. Finally, the case $\mathcal{V} = 0$ corresponds to the θ-solvent condition, for which the chain follows the ideal scaling $R \sim N^{1/2}$. In the general case, we define the exponent ν, such that:

$$R \sim aN^{\nu} \quad \text{with} \quad \begin{cases} \nu = 1/3 & \text{bad solvent} \\ \nu = 1/2 & \theta\text{-solvent} \\ \nu = 3/5 & \text{good solvent} \end{cases}. \tag{1.24}$$

Neutron scattering experiments allowed to verify these fundamental scalings in solution [14, 15, 16].

1.2.2 Polymers in solution

So far we have discussed the conformation of a single chain in a solvent. Yet real-life systems are composed of many chains, either in solution, or without solvent in the case of a polymer melt. Focusing on the former, we now move on to the particular case of multiple chains in solution, which may or may not interact with each other: first we define the concept of dilute and semi-dilute solutions and derive important scaling laws, and then we provide some results about electrically charged polymers.

Two concentration regimes

The scalings derived in the previous section are expected to be valid in the limit of dilute solutions, in which chains are sufficiently far from each other not to interact. Yet a new physics arises when chains gets closer to one another and occupy the entire available volume. This occurs when the concentration reaches a critical concentration c^* called the overlap concentration, and here expressed in mass of polymer per unit volume of solution.

When $c < c^*$, the solution is in the dilute regime while $c > c^*$ correspond to the so-called semi-dilute regime. Theses situations are sketched in figure 1.2. The remarkable feature of a polymer chain is that it pervades a volume much larger than the sum of its individual monomers: $R^3 \gg Na^3$. Hence the overlap concentration is usually achieved at relatively low mass fraction, justifying the terminology "semi-dilute". As an example, the polyacryalmide of molecular weight 2×10^6 g/mol used in this study has an estimated overlap concentration of 2.8 mg/mL, and this number goes even lower for polyelectrolytes. Note that in this document, we will only investigate the case where c is not too large compared to c^*, a situation referred to as the semi-dilute non-entangled regime. Using the space-filling condition, we get the following scaling for the overlap concentration:

$$c^* \sim \frac{M_0}{\mathcal{N}_A}\frac{N}{R^3} \sim \frac{M_0}{\mathcal{N}_A}\frac{N^{1-3\nu}}{a^3}\,. \tag{1.25}$$

Here $\mathcal{N}_A$ is the Avogadro number and M_0 is the molar mass of a monomer. We can also define the overlap concentration $\tilde{c}^*$ in monomer per unit volume, that is $\tilde{c}^* = (\mathcal{N}_A/M_0)c$. For the real chain model in good solvent, $\nu = 3/5$, and $c^* \propto N^{-4/5}$.

In semi-dilute solutions, another length scale arises, the correlation length ξ. Physically, the correlation length corresponds to the mesh size of the network

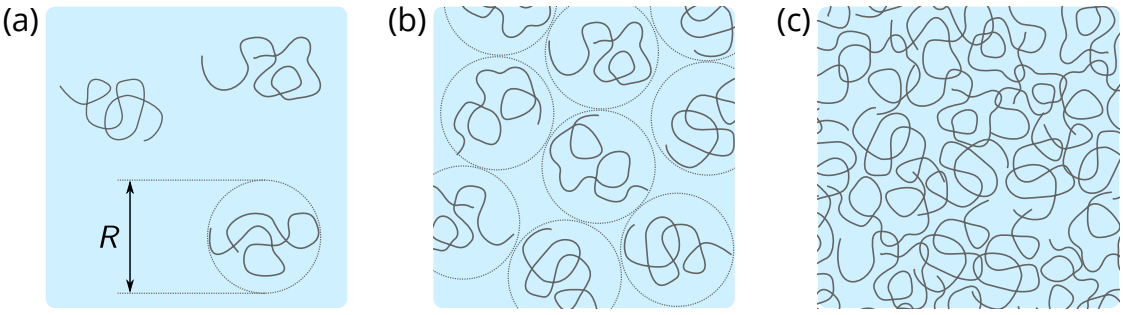

Figure 1.2: Polymer solution schematics in (a) the dilute regime, (b) at the overlap concentration, and (c) in the semi-dilute regime. Circles indicate the volume pervaded by the associated chains.

formed by overlapping chains. Said differently, it quantifies how often another chain is crossed when following a polymer backbone. The situation is sketched in figure 1.3. To compute ξ, we use a concept often used in polymer physics: the separation of lengths scales. The chain is divided in blobs of size ξ, each containing g monomers. Within a blob, neighboring chains are sufficiently far so that the chain follows an ideal scaling: $\xi \sim g^{\nu}$. Using the argument that chains and blobs are both space-filling, the monomer concentration in the solution $\tilde{c}$ is also the monomer concentration within a blob, namely $\tilde{c} \sim g/\xi^3$. Combining these two last equations, we obtain the dependence of the the correlation in the concentration:

$$\xi \propto \tilde{c}^{\nu/(1-3\nu)} . \tag{1.26}$$

In good solvent, we have $\xi \sim \tilde{c}^{-3/4}$, a scaling verified by neutron scattering experiments [14]. The correlation length decreases with the concentration, consistent with the picture of a network becoming denser. Additionally it is worth mentioning that ξ does not depend on N.

We may now go back to the initial problem of the chain size. At the scale of many blobs, overlapping chains screen the excluded volume interaction, thus the chains behave like random walks of correlation blobs. Using the scalings from the previous section, we obtain:

$$R \sim a\left(\tilde{c}a^3\right)^{(2\nu-1)/(2-6\nu)} N^{1/2} \propto N^{1/2} . \tag{1.27}$$

The chain size recovers the ideal scaling, only this time with a concentration-dependent prefactor. This result counter intuitive: in spite of the possible complex interaction arising in dense systems, chains behave ideally. This result generalizes to polymer melts and is known as the Flory theorem [17].

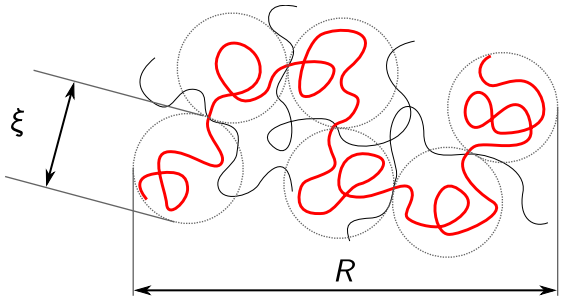

Figure 1.3: Schematics of a polymer chain in a semi-dilute network, with emphasis on the correlation length ξ and chain size R.

Introductions to polyelectrolytes

It is common in both industry and biological systems to deal with polymer chains that carry charges along their backbones. These are called polyelectrolytes, and the presence of charges creates a new type interactions that can be treated in a similar spirit as the neural case derived above. Below we give some useful results about polyelectrolytes, derived by Dobrynin and coworkers [18].

Let us consider a chain containing N monomers, and carrying a unit charge e every A monomers. We can use again a separation of length scales method and define an electrostatic blob of size ξ_e, containing g_e monomers. Within an electrostatic blob, the thermal energy dominates, so that the chain keeps an uncharged scaling: $\xi_e \sim g_e^{\nu}$. A blob builds up enough electrostatic energy to overcome $k_B\Theta$, such that blobs repel each other. The number of monomer per blob is obtained by balancing electrostatic and thermal energy:

$$g_e \sim k_B\Theta \frac{A^2 \varepsilon_0}{e^2}, \tag{1.28}$$

where ε_0 is the dielectric constant of the solvent. On scales larger that ξ_e, the chain behave as a stretched array of blobs due to electrostatic repulsion: $R \sim \xi_e N/g_e \sim aN$.

With a linear scaling of R with N, the volume pervaded by a chain gets large quickly, making the overlap concentration small compared to that of a neutral counterpart. Using equation 1.26, we have a new scaling law for the correlation length: $\xi \sim \tilde{c}^{-1/2}$, a scaling that we will used in chapter in section 3.2.2. Another feature of charged systems is their dependence in electrolyte concentration, since the the presence of salt screens electrostatic interactions. Dobrynin computed a range of other scaling laws for polyelectrolytes, with and without salt, that will also prove useful for data analysis in chapter 3.

1.2.3 Dynamical aspects and rheology

Now that we have explained the equilibrium conformation of polymer chains in solution, we will study the relaxation dynamics of these systems. As we will see, dynamics plays a crucial role in explaining the rheological properties of polymer solutions, which can be rationalized in the theory of viscoelasticity.

A purely elastic behavior is characterized by a constant finite elastic modulus, meaning that stress is proportional to strain. Conversely, a perfectly Newtonian liquid has a constant finite viscosity, with a stress proportional to the strain rate. Viscoelastic materials exhibit a combination of both. More specifically, a viscoelastic liquid behaves like a solid on short time scales, but flows like a liquid on longer time scales. For such time-dependent responses, the dynamics

is crucial, as it determines for a given situation, which of the two behaviors is dominant. A famous example of such behavior is Silly Putty, a material which bounces like a soft solid when dropped on the floor, but spreads like a liquid when left at rest on a table for several minutes [19].

An important result from standard linear viscoelastic theory [11, 20], connects the viscosity η to the stress relaxation modulus $G(t)$, describing the stress-relaxation of a material when submitted to a step-like strain:

$$\eta = \int_0^\infty G(t)\mathrm{d}t \sim G(\tau)\tau \,. \tag{1.29}$$

Here, τ is the characteristic relaxation time of the system. Note that in order to approximate the integral by a simple product of two factor, we assumed a unique relaxation time scale. This result is valid in the Maxwell model, the simplest framework for viscoelastic fluids, but this may not always be the case and systems with multiple time scales have been reported [21, 22]. In the following we investigate the relaxation dynamics of polymer chains in solution, in both dilute ans semi-dilute limits, in order to rationalize their rheological behavior using the viscoelasticity theory tools.

Dilute regime: Zimm time and intrinsic viscosity

Let us start with the dilute regime, and picture an single polymer coils of size R. In the Zimm model, this polymer coils drags the solvent molecules located within its pervaded volume and behaves like a colloidal particle of size R, in a bath of solvent of viscosity η_s. The diffusion coefficient D_0 of such objects is given by Stokes-Einstein relation: $D_0 \sim k_B\Theta/\eta_s R$. The Zimm time τ_Z is R^2/D_0, the time for the polymer coil to diffuse its own size, which finally reads:

$$\tau_Z \sim \frac{\eta_s R^3}{k_B\Theta} \sim \tau_0 N^{3\nu} \,, \tag{1.30}$$

where $\tau_0 = \eta_s a^3/k_B\Theta$ is the relaxation time of one monomer.

We now turn our attention to the viscosity of dilute polymer solutions, expected to increase with the concentration. We define the specific viscosity η_{sp} and the intrinsic viscosity $[\eta]$ of a solution with the following formulas:

$$\eta_{sp} = \frac{\eta - \eta_s}{\eta_s} \quad \text{and} \quad [\eta] = \lim_{c\to 0} \frac{\eta_{sp}}{c} \,. \tag{1.31}$$

By construction, $[\eta]$ is the initial slope of the specific viscosity *vs.* concentration curve, and has the dimension of a reciprocal mass concentration. For sufficiently low concentrations, we have $\eta_{sp} = [\eta]c$, and higher order developments of this

relation can be found in the literature [23]. In Zimm's framework, assuming that $G(\tau_Z)$ is of order $k_B\Theta$ per chain, we have:

$$[\eta] \sim \frac{\mathcal{N}_A}{M_0}\frac{R^3}{N} \sim \frac{1}{c^*} \sim \frac{\mathcal{N}_A}{M_0}a^3 N^{3\nu-1} . \tag{1.32}$$

In other words, the measurement of intrinsic viscosity allows an experimental determination of the overlap concentration. The latest equation is more commonly written [11]:

$$[\eta] = \phi_\infty \frac{R^3}{M} , \tag{1.33}$$

where $\phi_\infty = 0.425\mathcal{N}_A = 2.5 \times 10^{23}$ mol^{-1} is the universal Flory constant and $M = NM_0$ is the molar mass of the chain. Finally, in the dilute regime, we have $\eta_{sp} \sim c/c^*$. This formula is comparable to the viscosity of a dilute colloidal suspension, for which Einstein computed that $\eta_{sp} = \frac{5}{2}\phi$ where ϕ is the volume fraction occupied by the colloids [24].

Semi-dilute regime: Rouse dynamics and shear-thinning rheology

We now move on to the semi-dilute regime, where polymer chains cannot be considered independent from one another. In the Rouse model, the chain is described as a series of N beads of size a, connected by springs. Summing the contribution of each bead, the total friction coefficient of the chain is $\zeta_R \sim N\eta_s a$, and similarly to the Zimm time, the Rouse time τ_R reads:

$$\tau_R \sim \frac{\eta_s a R^2 N}{k_B\Theta} \sim \tau_0 N^{1+2\nu} . \tag{1.34}$$

In the following we place ourselves in the semi-dilute regime. Thus we assume $\nu = 1/2$ as suggested by the Flory theorem, discussed in section 1.2.2. The time τ_R corresponds to the relaxation of a chain of N monomers, but the same calculation holds for any subsection of $g < N$ monomers. Defining the p-th relaxation mode of the chain ($1 \leq p \leq N$) as the relaxation time τ_p of a segment of chain of length N/p, we have:

$$\tau_p \sim \tau_0 \left(\frac{N}{p}\right)^2 . \tag{1.35}$$

The mode p =1 corresponds to the Rouse time, the longest relaxation time of the system, while $p = N$ corresponds to the relaxation of a single monomer. The key idea of this model is that the N modes relax independently. With this framework Colby proposed a rationalization the apparent shear-dependent viscosity of semi-dilute polymer solutions [25].

Polymer solutions typically exhibit a shear-thinning behavior: the apparent viscosity plateaus at low shear rate, and then displays a power law decay – see section 2.4 for experimental data. The physical picture is the following: when submitted to shear, a polymer chain adopts an elongated conformation, which is associated to a different relaxation time compared to the unstretched chain. When the shear rate $\dot{\gamma}$ is smaller than $1/\tau_R$, all the modes have enough time to relax, and thus participate in the viscous dissipation. More generally, under a shear rate $\dot{\gamma}$, modes corresponding to $\tau_p < 1/\dot{\gamma}$ relax quickly enough to participate in the apparent viscosity, while modes for which $\tau_p > 1/\dot{\gamma}$ behave elastically. Summing the contributions of the viscous modes, one shows that:

$$\eta \sim k_B \Theta \check{c} N \tau_0 = \eta_0 \quad \text{when} \quad \dot{\gamma} < \tau_R^{-1} \tag{1.36}$$

$$\eta \sim \eta_0 \left(\tau_R \dot{\gamma}\right)^{-1/2} \quad \text{when} \quad \dot{\gamma} > \tau_R^{-1} . \tag{1.37}$$

This model describes well the experimentally-observed plateau viscosity, and predicts that the onset of shear thinning happens at a shear rate equal to the reciprocal Rouse time. Therefore, rheometry is a way to probe the longest relaxation time of a semi-dilute polymer solution. Concerning the decay of the viscosity as $\dot{\gamma}^{-1/2}$, experiments show a wider range power laws. We may explain this discrepancy by the fact that Colby assumed $\nu_0 = 1/2$, a condition likely unsatisfied on all length scales, especially on the scale of a correlation blob.

In this section we have defined the main tools of polymer physics and gave important scaling results. The key message is that polymers are random walk molecules, whose equilibrium size and relaxation time in solution depend essentially concentration, chain length, and molecular interactions. These object have a characteristic relaxation dynamics, that depends on the concentration regime. Knowing the microscopic features of the chain allows to predict the rheology of a polymeric sample. In the next section we will use these results to study polymer flows near solid surfaces.

1.3 Polymer hydrodynamics at interfaces

In section 1.2 we discussed a few bulk properties of polymer chains, that is to say in the case of an infinite, boundary-free medium. However the presence of a chains close to a surface has also been extensively studied and plays a major role in adhesion [26, 27], lubrication [28], colloidal suspension stabilization [29, 30, 31], transport in microchannels [32] as well as in our topic of interest: near-wall polymer flows.

In this section we will see how the presence of polymers near a solid surface modifies the hydrodynamic boundary condition. First we will explain the phenomenology of fluid slippage at a solid wall, then we will focus more specifically on slip of polymeric systems, and finally be will list some experimental tools available to investigate the problem.

1.3.1 Complex hydrodynamic boundary conditions

When solving the flow between two surfaces in section 1.1.2, we used a no-slip boundary condition. This commonly-used hypothesis states that the tangential velocity of the fluid at the wall is equal to the wall velocity, *i.e.* zero in the case of fixed boundaries. In spite of its numerous successes, this assumption does not rely on any fundamental principle, in fact as early as 1823, Navier predicted that it could be otherwise: fluid could slip at the wall, with a non-vanishing velocity.

To quantify the discrepancy between slip at the wall and simple boundary conditions, we introduce the slip length b, illustrated in figure 1.4 in the case of a simple shear flow at rate $\dot{\gamma}$. The slip length is the distance at which the velocity profile linearly extrapolates to zero, therefore the tangential velocity at the wall v_s reads $v_s = \dot{\gamma} b$. A situation where $b = 0$ corresponds to a no slip boundary condition, while the case of $b \to \infty$ describes an ideal plug flow.

Slippage has fundamental and practical consequences. Knowing the bound-

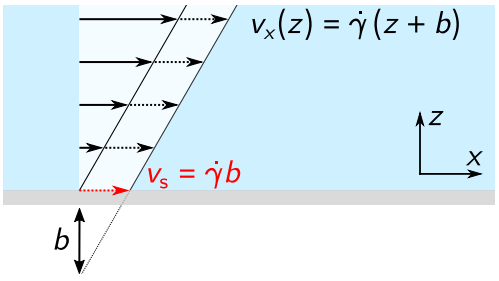

Figure 1.4: Illustration of a slip boundary condition in a shear-flow: v_x denotes the streamwise velocity, $\dot{\gamma}$ the shear-rate and b the slip length.

ary condition is essential to solve a fluid dynamics problem, particularly in micro- and nanofluidics contexts, where the surface to volume ratio is large. We will see in this section that when the slip length is comparable to the size of the system, it has a significant impact on its permeability. Additionally slip at the wall has been demonstrated to have practical consequences: it plays a role in extrusion instabilities of polymer melts [33] and adhesion [26, 27] for example. Finally, slip can make the interpretation of rheological data difficult, an issue reported in the literature [34, 35, 36]. A Couette cell rheometer for example assumes a no-slip condition to evaluate the shear rate, an estimate that becomes false if slip occurs.

The simplest framework for slip, proposed by Navier [37], is to assume an interfacial stress σ_w proportional to the slip velocity: $\sigma_w = k_s v_s$, where we introduced k_s the friction coefficient between the wall and the flow. Balancing this stress with the viscous stress $\sigma_{xy} = \eta\dot{\gamma}$, the slip length reads:

$$b = \frac{\eta}{k_s} . \tag{1.38}$$

The former equation reveals two remarkable features. First, slip is the result of the balance between a surface effect, the fluid-wall interaction, and a bulk effect, the viscous response of the fluid. Second, slip is connected to the rheology of the fluid, setting the need for proper characterization of the fluid mechanical properties.

In simple liquids, slip has been shown both experimentally and numerically to depend on the wettability of the surface. For water flows, reported slip lengths

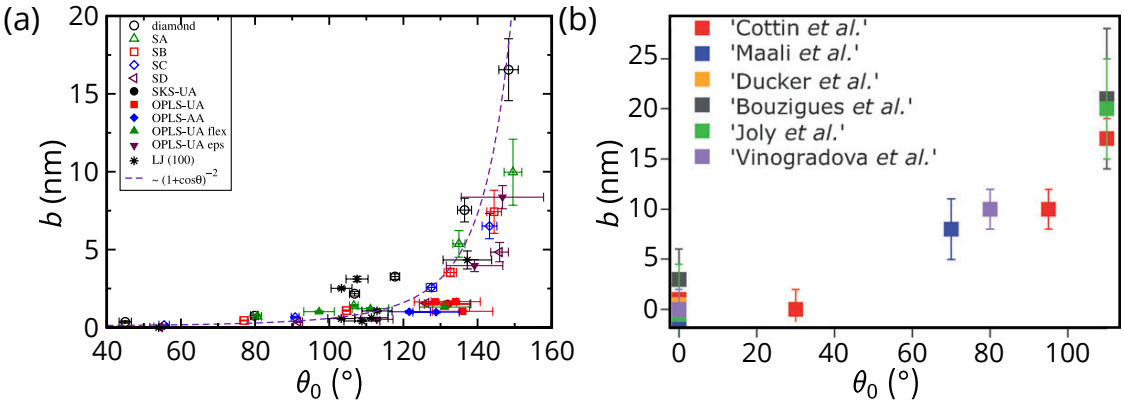

Figure 1.5: Slip length as a function of the contact angle. (a) Molecular dynamic simulation for water on various smooth surfaces, by Huang *et al.* [38]. (b) Experimental measurements available in the literature, taken from Bocquet and Charlaix [39].

are of molecular size, ranging from a few tenths of nanometers on hydrophilic surfaces to a few nanometers on hydrophobic ones [40, 41, 39]. Figure 1.5 shows reported slip length as a function of the contact angle θ_0 for water on various surfaces, for both molecular dynamics simulations and experiments. While the aforementioned results are well accepted for smooth surfaces, let us notice that much larger slip was measured in the case of flows on textured hydrophobic surface, with micrometric slip length reported [42, 43].

1.3.2 Near-wall polymer flows

Unlike simple fluids, soft matter offers a wide variety of complex fluids that exhibit large slip [44, 45]. These include for example colloidal suspension, gels, pastes and polymeric systems. In this section we focus on slip mechanisms and other interfacial phenomena for both polymer melts and solutions.

Slip in polymer melts

Let us first focus on polymer melts, which have received significant attention for a few decades. In 1979, de Gennes used Navier's framework – see equation 1.38 – to study the slip of polymer melts on ideal surfaces [48]. Here by ideal one

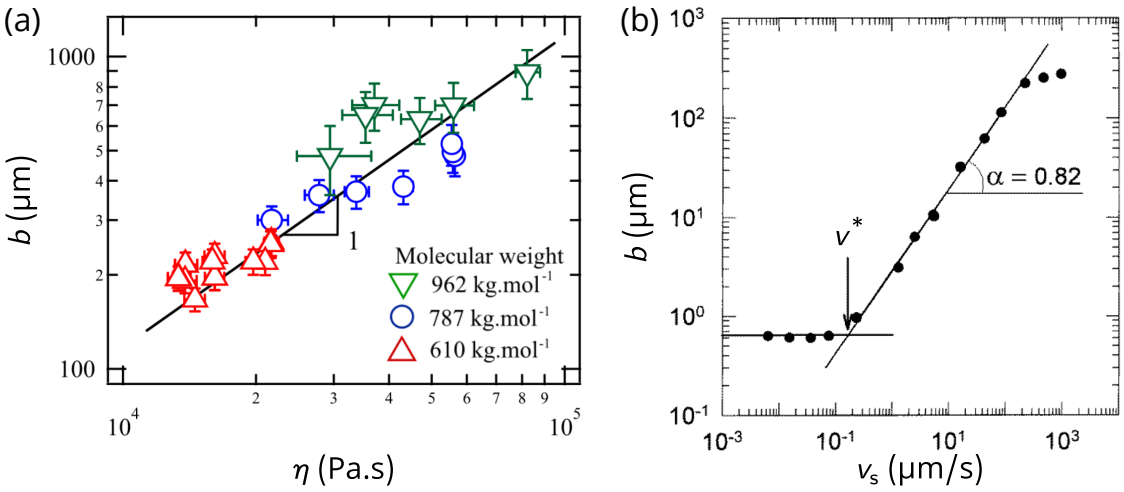

Figure 1.6: (a) Slip length of polymer melts on ideal surface as a function of the viscosity, taken from Hénot *et al.*[46]. The results were obtained with polydimethylsiloxane (PDMS) at different molecular weight as indicated, flowing on silica grafted with short chains. (b) Slip length as a function of the slip velocity taken from Léger *et al.* [47]. The results were obtained with PDMS on a surface grafted with long chains.

means that the solid interface is assumed flat, ungrafted and non-adsorbing. In these conditions, the friction coefficient, k_s is expected to be a monomeric property, that is to say independent on the chain length, and of the same order of magnitude as that of monomeric liquids. The melt viscosity on the other hand, scales like $\eta \propto N^3$ in the reptation theory [49], and may become large as compared to that of the equivalent monomeric liquid. Therefore the slip length is also expected to scale like $b \propto N^3$ and reach much larger values as compared to monomeric liquids. This molecular weight dependence was recently verified experimentally with different methods [50, 51, 46] – see section 1.3.3 –, and exemplified in figure 1.6 (a).

A remarkable feature of the case discussed above for ideal surfaces is the fact that the slip length does not depend on the local shear rate. However this behavior seems to be more the exception than the rule, and more complex behaviors were predicted and reported, with velocity-dependent slip lengths [53, 47, 54, 55]. Typical experimental data by Léger *et al.* are shown in figure 1.6 (b). At low velocity, the slip length is small and independent from the velocity. Above a critical slip velocity v^*, the slip length increases with the slip velocity, as a power law, and finally plateaus again at large velocities. This observation can be rationalized by carefully looking at chain-surface interaction. When a chain is attached to

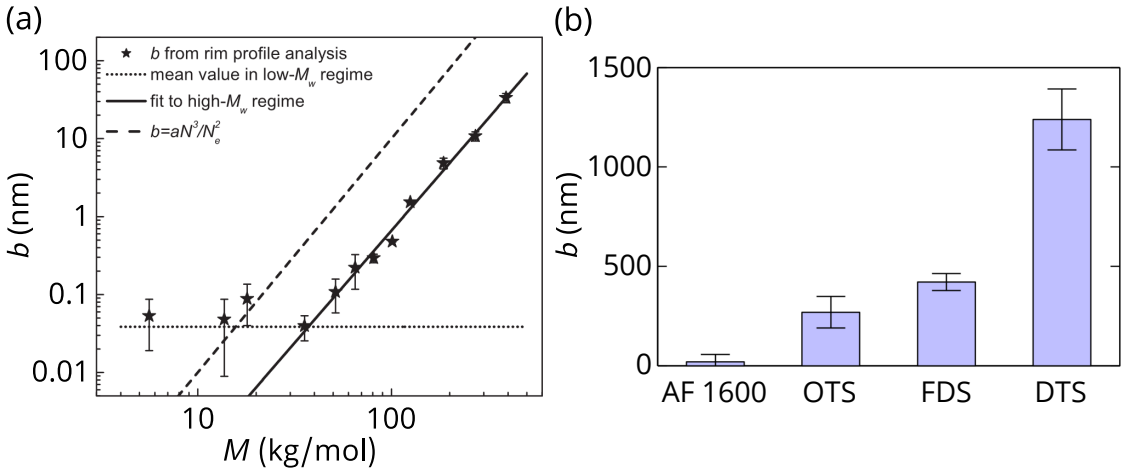

Figure 1.7: Slip length measured in dewetting experiments for polystyrene melts, for different molecular weights and hydrophobized substrates. (a) Slip length as a function of the molecular weight, measured on AF 1600, taken from Bäumchen *et al.* [50]. (b) Slip length, on various surfaces, for a molecular weight of 13 kg/mol, from McGraw *et al.* [52] (AF 1600: fluorinated polymer, OTS: octadecyltrichlorosilane, FDS: perfluorodecyltrichlorosilane, DTS: dodecyltrichlorosilane).

the surface, either by adsorption or chemical grafting, entanglements between anchored chains and bulk chains occur. At low velocity, these entanglements drastically increase the friction coefficient, leading to smaller slip length. Above v^* the chains gradually disentangle under flow, a feature associated to smaller friction coefficient an larger slip length. Finally, when chains at the wall are fully disentangled from that of the bulk, one recovers the ideal substrate case, with monomeric friction and large slip.

The importance of local entanglements in slip of polymer melts was also highlighted by the group of Jacobs, by studying the dewetting of polystyrene on hydrophobized substrates. In figure 1.7 (a) is plotted the slip length as a function of the molecular weight. Above a critical chain length for entanglements, the scaling $b \propto M^3$ predicted by De Gennes is recovered while below this threshold, weak slip is observed. On the other hand, figure 1.7 (b) shows that for a given molecular weight, the slip length strongly depend on the surface. This observation is not attributed to the surface wettability, but to structure of the grafted layer.

The disentanglement-induced onset of large slip described above has proven successful to capture the physical picture of slippage in polymer melts, where chains must be in direct contact with the wall. In solutions, the story is different, notably because the polymer concentration may be locally inhomogeneous close to a surface, as we now discuss.

Slip in polymer solutions

In solution, chains no longer have to be in contact with the wall, in fact close to a boundary, the polymer concentration does not even have to be homogeneous. This feature is not without consequences for near-wall flows. A chain interacts with a surface though a potential, which can be attractive or repulsive [56]. In ad-

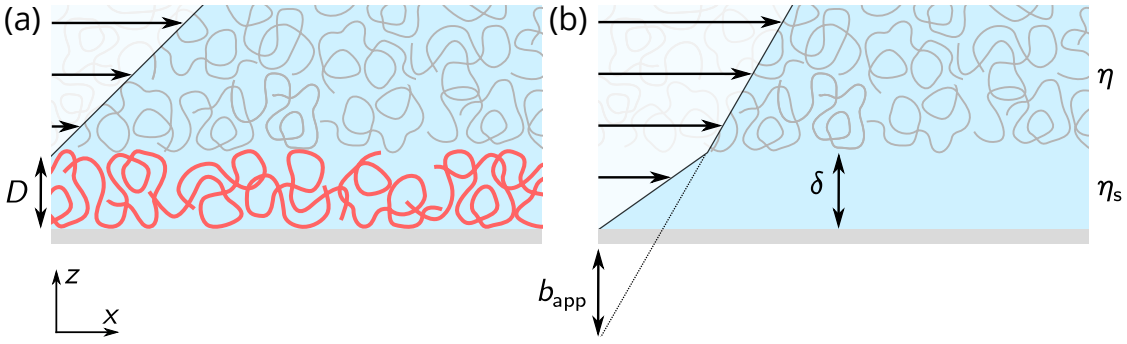

Figure 1.8: Different scenarios for near-surface flows, with (a) an immobile adsorbed layer, and (b) a depletion-induced apparent slip.

dition to this energetic consideration, approaching a chain close to a surface also results in an entropic penalty. Attractive walls lead to a permanently adsorbed layer of chains at wall-surface. This phenomenon explains the decrease in permeability of porous media when exposed to an adsorbing polymer solution, a major issue in enhanced oil recovery [57]. To push oil out of a porous natural reservoirs, water in injected. Yet because of Saffman-Taylor – also known as viscous fingering – instability [58, 59], polymers are added so that the viscosity of the pushing fluid matched that of oil. Chains of high molecular weight are typically used, yet once adsorbed the induced permeability drop causes increased energy loss in through viscous dissipation. More generally, adsorbed of grafted chains are at play in colloidal suspension stabilization, [29] lubrication [28], or surface modification [60]. Inversely, repulsive walls create locally a low concentration layer that enhances flows *via* the formation of a low-viscosity lubrication layer at the wall [61, 34].

The aforementioned phenomenology can be rationalized by defining an inhomogeneous polymer concentration profile, that is constant far from the wall, and increases or vanishes as one gets closer to the surface, resulting in a spatially-dependent viscosity. Denoting δ the characteristic distance over which the concentration gradient develops, the problem can be simplified by considering a stratified concentration profile, as depicted in figure 1.8. Regarding the flow profile, the situations are the following. For attractive surfaces, the immobile adsorbed layer of thickness D shifts the no-slip plane inside the channel [62], a case that can be seen as negative slip taking $b = -D$. Conversely, the stratified flow displays an apparent slip condition. Assuming a no-slip boundary condition in the in the lubrication layer, of thickness δ and viscosity η_s, and continuity of stress, one shows that the apparent slip length b_{app} obtained by extrapolating the bulk velocity profile reads:

$$b_{app} = \delta \left(\frac{\eta}{\eta_s} - 1 \right) \approx \delta \frac{\eta}{\eta_s} . \tag{1.39}$$

The last approximation assumes large viscosity mismatch between the two layers, which is relevant for semi-dilute polymer solution. This last equation shows that apparent slip scales like a molecular length δ, amplified by a factor η/η_s which can be large. It is also interesting to note that equation 1.39 has a similar form as equation 1.38, taking $k_s = \eta_s/\delta$.

Having introduced stratified fluid structure to describe hydrodynamic boundary conditions in polymer solutions, one must still to connect δ and D to the fluid and surface properties. This subject will be treated in chapter 3, to rationalize the extrapolation lengths of velocity profiles measured in polymer solutions. Finally, we mention that scenarios of slip in semi-dilute polymer solution involving monomer-wall friction have also recently been demonstrated, without the need

for concentration inhomogeneity near the surface [63].

In this section we have introduced concepts and theories to explain slip at the wall in polymeric systems. But addressing the question experimentally is a challenge, essentially because the physical ingredients at stake are molecular scaled. In the following, we go over some routes to investigate slip in laboratory.

1.3.3 Experimental methods for slip measurement

There are two main approaches to experimentally investigate slip at the wall. The first one consists in imaging the flow close to the surface with sufficient precision to determine the slip length. The second route, indirect, consists in measuring the effect of slip on an different accessible quantity. For more details on that topic the reader may refer to the reviews by Lauga *et al.* [40] and Neto *et al.* [41].

Le us first focus on indirect methods. Two classes of experimental pathways are mainly used: measuring the pressure *vs.* flow rate curve in a microchannel or measuring the force applied on an object moving near a surface. Let us start with a calculation. In section 1.1.2 we computed the flow profile and hydraulic resistance for a flow in a rectangular microchannel with a no-slip boundary condition. The same calculation with a slip length b at top and bottom wall gives:

$$v_x(z) = \frac{\Delta p}{2\eta L}\left[z\left(h_0 - z\right) + h_0 b\right] . \tag{1.40}$$

Integrating this profile along the cross section of the channel we obtain a new expression for the flow rate q:

$$q = \frac{\Delta p}{r_c}\left(1 + 6\frac{b}{h_0}\right) , \tag{1.41}$$

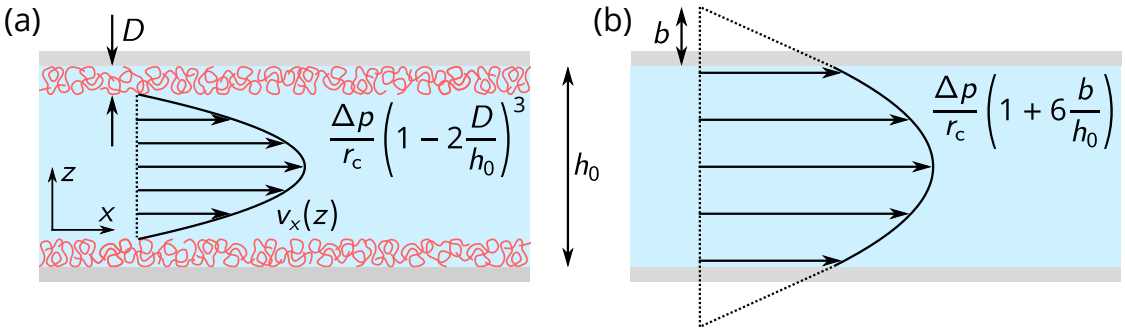

Figure 1.9: Modified parabolic flow profile, when (a) an adsorbed polymer layer is formed at surrounding surfaces and (b) slip at the wall occurs at top and bottom walls.

where $\Delta p/r_c = w h_0^3 \Delta p/12\eta L$ is the flow rate in the absence of slip. Similarly, with an adsorbed layer of thickness D, we have:

$$q = \frac{\Delta p}{r_c}\left(1 - 2\frac{D}{h_0}\right)^3 . \tag{1.42}$$

The two situations are depicted in figure 1.9, in the simplified case where the boundary condition is the same at top and bottom walls. Equations 1.41 and 1.42 show that boundary conditions may have a tremendous impact on the flow rate – or similarly the fluid velocity – provided the slip length or the adsorbed layer thickness is of the order or larger than the channel size. Let us notice that, unlike the situation of figure 1.9 (a), the presence of slip is not simply analogous to a channel of size $h_0 + 2b$.

With this method, slip length of the order of a few dozens of nanometers were measured in monomeric fluids over various surfaces [64, 65, 66]. Comparable procedures were also used for polymeric systems [67]. Finally, similar methods are also widely used by the oil industry to measure the adsorption-induced permeability drop in granular materials [68, 69, 57].

Another indirect method consists in approaching – or oscillating – an object, let us say a sphere, close to a surface and measure the associated time-dependent drag force [70, 71]. This situation can be achieved with an atomic force microscope [72] or a surface-force apparatus [73, 74]. Close to a surface, the expression of equation 1.16, valid in an infinite space, breaks down, and the computation of the drag force requires the full resolution of the Stokes' equation between the sphere and the wall, therefore involving the hydrodynamic boundary condition. In such cases fitting the force-displacement curves allows to extract a slip length.

A last approach we mention here, that has proven successful for polymer melts, measures slip lengths by studying the dewetting of thins films on hydrophobized surfaces. When taken above the glass transition temperature films dewet by forming holes. The height profile and the growth dynamic of these patterns can be connected to the slip length using a modified lubrication theory [50, 55, 75].

The methods described so far rely on indirect manifestations of fluid slippage. As a result, they require a complete physical modeling that includes slip, and a well-characterized experimental setups. We now turn our attention to direct measurement of hydrodynamic boundary condition. Flow visualization has always been at the center of experimental fluid dynamics. Today particle image velocimetry (PIV), a technique based on image correlation in a tracer-containing fluid, is widely used to characterize flows. Pushing PIV to the microscale allows to measure boundary conditions [76, 77].

Fluorescence recovery after photobleaching (FRAP) is another local flow mapping setup designed to measure slippage. In this experiment, the dye-containing fluid of interest is marked by photobleaching while sheared, allowing to characterize the flow by image analysis. This technique is well suited for polymer melts and concentrated solutions, where large slip is expected [47, 78, 63].

In this study, we used a variation on PIV: particle tracking velocimetry (PTV). Instead of doing image correlation in a region of interest, colloids embedded in the fluid are tracked individually, and serve as marker of the local flow field. Additionally, the particles are observed under total internal reflection fluorescence microscopy (TIRFM), which offers several advantages that we now describe.

TIRFM was invented in 1981 be Axelrod [79, 80] for cell imaging. In TIRFM the sample is illuminated by an evanescent wave created by total reflection of a laser at the interface between a high-index substrate and a low-index sample. Provided the incident angle exceeds the critical angle for refraction, an exponentially decaying field called an evanescent wave builds up orthogonality to the interface. The decay length is small: of the order of the laser wavelength. Hence only a thin layer of the sample close the interface can be observed. The light sheet is usually thinner than the depth of field of the imaging system, making out-of-focus issues less problematic. In other words one can image the sample at interface without perturbation from the bulk. TIRFM is still a widespread tool in biology, and is now coupled with sophisticated super-resolution techniques [81, 82].

Tracking the motion of microscopic objects is central in experimental soft matter physics [83]. Another advantage of evanescent wave illumination is the encoding of the position of an object in its fluorescence intensity. Because of the decaying field, a bright object is interpreted closer to the wall than a darker one, in a quantitative way. Said differently, the logarithm of the intensity provides a precise measurement of the position relative to the interface, allowing three-dimensional particle tracking. This feature made TIRFM a powerful tool to study soft matter systems, starting with colloidal force measurement [84, 85, 86], near-surface Brownian motion [87, 88], and finally flow imaging and slip measurement [89, 90, 91]. The question of the tracer size naturally arise when performing PTV. Desire for passive tracers leans toward the use particles as small as possible, yet smallest tracers typically display lower signal intensity, and enhanced Brownian diffusion, making them more difficult to track. The question of the tracer size naturally arises when performing PTV. Desire for passive tracers leans toward the use particles as small as possible, yet smaller objects typically display lower signal intensity, and enhanced Brownian diffusion, making them more difficult to track. The impossibility of achieving perfect tracer passivity in real-life setups is a limitation of this method. In the next chap-

ter, and in particular in sections 2.1 and 2.3 we describe in details our own implementation a TIRF microscope, as well as the calibration and particle tracking procedure.

Conclusion of the chapter

In this part we recalled a list of concepts and results borrowed from hydrodynamics and polymer physics. The main messages are the following. In microfluidics environments, flows are dominated by viscosity, and for the case of simple fluids, the velocity profile can be calculated analytically. The latter depends only on the applied pressure, the viscosity, and the channel geometry. Polymers on the other hand are complex molecular objects. In solution, there size and dynamic dictates the macroscopic behavior, which may be non linear. With these tools, we were able to highlight the state of the art regarding near-surface flows of polymeric liquids, with stress on hydrodynamic boundary conditions. Rationalizing slippage phenomena involves the comprehensive understanding of chain-surface interaction, but also of the bulk rheological properties of the flowing material. Lastly we have been through several experimental approaches to investigate this problem. In the next chapter, we will go through our own experimental setup to address interfacial flows.

Chapter 2

Materials and methods

The goal of this study is to experimentally investigate near-wall flows of polymer solutions. To do so, suitable experimental processes are required. To generate and finely control flows at the scale of a few micrometers, microfabrication tools and microfluidic equipment were used. Then, flow mapping was achieved by coupling particle tracking velocimetry with evanescent wave microscopy. In this chapter, we go in details through the equipment and experimental procedures used for this investigation.

The following parts of the chapter are organized as follow: section 2.1 is dedicated to the description of our lab-made total internal reflection fluorescence microscope. Microchannel manufacturing and fluidic procedures are then the subject of section 2.2. Section 2.3 covers the data treatment, with emphasis on our tracking routines. Finally, section 2.4 details polymer sample preparation and rheological characterization.

2.1 Evanescent wave microscopy : TIRFM

Microscopes may be one of the most iconic laboratory piece of equipment – at least to the general public – for a good reason: it is of everyday use in plethora of experimental fields. Among others, one can name geology, material science, soft matter, nanotechnologies and, biology. Optical microscopy is an imaging technique, aimed at providing magnified images of small objects based on their interaction with light. As a result, microscopes always feature these key elements: a light source, an optical magnifying apparatus, and a light sensor – which can just be the operator's eye. With these usually comes a set of optical and mechanical parts, along with add-ons specific to each type of microscopy. Among the many improvements made in the field over the years, the development of fluorescence microscopes is probably a landmark [92]. With this technique, it is

no longer the light transmitted or absorbed by the sample that is collected, but the fluorescent light produced *in situ* by specific molecules within the sample as a reaction to the incident light. These molecules are called fluorophores and are used to label the region of interest of the sample prior to imaging. This results in more contrast and more selectivity in experimental images.

The resolution of microscopy images is limited by diffraction, that is typically down to 200 nm when working with visible light. Recent development allowed to push this theoretical barriers [93], giving birth to super-resolution microscopy and finding applications in cell biology [94]. Microscopy experiments provide two-dimensional images of the sample, in the plane orthogonal to the optical axis. Moving on to three dimensions (3D) requires higher level of sophistication, for instance with confocal microscopy [95, 96]. Here we use a complementary approach: total internal reflection fluorescence microscopy (TIRFM).

Initially developed for cell-imaging [79, 97] the principle of TIRFM is the following: the sample, is illuminated with an evanescent wave field, created at the substrate-sample interface. This wave field is exponentially attenuated along the direction normal to this interface, over a distance that is of the same order as the wavelength of the illumination light. This way, only a sub-micron layer at the sample surface is observed, making this technique particularly relevant to study interface phenomena. The second advantage of evanescent wave illumination is the ability to determine the wall-normal position of imaged objects. Because of the non-homogeneous wave field, an object close to the interface will be relatively brighter than a further object. In other words, the logarithm of the fluorescence intensity encodes the distance to the wall. This allows for a 3D tracking of identical objects, and this technique was more recently used to study near-surface flows [98, 90] and colloidal diffusion [99, 87, 88].

In this first section we detail the setup of our lab-made evanescent wave microscope, its fine setting protocol, and the incident angle measurement procedure.

2.1.1 Experimental setup description

In figure 2.1 are sketched (a) top and (b) side views of the TIRFM experimental setup. References and details about important parts are provided in table 2.1 at the end of this section. The setup was assembled on a 75 cm by 150 cm vibration-damping optical table. A laser source generates a continuous monochromatic collimated light beam of tunable power, up to 150 mW, at the wavelength λ = 488 nm. A series of 3 mirrors M1, M2, M3, guided the light to a beam expander (BE). M1 was mounted on a periscope composed of two mirrors inclined at 45° with respect to the xy-plane of the table. Therefore the height of the beam could be controlled along the z-direction.

The BE was composed of a microscope objective lens of magnification 10x, and a converging lens of focal length 150 mm, the distance between which was the sum of their focal lengths. By doing so, the outcoming beam was collimated, and the beam had a diameter of typically 1 cm. Two diaphragms irises A1 and A2 placed before and after the BE, allowed to select only the central part of the beam, and helped during the alignment procedure described in section 2.1.2. Mirrors M4, M5 and M6 guided the beam toward the rear light port of the microscope, equipped with the iris A3. The lens L2 focused the beam at the back focal plane of the TIRF-objective. As pictured in figure 2.1 (b), a dichroic cube of splitting wavelength 500 nm allowed the laser beam to be reflected toward the TIRF-objective lens, while allowing transmission of higher wavelengths. The latter objective was mounted on a piezoelectric element, so it could translate along z with nanometric precision in a range of approximately 100 µm, allowing a fine

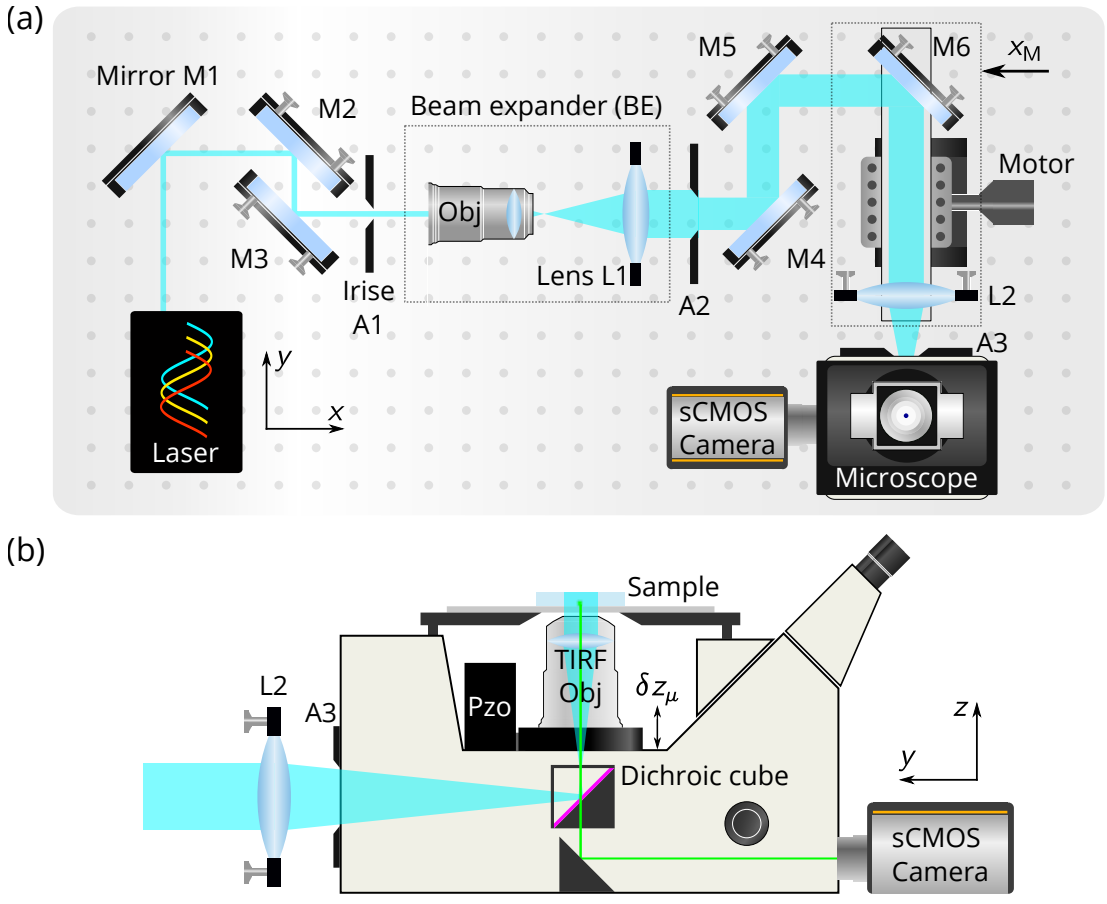

Figure 2.1: Schematic (a) top and (b) side views of the optical setup used for TIRFM experiments. Additional details about parts can be found in table 2.1.

control of the focusing plane. When the beam was aligned with the objective optical axis, as drawn in figure 2.1, the beam escaped the objective vertically.

In our TIRFM set up, the objective lens had a double role: guiding the excitation beam to the sample as described above, and collecting the fluorescence light emitted by the sample. The latter was always at a wavelength larger than the former's due to a phenomenon called Stokes shift, that translates energy conservation for the fluorophore molecule. The dichroic cube splitting frequency was chosen such that the fluorescence light was transmitted, and then reflected toward the camera by another cube, as depicted in figure 2.1 (b).

Mirror M6 and lens L2 were mounted on a translation stage actuated by a stepper motor that allowed translation in the x-direction with micrometric precision and a range of more than 10 mm. This way, the beam could be driven a distance x_M off-axis with respect to the TIRFM-objective optical axis. As depicted in figure 2.2 (a), this induced a finite angle θ with respect to the vertical direction for the outcoming beam. The schematized situation of the latter figure, that relies on geometric optics, is however misleading to rationalize θ quantitatively. The angle must be computed using the optic transfer function of the TIRFM-objective lens [99]:

$$\sin(\theta) = \frac{x_M}{n_g f'}, \tag{2.1}$$

where n_g denotes the index of the glass making the optics, and f' is the focal length of the objective. Note that in practice, objectives are made of multiple lenses, which makes the position of the optic center and focal planes – as well as the equivalent focal length – non-trivial and, in this case, unknown. Equation 2.1 reveals that changing x_M is a simple way of controlling θ.

Practically, the accessible range of θ was limited by the numerical aperture (NA) of the objective, namely the largest accessible angle was $\theta_{max} = \arcsin(NA/n_g)$.

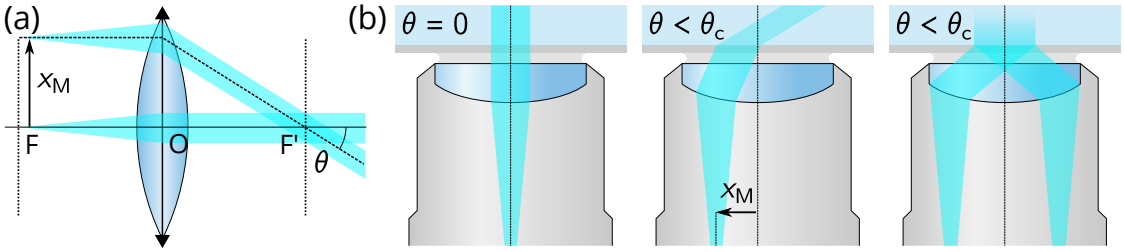

Figure 2.2: (a) Geometric optical model illustrating the optical path of a laser beam when driven off the axis of a converging lens. O is the optical center of the lens, F′ and F refer to the positions of its focal and back-focal planes, respectively. (b) Schematic picture of the laser beam at objective-sample interface, for three different incident angles.

For our 1.46-NA TIRFM-objective lens, and with $n_g = 1.518$ we had $\theta_{max} \approx 74.1°$. To achieve total internal reflection, the incident angle must be larger than the critical angle at the glass-sample interface. Denoting $n_{sample} = 1.33$ the refractive index of the water-based sample, we have $\theta_c = \arcsin(n_{sample}/n_g) \approx 61.2°$. This critical angle is defined only if $n_{sample} < n_g$, and can be reached provided NA > n_{sample}. The latter inequality provides a simple criterion to assess whether or not a sample can be theoretically used for TIRFM application with a given objective lens. Figure 2.2 (b) shows schematically the path taken by the beam as the beam incidence was moved from zero to criticality. For simplicity, we do not show the reflected part of the beam for angles lower than the critical one.

Above the critical angle, an evanescent wave developed in the sample, in the wall-normal direction. The complex amplitude of the associated wave field is of the form:

$$E(z, t) = E_0 \exp\left(-\frac{z}{2\Pi}\right) \exp\left(-j\omega t\right), \tag{2.2}$$

where E_0 denotes the wave amplitude, z the direction normal to the interface, ω the wave angular frequency, and t is the time. Note that there was no need to consider light polarization in this study. The penetration length Π is the typical length over which the wave field was attenuated. Using boundary conditions for electromagnetic waves at the objective-sample interface, we have [80]:

$$\Pi = \frac{\lambda}{4\pi} \frac{1}{\sqrt{n_g^2 \sin^2\theta - n_{sample}^2}}. \tag{2.3}$$

For fluorescence applications, the quantity of interest is the intensity of the wave field, $I \propto EE^*$ (here E^* denotes the complex conjugate of E):

$$I = I_0 \exp\left(-\frac{z}{\Pi}\right). \tag{2.4}$$

Here, I_0 is a constant that quantifies the intensity at the interface. This quickly decaying wave field illumination makes the main interest of TIRF microscopy. Now that we have seen the theory underlying the functioning of our objective-based TIRF microscopy setup, we will see in more details how to use this piece of equipment.

2.1.2 TIRFM alignment procedure

The optical setup pictured in figure 2.1 required fine alignment, to ensure the quality of the illumination field. In this section, we describe the procedure used [100]. First, the mirrors, the beam expander, the diaphragm irises and the lenses were adjusted in z to the level of the rear port of the microscope. The elements

of the BE were mounted on a rail ensuring they shared the same optical axis. With the help of irises A1 and A2, the beam was finely aligned with the aforementioned axis using the adjustment screws of M1 and M2. M1 adjusts the position on A1 and similarly for M2 and A2.

To make sure the distance between the x10 objective and the lens L2 was appropriate, the outcoming beam was projected on a screen. The BE was calibrated when the projected spot size was no-longer dependent on the screen position, which meant the beam was collimated.

The lens L2 and the TIRFM-objective were then removed. The latter was replaced by a threaded-30-centimeter-long tube that featured irises at both ends, which we call A4 and A5. The goal of the next step was to make sure the beam was aligned with A3, A4 and A5. The beam was observed on a screen orthogonal to its axis, and located above the microscope. By closing A2, diffraction rings were observed. A3 was partially closed, so that the interference pattern becomes cropped. Adjusting M4, the center of the rings was aligned with the cropping window. This process was repeated by partially closing A4, then A5, and adjusting M5, then M6, respectively. Several iterations of this process were usually needed until the beam was aligned with A3, A4, and A5 at the same time.

The TIRFM-objective was finally mounted back on, as well as the lens L2, and the latter was aligned so that the beam projected on the screen at the vertical of the objective. At the end of this process, the beam alignment was done.

With the alignment procedure completed, we experimentally monitored the transition from plane-wave illumination to evanescent illumination in the following way. A small quantity of fluorescent dye solution, typically rhodamine or fluoroscein was spread between two microscope coverslips. Due to the small working distance of the TIRFM-objective, thin 150-µm-thick coverslips were used. Turning the laser on, a fluorescent spot was observed on the camera. Actuating the stepper motor, the translation stage was gradually moved and the beam was driven off the optical axis. While doing so, one noticed the increasing outcoming angle, and the spot observed on the camera also shifted slightly. As the incident angle gets close to criticality, the outcoming beam vanished and the fluorescent spot widened. When total internal reflection fully occured, the intensity of the fluorescent spot suddenly dropped.

The previous step was performed with the full camera sensor, covering a 112x94 µm observation window. The fluorescent spot size, by comparison, was approximately 25 µm in diameter. Hence, a cropped region of the sensor was used for actual experiments, corresponding to 23x22 µm square in the center of the sensor. This required to center well the illumination region which may have necessitated to adjust the camera position in the yz plane. The dye solution was finally replaced by the sample, which was ready for imaging at this point.

2.1.3 Incident angle measurement

The penetration length Π is a key quantity in TIRF microscopy for it fixes the resolution in the wall-normal direction z. With equation 2.3, the value of Π can be computed. In figure 2.5 (b) therefore we plot Π as a function of the angle for the typical values n_g = 1.518 and n_{sample} = 1.33. The penetration length was typically on the order of magnitude of the wavelength of the illumination light – shorter though – and decreased with increasing incident angles. While the finite numerical aperture of the TIRFM-objective lens imposes a minimum value for Π, in this case 64.5 nm, there was no theoretical upper limit for Π, since the quantity diverges close to criticality . However it proved experimentally difficult to work with theta too close to the critical angle – 62.1° under the aforementioned condition, or too close to the largest accessible angle – 74.1°. In practice θ was set between 64.4° and 69°, for penetration lengths roughly in the range between

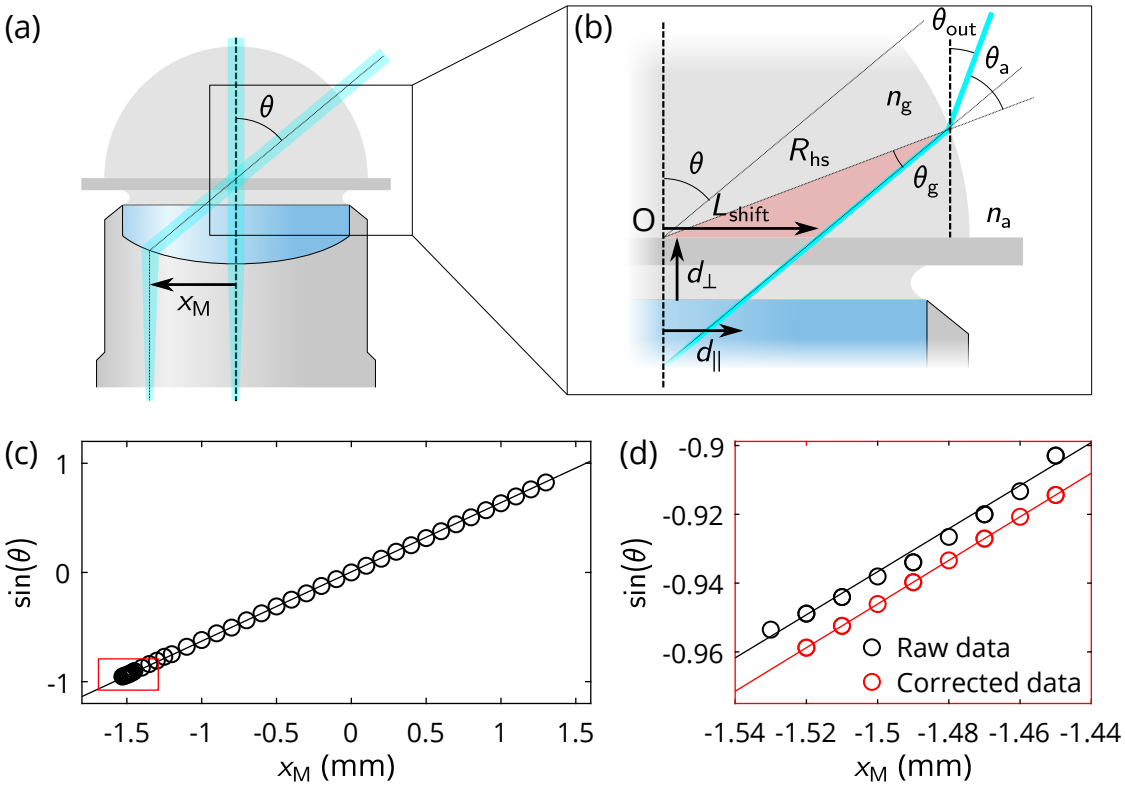

Figure 2.3: Hemisphere calibration experiment, with (a) a schematic of the setup and (b) a zoom in the region of interest to emphasize the refraction at hemisphere-air interface. A calibration curve is plotted in (c), and a zoom in the region of interest including the correction is shown in (d).

80 nm and 120 nm.

We said that the incident angle could be tuned by varying x_M, yet the actual value of θ was not known *a priori*. In this section, we exhibit two methods to measure θ and estimate Π. The so-called "hemisphere" method has already been described in the literature [90, 101], yet we provide here additional data as well as a discussion on the limitation of this method. It relied on the use of a an index-matched glass hemisphere, placed on top of the TIRFM-objective as sketched in figure 2.3 (a). This way, the light escaped the setup with an angle $\theta_{out} \approx \theta$, which could be measured macroscopically by projecting the beam on a horizontal screen above the setup. With a projecting distance of typically 1 m, and a spot size that was centimetric, we obtained a good precision on the output angle θ_{out}. Figure 2.3 (c) shows $\sin(\theta_{out})$ as a function of motor position x_M. The data are well fitted by a straight line of slope 0.626 ± 0.001 mm^{-1}, as expected from equation 2.1. The latter equation provides a measurement of the focal length of the TIRFM-objective lens: $f' = 1.052 \pm 0.003$ mm. This value is consistent with the typical order of magnitude expected for a 100x microscope objective lens.

We now discuss possible systematic errors that arised from the hemisphere method. The procedure described above was valid provided $\theta_{out} = \theta$, which would have been valid if 1 – there was perfect index matching between the TIRFM-objective lens, the immersion oil, the glass coverslip, and the hemisphere, and 2 – the center O of the hemisphere, and the focal point of the objective must have been located at the same spot. This latter condition may not have been perfectly met in this experimental setup, resulting in refraction at hemisphere-air interface as sketched in figure 2.3 (b). We now compute the output angle θ_{out} in the situation where the hemisphere was vertically shifted a distance $d_\perp$ vertically, and a distance $d_\parallel$ horizontally. We use Snell-Descartes law at hemisphere-air interface. Denoting θ_g and θ_a the incident and refracted angles, respectively, we have $n_g \sin\theta_g = n_a \sin\theta_a$. Using the law of sine in the red triangle of figure 2.3 (b), we have $L_{shift} \sin(\pi/2 + \theta) = R_{hs} \sin(\theta_g)$, with $L_{shift} = d_\parallel + d_\perp \tan(\theta)$. Finally noting that $\theta_{out} = \theta + \theta_g - \theta_a$, we can compute the following correction:

$$\theta - \theta_{out} = \arcsin\left(\frac{n_g}{n_a}\frac{d_\parallel \cos(\theta) + d_\perp \sin(\theta)}{R_{hs}}\right) - \arcsin\left(\frac{d_\parallel \cos(\theta) + d_\perp \sin(\theta)}{R_{hs}}\right). \quad (2.5)$$

Not surprisingly, this correction vanishes when $n_g/n_a \to 1$, or when $d_\perp/R_{hs}$ and $d_\parallel/R_{hs} \to 0$, which suggest that working with a large-radius hemisphere decreases this error. To make $d_\parallel$ as small as possible, we set $\theta = 0$ by projecting the outcoming beam as described before, and we made sure that the projected laser spot was located at the vertical of the TIRFM-objective with, and without the

hemisphere. The parameter $d_\perp$ was estimated to be the thickness of the glass slide on which the hemisphere was placed – 1.0 mm. To be rigorous, the distance that matters was not the front-lens-to-O, but the focal-point-to-O. Yet since the working distance of the objective was typically 100 µm, this quantity should be negligible compared to the slide thickness. The corrected sine of the angle, computed with $d_\parallel = 0$ and $d_\perp = 1$ mm is plotted in figure 2.4 (d), with emphasis in the region of interest for TIRFM. A best-fitting straight line was computed for the corrected data, which allowed to evaluate a corrected value of the incident angle. We discuss the relevance of this correction at the end of the section, by comparison with the other incident angle measurement method, described in the following.

The second angle measurement procedure is here referred to as the *in situ* calibration method. The principle is sketched in figure 2.4 (a): a solution of fluorescent dye was observed under TIRF illumination, with the full field of view. The experiment was performed with a flow of dye to prevent photobleaching. The TIRFM-objective was translated a distance δz_μ along the z direction with the objective piezomount over a total distance of typically 10 µm. When the objective moved, the fluorescence spot translated a distance δx_μ along x, as can be seen in figure 2.4 (b). For each δz_μ, a snapshot was recorded and the value of δx_μ was determined by 2-two-dimensional Gaussian fitting of the fluorescence spot. A set of experimental curves of δx_μ as a function of δz_μ, performed for different motor position x_M is shown in figure 2.4 (c). The data are always well described by straight lines, the slopes of which increase with x_M, *i.e.* with the incident an-

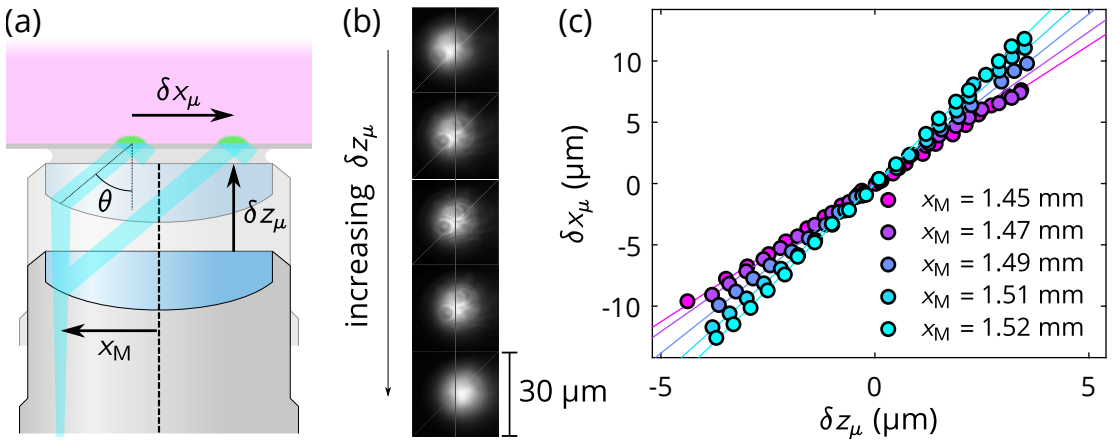

Figure 2.4: *in situ* angle calibration method, with (a) a schematics of the experiment and (b) a series of images illustrating the shifting of the fluorescent spot when the objective was translated in z. (c) shows experimental data for δx_μ as a function of δz_μ, for different incident angles.

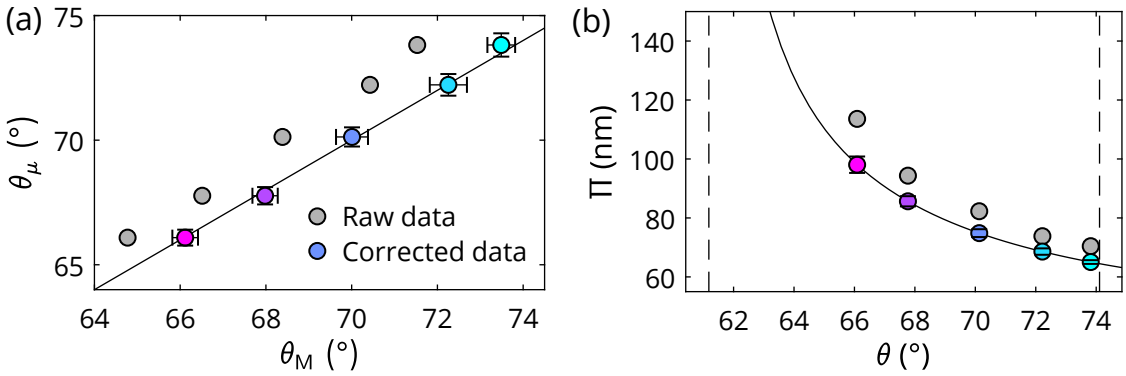

Figure 2.5: (a) Incident angle θ measured *in situ*, as a function of the same quantity measured with the hemisphere method, with (colored circles) and without (gray circles) refraction correction. The color map refers to the motor position as in figure 2.4, and the solid line indicates the $y = x$ line. (b) Theoretical penetration length Π as a function of θ. Vertical dashed lines indicate the critical angle (61.2°) and the largest angle allowed by the numerical aperture of the objective (74.1°). Colored circles show the Π value for the angle measured with *in situ* calibration, and gray circles show the associated Π values one would have obtained without taking into account the hemisphere correction.

gle θ. This observation can be rationalized by computing the geometric relation between δx_μ and δz_μ:

$$\delta x_\mu = \tan(\theta)\delta z_\mu. \tag{2.6}$$

Thus, the previously-mentioned slopes provided a simple measurement of θ.

Figure 2.5 (a) compares the hemisphere measurement θ_M and the *in situ* measurement θ_μ. The two methods are in good agreement, as emphasized by the collapse of the data on the $y = x$ curve, provided the refraction correction is applied for the hemisphere experiment. Not taking this correction into account lead to a systematic shift of typically 2° in θ. Figure 2.5 (b) shows the theoretical penetration length as a function of the incident angle according to the theoretical expression of equation 2.3. The values of Π for the previously-measured angles is displayed in colored circles, as well as the Π values one would have obtained without taking into account the hemisphere correction, in gray. For the smaller angle measured, the relative error in the estimated penetration length was 16 % and this number went down to 8 % for highest angles. This latter observation suggested that working further from the critical angle, where Π varies slower with θ, may be a good strategy for minimizing systematic errors when using the macroscopic angle-measurement method.

The *in situ* calibration developed for this system was precise, easy to perform – it can be automatized, no bias was identified, and most importantly it was a

local measurement. Particularly, this microscopic method can be performed in a microfluidic chip in the same condition as the associated experiment. For those reasons, this latter method was preferred for the rest of this work. In practice, this calibration was performed after each microfluidic experiment, by injecting a fluorescein solution in the chip, without changing the system otherwise.

Name	Description	Reference	Note
Optical table		Newport	
Laser		Gataca System iLaunch	λ = 488nm
M1, M2, M3	Mirror	Newport	ø 25.4 mm
M4, M5, M6	Mirror	Newport	ø 50.8 mm
A1, A2	Irise diaphragm	Thorlabs	
Obj	Microscope ojective lens	Leica Achro 10/0.25	NA= 0.25, 10x
L1	Converging lens	Thorlabs	ø 25.4 mm
L2	Converging lens	Edmund Optics ACH 25x200 MGF2 TS	
Motor	Motorized Linear Actuator	Newport NSA12	
Microscope	Inverted micorscope	Leica	
Camera		Andor Neo sCMOS	
TIRFM Obj	Oil immersion TIRFM-ojective lens	Leica HCX PL APO	NA= 1.46, 100x
Dichroic cube		Chroma	
Pzo	Piezoelectric scanner	Physik Instrument P-721 PIFOC	

Table 2.1: List of optical parts used for the TIRFM setup.

2.2 Microfluidics and microfabrication

Microfluidics is the science of manipulating fluids at the micrometric scale, which finds many applications: indeed downsizing systems usually means cheaper, faster and more integrated processes, which path the way to so-called "lab-on-chips" [102, 103, 104]. With the ability to design microreactors [105] or do single-cell analysis [106], microfluidics proves a powerful tool in chemistry and biology. Medical technologies are also an important domain of application, with diagnostics [107] or drug delivery [108]. The field has been booming in the 1990's thanks to progress made in microfabrication: the combination of photolithography, inherited from microelectronics, and elastomer molding gave birth to soft lithography [109]. This technology allows the fabrication of cost-effective microstructures with micrometric precision.

The most commonly used elastomer for this application is polydimethylsiloxane (PDMS), a transparent rubber-like material that features interesting properties for microfluidic applications. It is liquid at room temperature but cures when baked with cross-linking agent, which makes it easy to mold. Additionally it is inexpensive, transparent in UV-visible regions, chemically inert, bio-compatible, and seals easily to glass surfaces by plasma treatment. However this material also has its downsides: it swells when exposed to certain organic solvents [110] and it is permeable to water, causing issues [111] that led researchers to develop alternatives such as thermoplastic [112] or glass devices [113]. Being an elastomer, PDMS is finally a soft material, a key feature for the elasto-hydrodynamic study of chapter 4.

In this work, we used microfluidics as a way to generate laminar controlled flows in channels of controlled geometries. The first part of this section explains the in-lab microfabrication process, while the second part describes the peripheral microfluidic environment, that we used to drive flows and characterize chips.

2.2.1 Microfabrication

The soft lithography procedure used in this work was standard and is extensively described in a review by Xia and Whiteside [109]. It is beyond the scope of this study to discuss in details the underlying physical phenomena at play when performing soft lithography, however we will recall the main steps of the fabrication process, sketched in figure 2.6. The channel designe was drawn numerically with a dedicated software – here we used CleWin 5, and the negative was printed out using a photoplotter, which allowed micrometric precision in the in-plane patterns. A drawing of such a mask is shown in figure 2.7, courtesy

of Alexandre Vilquin. The following steps were performed in a clean room until mentioned otherwise, and all the experimental parameters (spin-coating speed, baking time, illumination settings...) were chosen according to the photoresist manufacturer recommendation for the desired channel thickness, and can be found in table 2.2.

A clean 4-in.-diameter silicon wafer was placed on a hot plate at 200°C for approximately 10 minutes to evaporate potential traces of water [114]. A photoresist of the SU-8 series (Microchem) was spin-coated (Polos 200 advanced) to obtain a layer of the desired thickness h_0, that will be the final channel height (step 1). The coated wafer was given a first bake ("soft bake") using a hot plate. The illumination was then carried out using an MJB4 mask aligner (SÜSS Microtech), in soft contact mode and with an illumination wavelength of 345 nm. Exposed areas of the photoresist crosslinked as a result of ultraviolet light exposure (step 2). A second bake was performed ("post-bake"), after which uncrosslinked photoresist was rinsed off by immersing the wafer in propylene glycol monomethyl ether acetate (PGMEA) for approximately 1 minute under gentle agitation (step 3). After a last rinse with isopropanol, a final bake ("hardbake") was performed at 200°C for approximately 10 minutes, in order to prevent delamination and crack formation in the cured photoresist.

The wafer was characterized by mechanical profilometry (Veeco Dektak 6M Stylus Profilometer) to measure the thickness of the newly built patterns. An example of such characterization is provided in figure 2.7 (a). Mechanical profilometry provided a measurement of the height profile along a line, like the one drawn in the inset. While the target thickness was 20 µm, the data revealed some inconsistency from chip to chip, which seemed to be dependent on chip

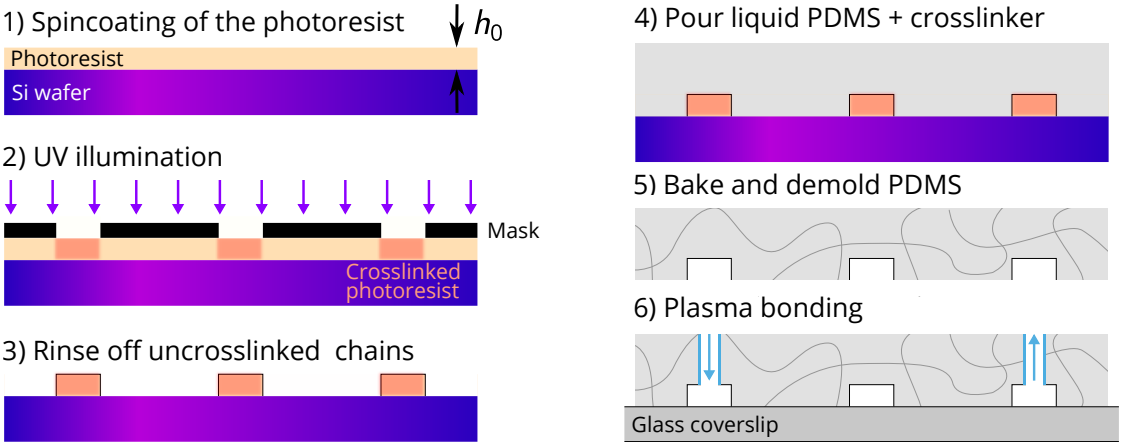

Figure 2.6: The different steps of the channel fabrication procedure by soft lithography.

Pattern	Straight	Serpentining
Length	4 cm,	8.8 cm
Width	{200, 500, 1000,2000 } µm	180 µm
Target Thickness	5 µm	20 µm
SU-8 reference	SU-8 2005	SU-8 2015
Spin-coating	3000 rpm for 30 s	2000 rpm for 30 s
Soft bake	2 min at 95°C	2 min at 95°C
UV illumination energy	100 mJ/cm^2	150 mJ/cm^2
Post-bake	1 min at 65°C and 3 min at 95°C	5 min at 95°C

Table 2.2: Experimental parameters for the soft lithography microfabrication procedure, for 20 µm- and 5 µm-thick depositions.

location on the wafer, as can be seen on figure 2.7 (c). Chips located in the central part of the wafer had a measured thickness of 16 µm, this number gradually increasing away from the center, up to 19.9 µm. We interpret this result by an non-homogeneous spin-coating. This observation also justified our efforts to characterize channel thicknesses, that are developed in section 2.2.2.

The following steps of the microfabrication process were no longer made in a clean room, but under a laminar flow hood. Commercial liquid polydimethylsyloxane (PDMS, Momentive RT 615) was prepared by mixing the base product with the crosslinking agent in a nine to one fraction, for a total mass of approximately 50 g. After vigorous hand mixing, the mixture was poured on the wafer, and the put under vacuum for at least one hour to evacuate air bubbles. Once bubble free, the melt was gently poured on the wafer and baked overnight at 70°C (step 4). The slab of PDMS was then gently demolded, and individual chips were cut apart (step 5). These chips could be conserved at least months with adhesive tape to protect the channel side, yet they were always cleaned with isopropanol before use. Inlet and outlet holes were punched to allow tubing connection. To do so, designs always featured circles with diameter 1 or 2 mm at inlet and outlet (see figure 2.7) (b)). The chips were finally plasma bonded (Femto Science CUTE) to a clean glass microscope coverslip (step 6). When submitted to an oxygen plasma, reactive radical sites were created at the surface of the PDMS and glass. Straight out of the plasma cleaner, the activated surfaces were put in contact, and covalent silicon-oxygen bonds ensured proper sealing [115]. Tubing was finally plugged in and the device was ready for use.

Two types of geometries were used. The first one consisted of a serpentining rectangular channel of length 8.8 cm, width 180 µm, and target height 20 µm. The second design was a straight rectangular channel, of length 4 cm, different

width comprised between 200 and 2000 µm, and target height 5 µm.

2.2.2 Microfluidics environment

To drive flows, we used a pressure controller (Elveflow OB1 mkIII+) that imposed a pressure, relative to the atmospheric pressure, in the 2-mL-reservoir containing the fluid of interest. The controller could also impose time dependent pressure pattern, compatible with a response time of approximately 0.1 s. Our model featured two independent channels that covered the 0 to 200 mbar

(a)

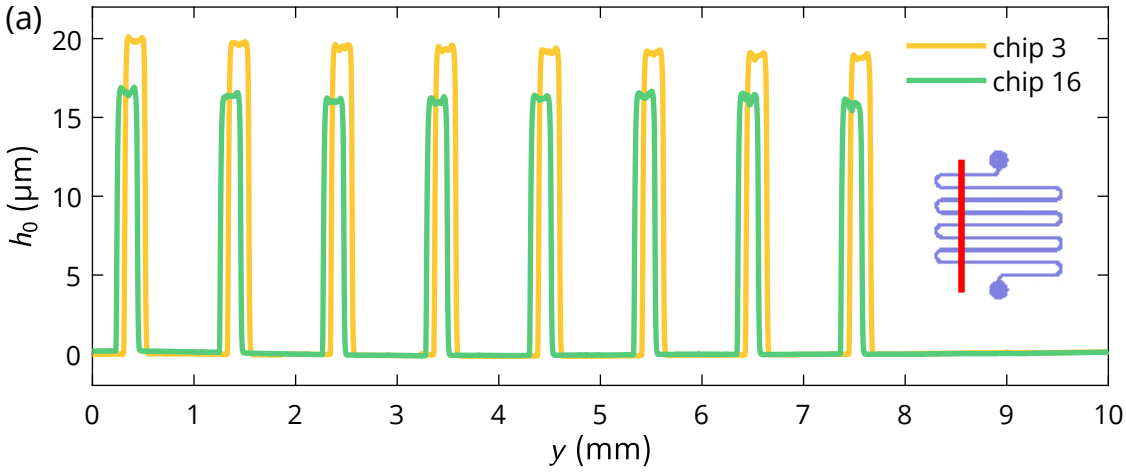

(b)

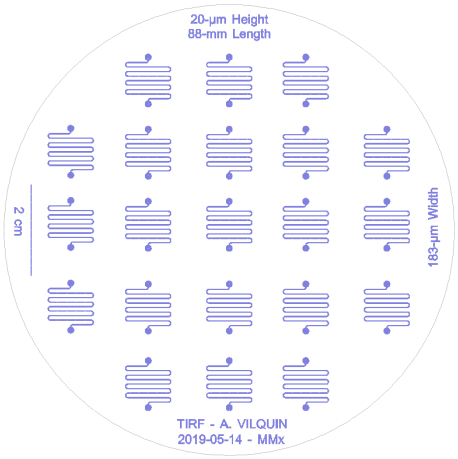

(c)

chip $\langle h_0 \rangle$	1 19.4	2 19.9	3 19.5	
4 18.1	5 16.3	6 16.2	7 18.6	8 18.9
9 18.4	10 16.5	11 16	12 16.2	13 20.1
14 18.9	15 16.7	16 16.3	17 17	18 19
	19 18.5	20 18.5	21 18.7	

Figure 2.7: Wafer characterization with (a) profilometry data. Each of the 21 channels of the wafer were characterized along a line pictured in red in the inset (only two curves are shown for clarity). In (b) is shown an image of the wafer design, from the software Clewin. Diagram (c) summarizes the mean channel height of each chip.

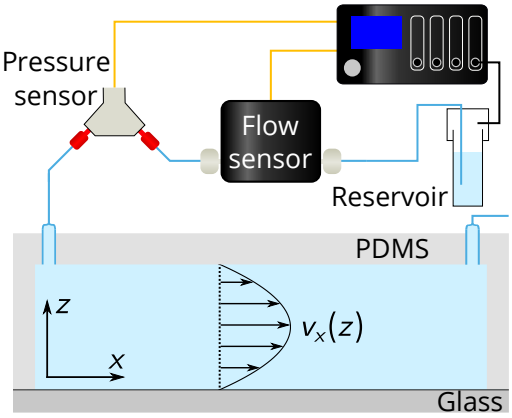

Figure 2.8: Schematics of the microchannel hydraulic resistance measurement, including a pressure and a flow sensor.

and 0 to 2000 mbar range. With the former being more accurate and the latter having a broader range, the best-suited channel was used depending on the application. The fluid was guided toward the chip with tubing (PEEK, IDEX 1581, inner diameter: 0.25 mm, outer diameter: 1/32 in.) of typical length inferior to 50 cm ensuring negligible hydraulic resistance.

For water driven in a 20 µm-thick chip, and at flow velocities compatible with TIRFM experiment, the Reynolds number typically ranged between 5×10^{-2} 5×10^{-3}, ensuring viscosity-dominated flows.

In this study we also used pressure and flow sensors (Elveflow MPS1 & MPS2, MFS1) with a set of appropriate microfluidic connectors. Gauge pressure sensors probed the local pressure, relative to atmospheric pressure, by measuring the deflection of a membrane using piezoelectric technology. They were calibrated before each use according the manufacturer's recommendation. The flow sensor worked by locally heating the fluid passing through a thin glass capillary, and measuring the downstream temperature. With simple fluids, this measurement unit did not require any calibration, but great care was taken in maintaining the cleanliness of the sensor. These sensors were not without impact on the flow, and a detailed discussion on that topic is provided in chapter 4.

With these sensors we measured the hydraulic resistance of microfluidic channels, using the setup schematically shown in figure 2.8. Ultra-pure water (Milli-Q, 18.2 MΩ cm, viscosity $\eta = 1.00 \pm 0.05$ mPa s) was driven in the system by imposing a constant pressure p in the reservoir. The two sensors measured the time-dependent flow rate $q(t)$ and pressure $p_0(t)$ at channel inlet. While the system displayed a finite relaxation time due to elasto-hydrodynamic effects described in chapter 4, it eventually reached a steady-state with a constant flow rate q_∞ and pressure $p_{0,\infty}$. Tuning p, we probed various steady-states.

2.3 Particle tracking velocimetry

Flow visualization is a key part of experimental fluid dynamics, and it is still an active field of research [116]. Relevant fields include among others biology, medicine, engineering, geology and climate science among others. Very early, smoke [117] or dyes were used to reveal flows at the macroscopic scale. Today many other techniques have been developed, such as hot-wire anemometry [118], laser Doppler-anemometry [119] or particle image velocimetry (PIV) [120], to name a few, each of them having there advantages and shortcomings [121]. Today, PIV a is popular pathway [122], that transferred well to microfluidic applications [123, 124]. Like most of the previously-mentioned methods, it rely on seeding the fluid of interest with tracers. The flow is then imaged with a digital camera, and each image is divided into subcells, within which the average flow is determined by image correlation.

In this study, we used particle tracking velocimetry (PTV). This method relies on similar principles as PIV, only here the trajectory of individual tracers is tracked. While this method requires more imaging and tracking sophistication [121, 123], it offers several advantages in the context of TIRFM experiment. Firstly one can work with low tracer fraction [125] for minimal impact on the flow. Second 3D-mapping [121] is made possible by tracer out-of-plane position inference. Finally, PTV has been shown to be more accurate near walls [125].

In this section we will go through the digital implementation of the lab-made PTV routines used to measure the near-wall flow profiles. The first part is dedicated tracer detection, and the second part describes the trajectory reconstruction algorithm.

2.3.1 Tracer detection

The tracers used in our experiment were carboxylate-modified polystryrene microspheres (Invitrogene FluoSpheres F8803), of radius $R = 55$ nm, and maximum emission wavelength $\lambda_{em} = 515$ nm. They were used as provided by the manufacturer (2 wt.%), at a fraction of 3 µL/mL in the fluid of interest. If the latter was a viscous fluid, homogenization of the tracers within the sample was achieved by gentle successive suctions with a the micropipette. In these conditions, the expected particle concentration is 8.6×10^{13} L^{-1}, for an average distance between tracers of typically 2 µm. This distance being roughly 40 times the radius of a particle, no hydrodynamic interaction between tracers is to be expected [126].

The tracer-containing solutions were driven in a microfluidic channel and observed under TIRF illumination. The camera recorded sequences of 2000 frames, in rolling shutter mode, at a rate $1/\Delta t = 400$ Hz, with 16-bit gray-level

encoding and 2.5 ms exposure time. With our 100x objective lens and with a real pixel size of 6.5 µm, the apparent pixel size, measured with a calibration grid, was 43.7 nm/pixel.

All the image processing and data treatment was performed with lab-made Matlab codes, notably using relevant image processing libraries. We are extremely grateful to Alexandre Vilquin for coding and sharing the aforementioned procedures. The first step of PTV was the detection, for each frame, of the positions (x,y) and fluorescence intensities (I) of visible tracers. A typical TIRF microscopy raw image is shown in figure 2.9 (a). The noise level was approximately 100 on the camera gray scale, and the brightest particles reached 10 000, covering two orders of magnitude in fluorescence intensity measurement. In our experimental conditions, these intensity levels correspond to particles located within a distance of one micron from the channel bottom wall.

To detect tracers, each image was 2D band-bass filtered [127], with spatial cutoff frequencies of 1 pixel^{-1} and 10 pixel^{-1}. The pixels below a threshold value, determined manually for each experiment, were then set to zero. Figure 2.9

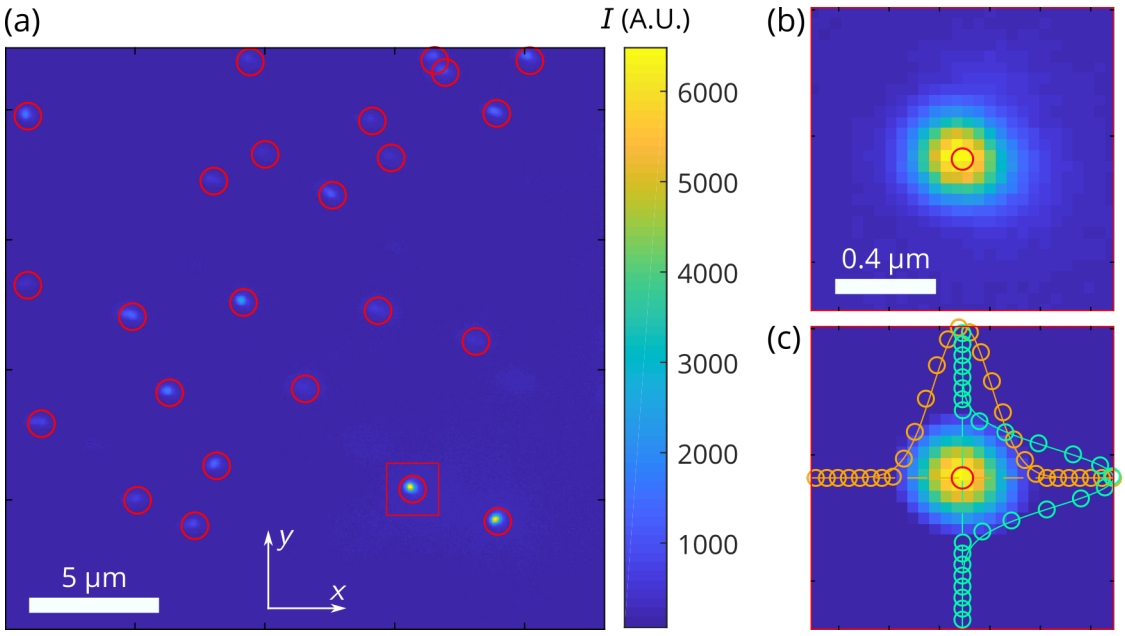

Figure 2.9: Particle detection protocol. (a) shows a raw image of fluorescent particles observed under TIRF illumination, with detected tracers highlighted with red circles. A zoomed view of the framed particle is provided in (b). (c) displays the same image, after filtering and thresholding. The orange and green curves are x and y profiles along the center of the particle, with associated Gaussian fits.

shows a zoomed view of a tracer (b) before and (c) after filtering and thresholding. The non-zero clusters – indicating the presence of a tracer – were detected using the *regionprops* function, and 2D-Gaussian fitted according to the following equation:

$$I(x, y) = a_1 + a_2 \exp\left(-\frac{(x - a_3)^2 + (y - a_4)^2}{2a_5^2}\right), \tag{2.7}$$

where the $\{a_i\}$ are the fitting parameters. Orange and green curves in figure 2.9 (c) show cuts of the particle intensity profile along x and y, respectively, with the associated best-fit profiles. Although fitting 10^5 particles required some computational power, this method was preferred for its accuracy. On the image of figure 2.9, 24 particles were detected, as highlighted with red circles. This number corresponds to an average distance between tracers of 4.6 µm, which compares reasonably to expected value for this concentration. With a sub-micron observation zone, this small density also prevents overlapping of particles in the z direction.

Back to figure 2.9, the Gaussian fit describes the data well, and enabled sub-pixel determination of the tracers' positions a_3 and a_4, as well as good precision in peak intensity evaluation a_2. On the example of figure 2.9 (c) the width of Gaussian fit was $\sigma_{\text{tracer}} = 115$ nm, this number being weekly dependent, with the peak intensity. We attempt to rationalize this observation in the context of diffraction. Because the tracers were approximately a fifth of the wavelength in diameters, they can be considered point-like sources, meaning that the intensity

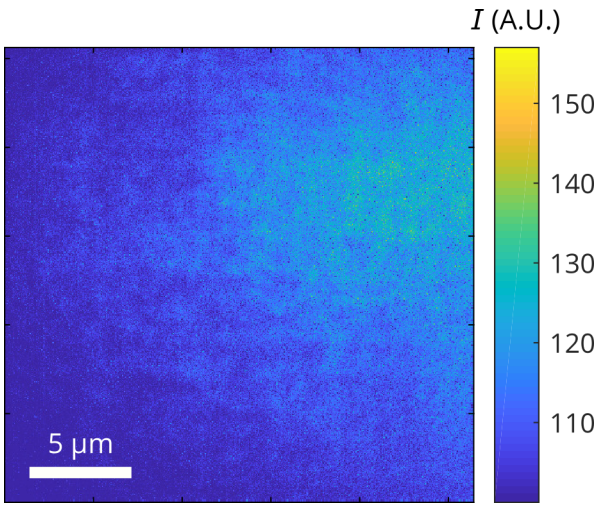

Figure 2.10: Temporal minimum stack for an experimental video, recorded during a TIRFM experiment. The particles vanished, revealing the illumination inhomogeneity.

profile observed on the camera is the point-spread function (PSF) of the TIRF-objective lens. Such PSF is often approximated by a Gaussian function, and in the non-paraxial case, valid for high-NA systems, the theoretical standard deviation reads [128]:

$$\sigma_{\mathrm{PSF}} = \frac{\lambda_{\mathrm{em}}}{2\pi n_{\mathrm{g}}} \left(\frac{4 - 7\cos(\theta_{\mathrm{max}})^{3/2} + 3\cos(\theta_{\mathrm{max}})^{7/2}}{7(1 - \cos(\theta_{\mathrm{max}})^{3/2})} \right)^{-1/2} . \tag{2.8}$$

The numerical application with NA = 1.46, n_{g} = 1.518, and θ_{max} = 74.1° gives σ_{PSF} = 76 nm. Thought σ_{tracer} and σ_{PSF} have the same order of magnitude, two arguments can be thought of to explain the discrepancy. The first one is optics: with $2R/\lambda_{\mathrm{em}} \approx 0.21$, it could be that the PSF is not perfect approximation of the particle diffraction pattern. Furthermore, the full spectrum of emission of tracers includes larger wavelengths, up to 650 nm according to the manufacturer, which should enlarge the diffraction figure. The second argument relies on Brownian motion. Because they are small objects, tracer-particles are subject to random diffusion in all direction of space, and the apparent intensity profile results the integration of the static diffraction pattern over the exposure time. Our estimate based on Stokes-Einstein relation suggests that, in our experimental conditions, a tracer particle diffuses a distance comparable to its own diameter over the acquisition time of the camera, making this effect non-negligible.

We now discuss the bias induced by non-homogeneous illumination in the context of our TIRFM experiments. Indeed for a Gaussian beam that was not large compared to the observation zone, the intensity field was higher in the center than at the edges of our images. This could cause an inaccurate determination of tracers' fluorescence intensity, leading to in-plane discrepancy of the particle's estimated altitude . To quantify this non-homogeneity, we did as follow. Since the dichroic cube inside the microscope was not ideal: a fraction of the laser intensity was directly reflected toward the camera. Thus the signal measured when the laser was on, but without any fluorescent object in the observation window, provided an estimate of the spatial illumination fluctuation. In practice, this information could even be obtained in the presence of tracers, by performing a temporal minimum stack of a recording, *i.e.* by keeping the lowest intensity measured by each pixel over time. Such images, like the one shown in figure 2.10 indeed revealed non-homogeneous gray level, with fluctuations of order of 10 %. With $\log(1 + 10\%) \approx 0.095$, the relative error on $\log(I)$, was inferior to 3 %. In practice, no difference was noticed in velocimetry data with or without this background correction, hence it was not applied in the following.

2.3.2 Trajectory reconstruction

The trajectory reconstruction problem is the following: for a given list of particles at frame n, which particles of frame $n+1$ might they correspond to ? There are algorithms available to answer this question numerically, notably relying on the Hungarian algorithm. In this work, we used the *simpletracker* [129] function, which could handle gaps, *i.e.* reconstruct a trajectory even if the particle is missing in one or several frames. We adapted this routine to keep track not only of the position of a particle along its trajectory, but also of its fluorescence intensity. Figure 2.11 (a) shows a chronophotography of a the motion of a particle. The experiment was performed in a glass-PDMS microchannel of length 8.8 cm,

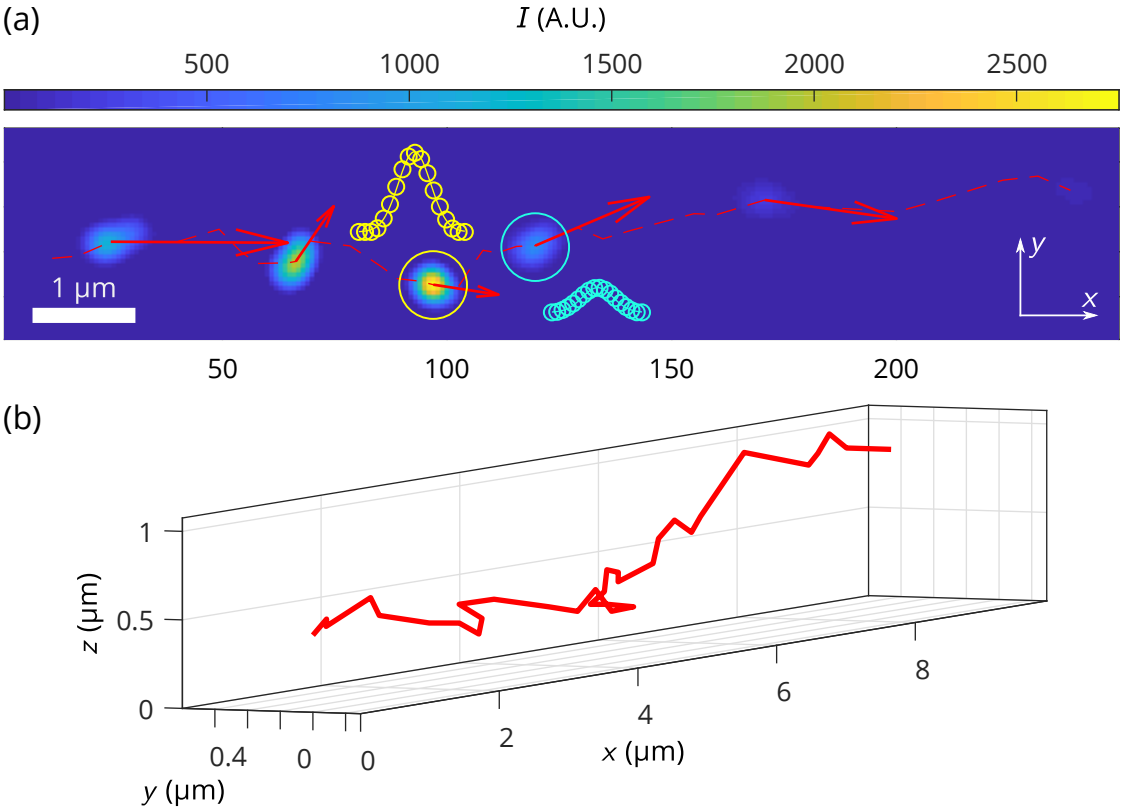

Figure 2.11: Particle tracking procedure. (a) Chronophotography of a particle advected by a flow in the x direction, observed under TIRFM illumination. The particle is shown every 6 frames, *i.e.* 15 ms. The dashed line shows the trajectory, reconstructed with our tracking protocol, and the arrows show the instantaneous velocities, in arbitrary units. The Gaussian intensity profile at two different instants is also shown. (b) reconstructed 3D-trajectory, z being computed from the intensity I using equation 2.4, with Π = 124 nm and $\log(I_0)$ = 10.64.

width 180 µm and height 20 µm, under a shear flow in the x direction, generated by a 40 mbar pressure drop across the channel. The figure displays the particle position every 6 frames, *i.e.* every 15 ms. The dashed line shows the trajectory, reconstructed with the previously mentioned procedure. Arrows represent the instantaneous velocity in arbitrary units.

From the previous data, we were able to compute the 3D trajectory of the particle. The fluorescence intensity fluctuations, visible in figure 2.11 (a), encode the motion of the particle in the wall-normal direction: $z = \Pi(\log(I_0) - \log(I))$. The penetration length $\Pi = 124$ nm was obtained from the *in situ* angle calibration method and equation 2.3, and intensity at the wall $\log(I_0) = 10.64$ was evaluated with a method detailed in section 3.1. A 3D-visualization of such trajectory is shown in figure 2.11 (b).

A selection of trajectories are plotted in figure 2.12 for (a) $p_{\text{in}} = 20$ mbar and (b) 70 mbar. All the trajectories show displacement fluctuations, due to diffusion mentioned in section 2.3.1. Tracer particles are thus subject to two transport phenomena: advection by the flow, that is deterministic, and diffusion, that is stochastic. The full motion of particles is governed by an advection-diffusion equation, which reveals a dimensionless number, know as the Peclet number Pe, which compares the relative weight of the two transport mechanisms. Namely, one has:

$$Pe = \frac{v_x R}{D_0}, \tag{2.9}$$

where D_0 is the diffusion coefficient of the tracers, given by Stokes Einstein's

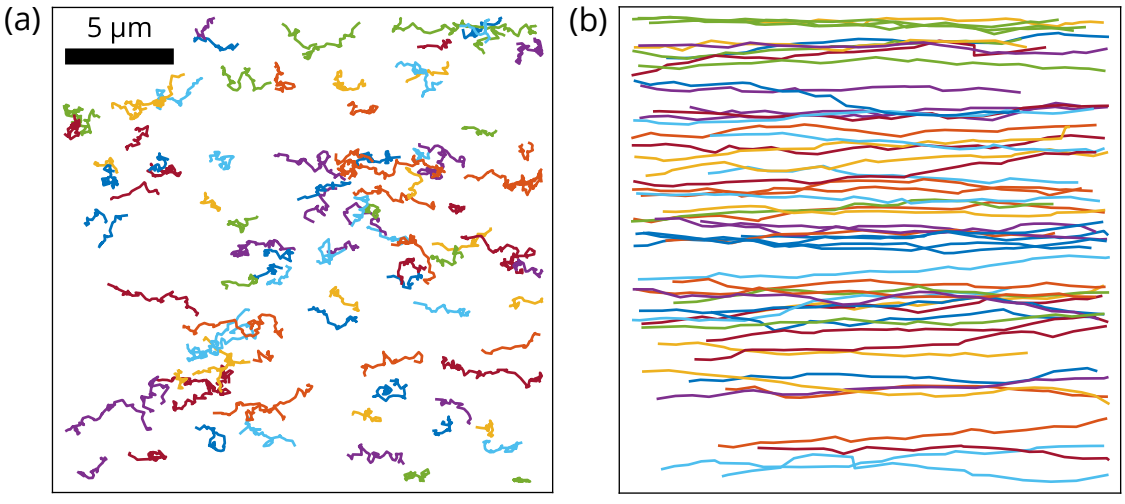

Figure 2.12: Selection of reconstructed trajectories for flows driven by (a) a 20 mbar pressure drop and (b) a 70 mbar pressure drop.

relation:

$$D_0 = \frac{k_B T}{6\pi\eta R} . \tag{2.10}$$

Here, k_B is the Boltzmann constant and T is the absolute temperature. In figure 2.12 (a), $Pe \approx 0.3$: diffusion dominates and the trajectories look fluctuating, while in 2.12 (b), $Pe \approx 5$: advection dominates and trajectories look ballistic.

The trajectories are segmented into N individual displacement events, computed between two consecutive frames, $\{[\delta x_i, \delta y_i, \delta \log(I)_i]\}_{i=1...N}$. To each of these jumps is associated a $\log(I)_i$ value that is averages along the displacement. Before moving on to velocimetry, the data are cleared of supposed outliers: jumps associated to objects that are too small, two large or non-circular, for example, are sorted out. At the end of this process, typically 30 000 displacement events are observed for each 2000-frames video. In a TIRFM experiment, 4 to 10 videos are recorded for a given set of experimental parameters *e.g.* the pressure and polymer concentration.

2.4 Polymer solution preparation and characterization

2.4.1 Sample preparation procedure

The polymer used in this study were polyacrylamide (PAM) and hydrolyzed polyacrylamide (HPAM), the molecular structure if which is sketched in figure 2.13. They were synthesized in lab by RAFT/MADIX polymerization (courtesy of Mathias Destarac, Université Toulouse - Paul Sabatier), according to a protocol detailed in the literature [130, 131]. The samples were also characterized by the manufacturer and their main features – number-averaged molar mass M_n and polydispersity index – are summarized in table 2.3. The latter were measured by size exclusion chromatography coupled with multiangle light scattering, and as explained here [130]. Solutions were made by mixing solid polymers in a solvent, either ultra-pure water (Milli-Q, 18.2 MΩ cm) or NaCl solutions (Sigma Aldrich,>99 %), using an orbital shaker at 60 rpm for at least 24 hours. Target concentrations were achieved by dilution of such solutions with their associated solvent. The refractive index of the solution was measured (Atago refractometer). The results for PAM(2082k) are plotted in figure 2.14, and reveal a linear relation between n_{sample} and the concentration in the [0 - 8] g/L range, with a slope 1.6×10^{-4} L/g. The data point at 16 g/L is off the line and indicates a possible sublinear increase for the large concentrations. For our samples, and for TIRFM application, the effect was computed to be negligible.

Standard rotational rheometry measurement were performed (Anton Paar MCR 302) in a Couette cell, in continuous shear mode, in the [1-1000] s^{-1} range. Such measurements were made to characterize the polymers, prior to each TIRFM experiments, with the same sample as for velocimetry.

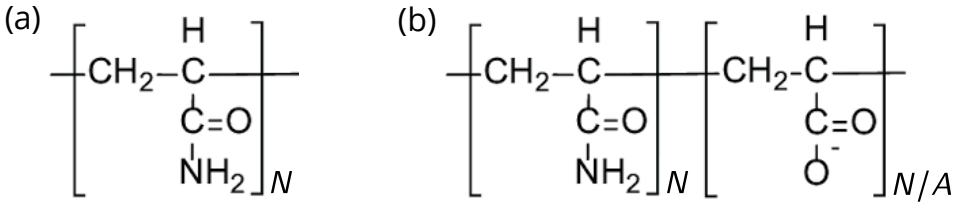

Figure 2.13: Molecular structure of (a) PAM and (b) HPAM.

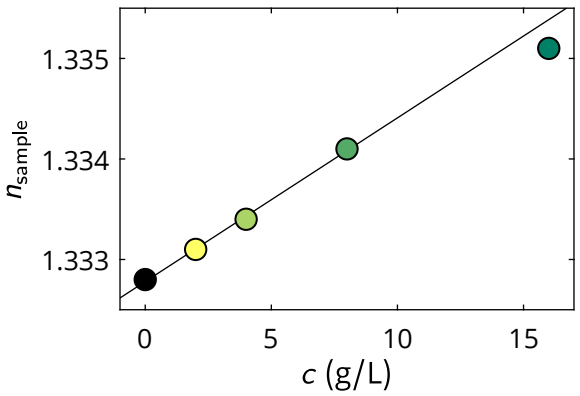

Figure 2.14: Refractive index of PAM(2082k) solutions, as a function of the concentration. The black line is a linear fit of the data, excluding the last data point.

2.4.2 Rheological characterization

The rotational rheometry results are shown in figure 2.15 for a selection of (a) PAM(2082k) and (b) HPAM(817k[-]) solutions of different concentrations c. While not shown here, data were also collected for PAM(1284k) and show a behavior similar to PAM(2082k). We first turn our attention to neutral polymers. The measured viscosity increases with concentration, and shear thinning is observed for concentrated enough solutions. The curves display a Newtonian plateau of viscosity η_0 at low shear, and a power law decrease at high shear [25]. To characterize this behavior, we used a model available in the literature [132], specifically developed for the prediction of PAM and HPAM rheological behavior, which we now describe.

The model relies on two parameters that depend only on the chain properties, solvent, and temperature: the intrinsic viscosity $[\eta]$, and a time scale τ_d. The intrinsic viscosity was first determined for both PAM(1284k) and PAM(2082k). Denoting η_s the solvent viscosity, and η_{sp} the specific viscosity, defined as $\eta_{sp} =$

Designation	M_n (kg/mol)	Polydispersity index	Electric charge
PAM(1284k)	1284	1.05	Neutral
PAM(2082k)	2082	1.07	Neutral
HPAM(817k[-])	817	1.09	[–],10 %

Table 2.3: Characteristics of the PAM samples used in this study.

$(\eta_0 - \eta_s)/\eta_s$, the intrinsic viscosity $[\eta]$ is expected to follow the following behavior:

$$\eta_{sp} = c[\eta] + 0.667(c[\eta])^{1.31} + 0.026(c[\eta])^{4.72} . \tag{2.11}$$

This model is a higher order development of the definition of $[\eta]$ as the ratio η_{sp}/c in the limit of low-c regime. η_{sp} as a function of c is plotted in the inset of figure 2.16 (a), for PAM(1284k) and PAM(2084k). Using $[\eta]$ as the only adjustable parameter in the latter equation, the experimental data were fitted and we obtain, $[\eta]$ = 0.35 L/g and $[\eta]$ = 0.52 L/g, respectively. The main figure shows the associated normalized data, *i.e.* η_{sp} as a function of $c[\eta]$, along with the model of equation 2.11, which describes well the data.

Full $\eta \; vs. \; \dot{\gamma}$ curves where then fitted with a Carreau model of the form:

$$\eta(\dot{\gamma}) = \eta_\infty + (\eta_0 - \eta_\infty)\left(1 + (\tau_{rheo}\dot{\gamma})^\kappa\right)^{(n-1)/\kappa} , \tag{2.12}$$

where η_∞ denotes the viscosity at high shear rate, τ_{rheo} is characteristic time scale, the inverse of which quantifies the onset of shear thinning, n is the shear thinning exponent, describing how fast viscosity decreases with the shear rate, and κ characterizes the transition from Newtionian to shear thinning. In this study, we take $\eta_\infty = \eta_s$, *i.e.* 1.0 mPa s, and κ is arbitrarily set to 2. n is imposed as follow:

$$n = 1 - (0.796 - 0.687 \exp(-0.059 c[\eta])) , \tag{2.13}$$

which leaves τ_{rheo} as the only fitting parameter as this stage. As can be seen in figure, 2.15 (a), this model fits the data well for all the tested solutions, and τ_{rheo} is plotted as a function of $c[\eta]$ in the inset of figure 2.16 (b). The data were fitted with the following model:

$$\tau_{rheo} = \tau_d \left(1 + 0.04 \left(c[\eta]\right)^{2.4}\right) , \tag{2.14}$$

which serves as our experimental determination of the parameters τ_d. We obtain τ_d = 1.0 and 1.8 ms for PAM(1284k) and PAM(2084k), respectively. The normalized data τ_{rheo}/τ_d as a function of $c[\eta]$ collapse well on the model of equation 2.14, as can be seen in main figure 2.16, (b).

Overall, this empirical model provides a good description of our experimental data. It can be used to predict the rheological behavior of our PAM sample. Once the parameters $[\eta]$ and τ_d experimentally determined, the model allows to predict the viscosity for any shear rate and concentration.

We now explore the physical meaning of these parameters. $[\eta]^{-1}$ has the dimension of a concentration, and it is a good approximation of the overlap concentration, which is the reason why the dimensionless quantity $c[\eta]$ is sometimes referred to as the overlap parameters. More precisely, one has $[\eta]$ =

$\phi_\infty \langle r^2 \rangle^{3/2}/M$, where ϕ_∞ is called the Flory constant, $\langle r^2 \rangle$ is the mean square end-to-end distance of the chain, and M is its molecular weight [133]. Assuming a scaling of the form $\left(\langle r^2 \rangle\right)^{1/2} \propto N^\nu$, for the chain size, we have $[\eta] \propto N^{3\nu-1}$. With Flory exponent $\nu = 3/5$ for a linear chain in good solvent [11], our data verifies this scaling remarkably: $\frac{[\eta]_{1284k}}{[\eta]_{2082k}} \left(\frac{2082}{1284}\right)^{3\nu-1} \approx 0.99$. We can also extract typical chain sizes from this calculation, taking $\phi_\infty \approx 2.8 \times 10^{23}$, we have $\langle r^2 \rangle^{1/2} \approx 116$ and 156 nm for PAM(1284k) and PAM(2084k), respectively.

τ_d can be seen as the relaxation time of the polymer chains in the dilute limit, a quantity usually captured by the Zimm relaxation time τ_Z [11]. Computing the theoretical Zimm time $\tau_Z \sim \eta_s \langle r^2 \rangle^{3/2}/k_B T$ for our two samples, we obtain 0.40 and 0.95 ms, comparing reasonably to experimental values $\tau_d = 1.0$ and 1.8 ms.

Moving on to rheology curves of HPAM(817k[-]) figure 2.15 (b), we notice that similar range of viscosities is achieved at much lower concentration. The shear

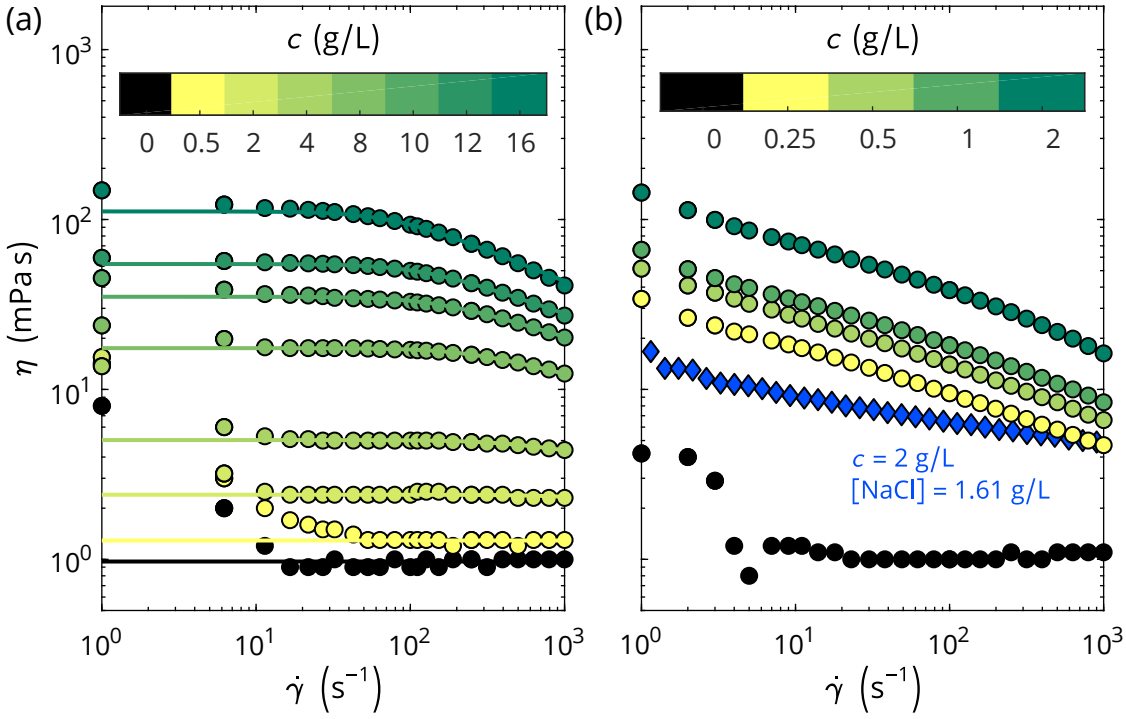

Figure 2.15: Viscosity *vs.* shear rate curves measured by standard rotational rheometry in a Couette cell for various (a) PAM(2082k) solutions and (b) PAM(817k[-]) solutions, at different concentrations. In (a), solid lines represent the fits of the data, according to the Carreau-like model described in [132]. In (b), the blue curve shows the data obtained for $c = 2$g/L with addition of salt, [NaCl] = 1.61 g/L.

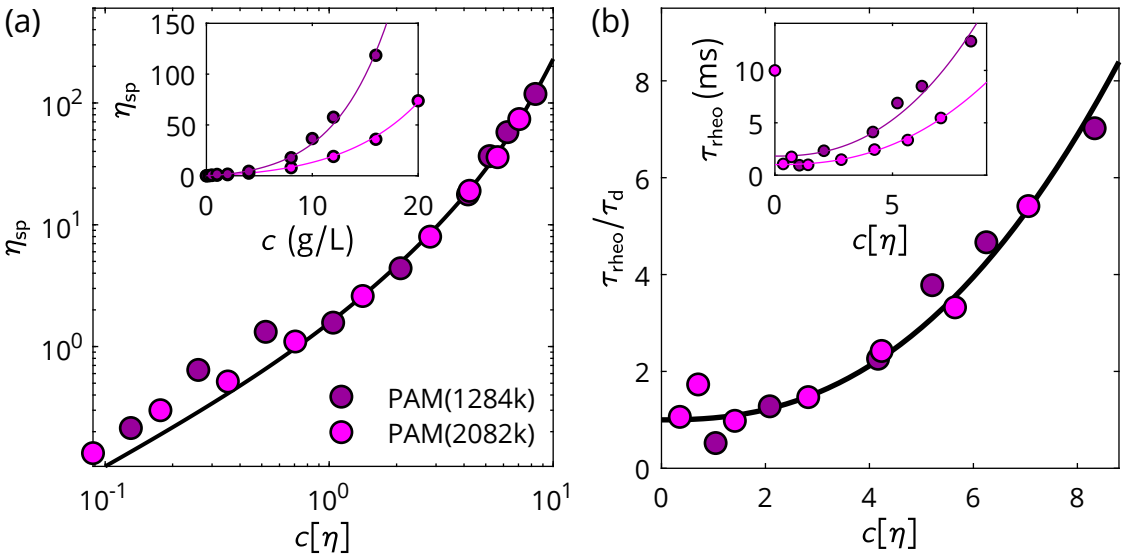

Figure 2.16: Fitting parameters for the Carreau-like model. (a) specific viscosity as a function of the overlap parameter, for two neutral PAM solutions. The solid black line is the model of equation 2.11. The intrinsic viscosities were determined by fitting the η_{sp} *vs.* c curves as shown in the inset. (b) normalized relaxation time as a function of the overlap parameter. The solid black line is the model of equation 2.14. The normalizing time τ_d was obtained by fitting the τ_{rheo} *vs.* $c[\eta]$ curves as shown in the inset.

thinning behavior is also observed all along the accessible range of shear rates. Experimentally this means the Newtonian plateau viscosity could not be measures, make all the previous analysis out of our range. This also suggests that the charged samples have a larger chain size and longer relaxation time than their neutral counterparts. Polyelectrolytes indeed show specific scalings, due to monomer-monomer electrostatic repulsion [18]. We will go deeper into this topic in the next sections. When electrostatics is at play, ionic strength plays a significant role. This is exemplified by the blue curve of figure 2.15 (b), performed with the addition of NaCl, at a concentration of 1.61 g/L. Qualitatively, the presence of salt screens the electrostatic repulsion between monomers, making the chain size smaller, end hence a lower viscosity for the same number of chains.

Conclusion of the chapter

The second section of this manuscript went through equipment and procedures used to measure near-surface flows of polymer solutions in controlled confined environments. Firstly we have seen how to assemble and use a total internal reflection fluorescence microscopy for evanescent wave illuminations of our samples. After that we have described the fluidic part of the experiment, with microchannel fabrication by soft lithography and flow control protocols. Thirdly we have explained our flow mapping technique based on particle tracking velocimetry. Finally gave seen how to make poly(acrylamide) and hydrolyzed poly(acrylamide) solutions, and characterize them with rotational rheometry. With these tools we now move on to the next chapter, where the rheology and the hydrodynamic boundary conditions of polymer solutions are investigated.

Chapter 3

Microscale velocimetry in polymer solutions

With the experimental tools and procedures described in the previous chapter, we now move on to the results obtained for several simple and complex fluids. Various information can be extracted from TIRFM experiments, but here we will mostly focus on the mean velocity of the tracers, which is assumed to be a probe of the local flow profile. After careful analysis of typical experiments in water and water-glycerol mixtures in section 3.1, we treat the case of PAM and HPAM solutions. In section 3.2.1, we first show how, by measuring the local shear rate for a controlled imposed shear stress, TIRFM velocimetry can be used as a local microrheometer. Then in section 3.2.2 we investigate the hydrodynamic boundary condition for polymer flows, and highlight the crucial wall of electric charges.

The results shown in this chapter were published *Sofft Matter*, and involve the work of A. Vilquin, N. Sanson, S. Jouenne, F. Restagno and J. D. McGraw [134].

3.1 A calibration experiment in Newtonian fluids

To start off, we focus on a typical TIRFM velocimetry experiment, performed in ultrapure water in a 8.8 cm long, 180 µm wide and 16.5 µm thick microchannel. In figure 3.1 (a) is shown the velocity profile, *i.e.* the streamwise velocity v_x as a function of the distance z to the wall, for a flow driven at 35 mbar. The velocity were computed over two consecutive frames: $v_x = \delta x/\Delta t$, where δx is the distance traveled between two images, and $\Delta t = 2.5$ ms is the inverse of the acquisition rate. This graph includes the data of five 2000-frames recordings for a total of approximately 2×10^5 displacement events. The cloud of point shows the velocity, computed of each individual jump, as a function of z or $-\log(I)$. For clarity, only one percent – randomly picked – of the data points are displayed. To

compute z we used a penetration length of 86 nm measured with the *in situ* calibration method described in section 2.1.3, and $\log(I_0) = 10.16$. The evaluation of the latter quantity is described later in this section. Particles are observed only in the 180 nm $\leq z \leq$ 620 nm region. The upper boundary is set by our limited observation area: with the exponential decay of the illumination field, no signal can be measured more than a few penetration lengths away from the wall. The lower boundary is due to electrostatic interactions between the wall and the particles. Immersed glass develops a negative electric potential of typically −60 mV in our experimental conditions, according to data available in the literature [135, 136]. The tracer-particles being also negatively charged, with a zeta-potential of the same order of magnitude [137], they are repelled from the glass, leaving a tracer-free depletion layer close to the wall.

The experiment also reveals scattered data points. This is due to the Brownian nature of the tracers: the particle motion are subject to random diffusion around the local flow motion. The statistical physics involved in this phenomenon is a topic on its own, and our experimental setup is well suited for its investigation [88], but for now we will focus on average quantities. To kill

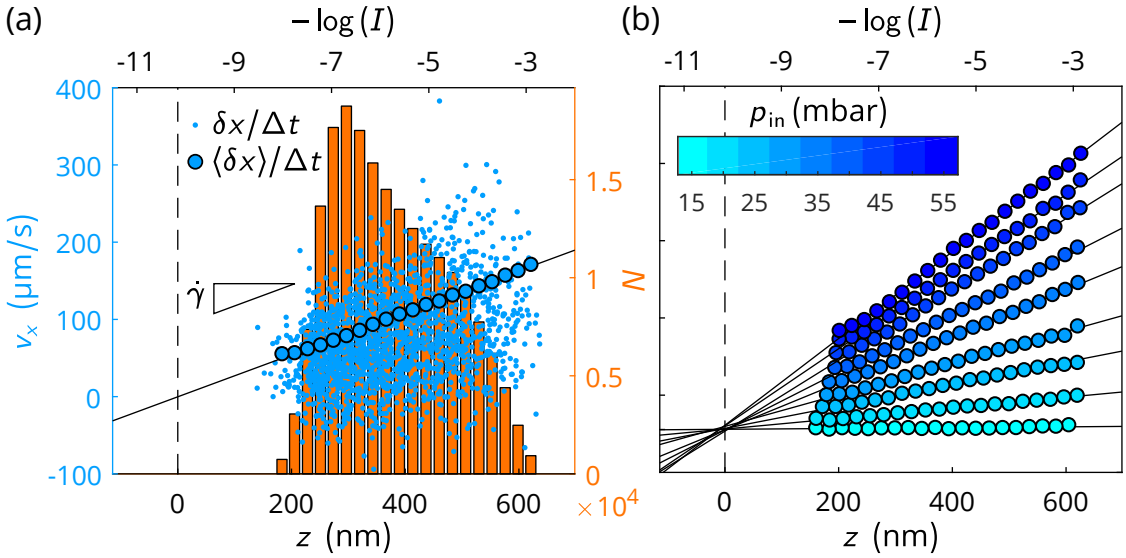

Figure 3.1: (a) Sample of individual velocities (points) and mean velocity (circles) of tracked particles as a function of z and $-\log(I)$, for a flow of water in a microfluidic channel. The bar chart indicates the population within each intensity bin used for the averaging. The straight line is a linear fit of the mean velocity, whose slope is a measurement of the shear rate. The experiment was performed at p_{in} = 35 mbar, in a 8.8 cm long, 180 µm wide and 16.5 µm thick microchannel. (b) Mean velocity profiles for flows at different pressures.

these fluctuations and help visualize the flow profile, the observation window is divided in 20 equally sized layers parallel to the bottom wall, of typical thickness 0.25 $\log(I)$ unit *i.e.* 22 nm. The average velocity within each bin is plotted in blue circles, and the bar chart displays the population of each bin. The latter histogram is the experimental particle intensity distribution along z. It indicates that the tracer are not equally spread within the observation window. The fine shape of this distribution is non-trivial and can be rationalized using the statistical physics of particle ensembles close to a repellent wall, optics and particle polydispersity [101, 88].

The mean velocity profile is well fitted by a straight line, the computation of which takes into account the relative population involved in each data point. The slope of this line is a measurement of the near-wall shear rate $\dot{\gamma} = \partial v_x/\partial z$. The linearity of the mean flow profile is in accordance with Poiseuille flow theory. Indeed with a small viewing window compared to the channel height, we observe the linearization of the predicted parabolic velocity field. In these experimental conditions, the expected deviation from linearity is less than 4 % at the furthest from the wall.

Doing this experiment for different input pressures, we obtain the mean velocity profiles of figure 3.1 (b). The best-fitting lines cross at single point of zero velocity, which serves as our definition of the no-slip plane, wall position,

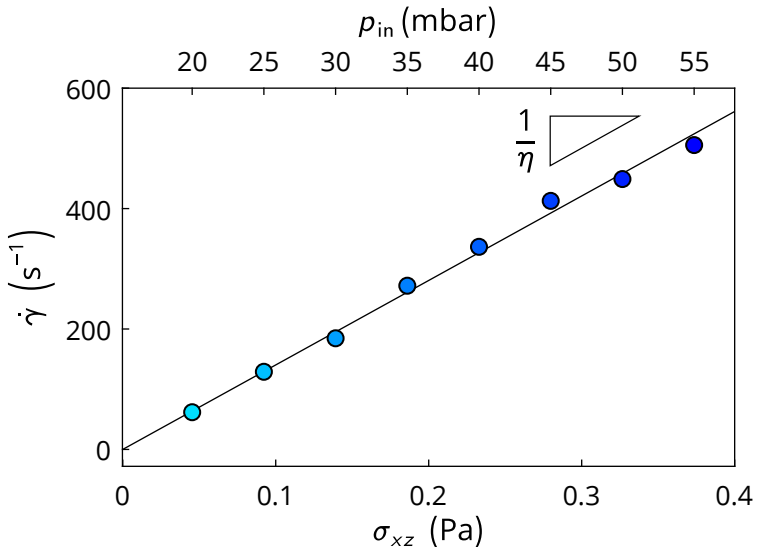

Figure 3.2: Experimental shear rate as a function of pressure and shear stress, for a flow of water in a microfluidic channel. The best fitting straight line is a measurement of the fluid viscosity. The color map is the same as that of figure 3.1.

and definition of $\log(I_0)$. This choice was made under the assumption of no-slip at the wall, which is the most natural hypothesis for water on hydrophilic surfaces [138, 139].

The experimental shear rate is plotted as a function of shear stress in figure 3.2. For a rectangular channel of constant height h_0 and length L, the near-wall shear stress σ_{xz} is proportional to the pressure drop across the channel: $\sigma_{xz} = (p_{\text{in}} - p_{\text{hs}})h_0/2L$. In this formula, p_{hs} denotes the hydrostatic pressure correction (1 mbar/cm) arising from the fact that the liquid reservoir where the pressure was set was at a lower altitude than the microscope stage. In practice p_{hs} was set such that the linear fit of the data cuts the stress axis at zero shear rate. Here we have p_{hs} = 15 mbar. The data is well fitted by a straight line, which is consistent with Poiseuille flow theory. The inverse of the slope provides a measurement of the fluid viscosity. We obtain η = 0.72 ± 0.03 mPa s, the error estimate including uncertainties on the penetration length, channel geometry, and fit. This value is smaller that the accepted value [140], and cannot realistically be explained by a rise in temperature. To account for this bias, here assumed systematic, such velocimetry experiment was always performed prior to complex fluid analysis, for calibration purpose.

With such calibration done, experiments were also performed with water-glycerol mixtures. Such solutions are often used when it comes to work with fluids of different viscosities [141]. Figure 3.3 (a) shows the shear rate as a function

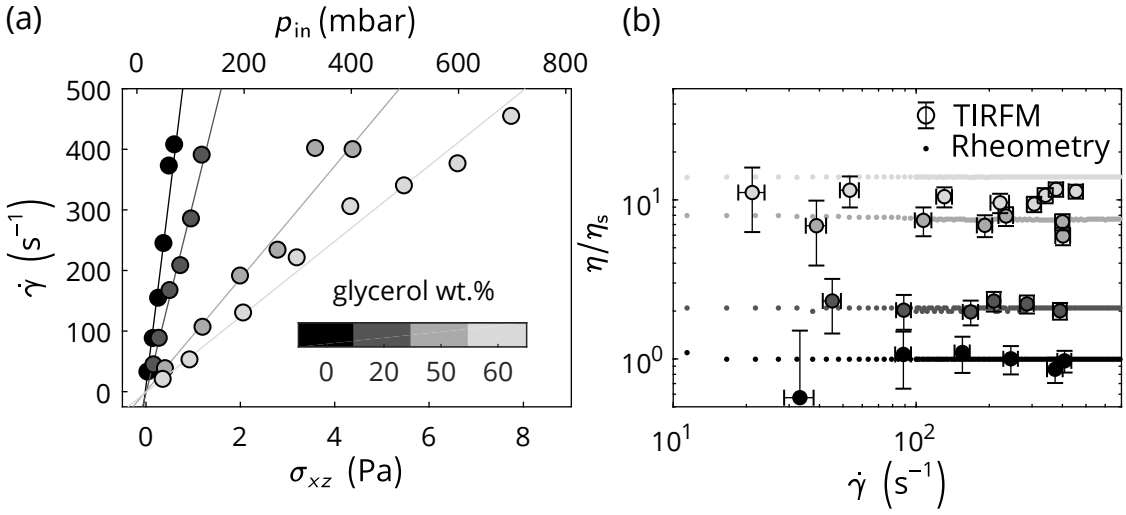

Figure 3.3: (a) Shear rate *vs.* shear stress for various water-glycerol mixtures, with best-fitting straight lines. (b) Normalized viscosity as a function of shear rate, for the same mixtures. Rotational rheometry data are superimposed for comparison.

of the shear stress for water glycerol at different weight fractions, as indicated. These experiments were performed with 200 nm diameter tracer particles, and the change in refractive index with glycerol content was taken into account in the evaluation of the penetration length. Like for water experiment, the shear rate increases linearly with the shear stress, indicating the Newtonian behavior of the fluids.

The viscosity, defined by $\eta = \sigma_{xz}/\dot{\gamma}$ and measured with TIRFM velocimetry were compared to the bulk rotational rheometry data, measured in a Couette cell. The normalized viscosity η/η_s, where η_s denotes the viscosity of pure water measured in the same conditions, is plotted as a function of the shear rate in figure 3.3 (b). For all the tested mixtures, the viscosity is constant in the accessible range of shear rates, and increases with the glycerol fraction. Once normalized, the data obtained with both instruments are in good agreement.

We now list some physical limiting factors of TIRFM velocimetry that may explain the observed discrepancy between the measured viscosity of water and the generally accepted value. Equation 2.4 used to compute z from $\log(I)$ does not take into account two important effects. If there is polydispersity, a larger object will be interpreted closer to the wall than a smaller counterpart at the same position. Similarly, due to finite depth of field of the objective (≈ 350 nm), out of focus objects will appear less bright than those in focus, independently of the evanescent illumination. These phenomena bias the estimation of the altitude z of the tracers, and therefore the shear rate evaluation. Additionally, hydrodynamic effects have been suspected to arise due to the finite – and relatively large – size of the tracer particles [87]. The hydrodynamics of a sphere close to a rigid wall is a difficult problem that has been extensively studied [126, 142]. The associated effect are expected to decrease on a scale of the order of the sphere radius. Here, the particles are located at least 4 radii away from the wall, which should prevent such hydrodynamic coupling with the wall.

In this section we have seen how TIRFM may be used to image the flow profile near the bottom glass wall of a microfluidic channel, in the case of Newtonian fluids. The velocity profiles are locally linear, and two practical quantities are extracted from the linear fit the of data. The slope provides a measurement of the interfacial shear rate, while the intercept at null velocity provides the wall position. While the former allo to access the rheological properties of the fluid, the latter will be crucial to study the hydrodynamic boundary conditions, as we will see in section 3.2.2. In the next section, we turn our attention to polymer solution flows.

3.2 TIRFM in polymer solutions

3.2.1 Microrheology

In TIRF microscopy experiments with complex fluids, a calibration was required. Such calibration was achieved by performing the experiment in pure water prior to injection of the fluid of interest. We recall the injection procedure: a tracer-containing water solution was first injected in the microfluidic channel, and velocimetry measurements were performed for different pressures as described in the previous section. Then, the polymer solution was injected in the chip until completely filled, and measurements were carried out in the same way. Finally, a dye solution was injected in the chip to perform the *in situ* calibration of the

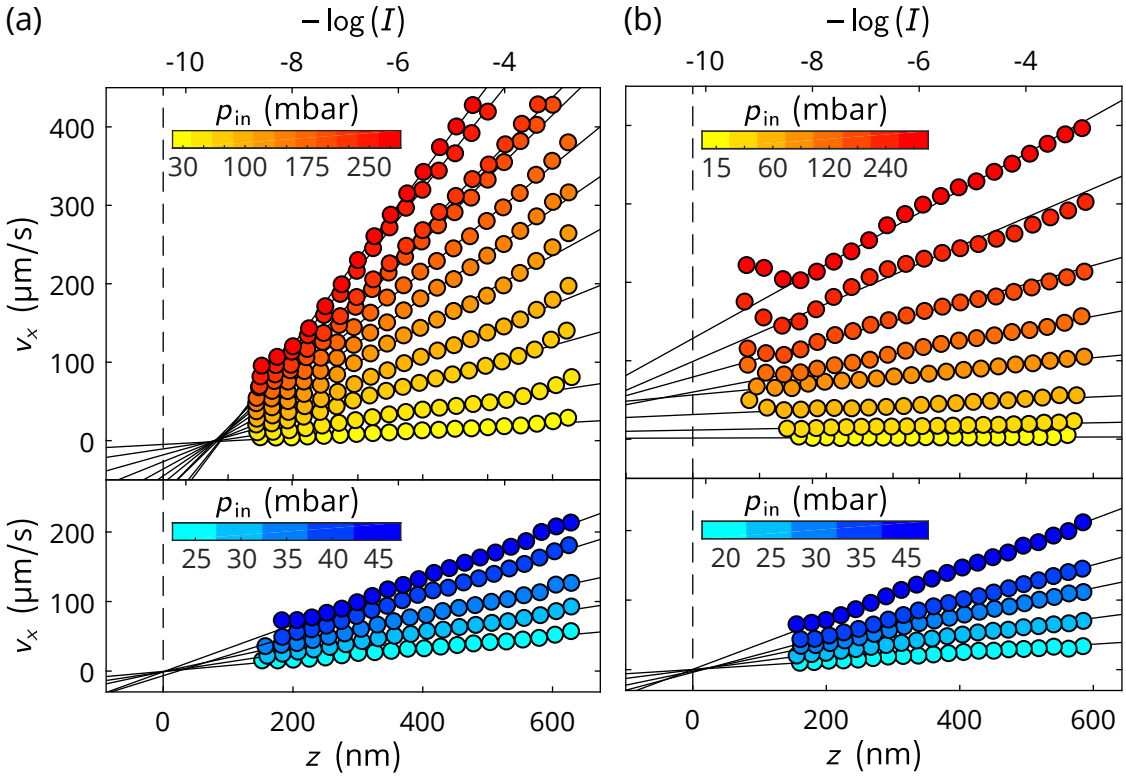

Figure 3.4: Pressure dependant velocity profiles, *i.e.* streamwise velocity as a function of z – or, equivalently – $\log(I)$ – for (a) a PAM(2082k) solution at 2 g/L and (b) an HPAM(817k[-]) solution at 0.5 g/L. The reference experiment performed in water is shown under each graph. Black straight lines are linear fits of the data, and the dashed lines represent the position of the bottom wall of the channel, extracted from the calibration experiment.

incident angle. Figure 3.4 shows a set of velocity profiles at different pressures for (a) a PAM(2082k) solution at a concentration of 2 g/L and (b) an HPAM(817k[-]) solution at 0.5 g/L. Under each graph is displayed the associated calibration experiment. These calibrations allow to determine the wall-position, or $-\log(I_0)$, as the altitude where the profiles linearly intercept to zero velocity. The quantity $\log(I_0)$ is assumed to be sample-independent, since all the liquid used in these experiments have similar optical indexes. The shear rate *vs.* pressure relation for this water experiment also allows to measure the solvent viscosity η_s and hydrostatic pressure p_{hs}. All the data shown here are well described by straight lines, from which we extract the shear rate $\dot{\gamma}$ and the slip length b, *i.e.* the distance at which the streamwise velocity linearly extrapolates to zero.

To start, we turn our attention to the shear rates. Like in the pure water case, the relation between the shear rate and the pressure relation provides information on the viscosity of the fluid. We use the same definition for the viscosity $\eta = \sigma_{xz}/\dot{\gamma}$ with the shear stress given by $\sigma_{xy} = (p_{in} - p_{hs})/2L$. The normalized viscosity η/η_s is plotted as a function of the shear rate in figure 3.5, for different so-

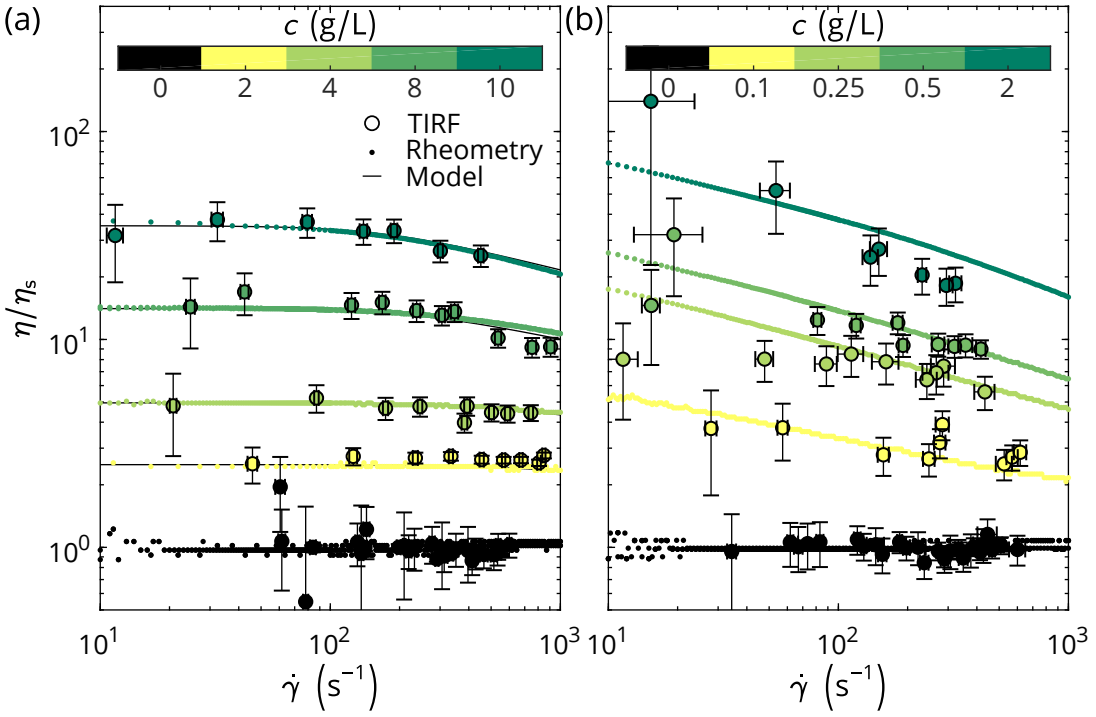

Figure 3.5: Scaled viscosity as a function of the shear rate for different solutions of (a) PAM(2082k) and (b) HPAM(817[-]). Circles show the measurements obtained by TIRF velocimetry, while dots are rotational rheometry data. For PAM(2082k) the model described in section 2.4.2 is also displayed.

lutions of (a) PAM(2082k) and (b) HPAM(827k[-]). The rotational rheometry data, performed with the same solution, are also plotted. For both solutions, the velocimetry captures well the rheological behavior. For PAM(2082k), the predictive model described in the previous section is also displayed. We use the parameters obtained independently in the rheometry experiment $[\eta]$ = 0.52 L/g and τ_d = 1.8 ms, and the plateau viscosity η_0 is extracted from the rheometry data. Parameters n and τ_{rheo} are computed from equations 2.13 and 2.14. The model also describes the data well.

We now discuss an important possible bias in the TIRFM velocimetry data. In chapter 4 we describe how a pressure gradient applied in a PDMS-made microfluidic chips may induce deformation of the channel. This effect causes a pressure- and x-dependent channel thickness, a quantity used to compute the local shear stress. In other words, the formula $\sigma_{xy} = (p_{in} - p_{hs})/2L$ breaks down. In extreme cases, if the applied pressure is high enough to deform the channel significantly, this would result in an apparent shear thinning. The data shown here do not take into account this phenomenon, however corrected data are provided at the end of chapter 4, where channel deformation is discussed in depth. In this case, the effect affects only the most concentrated data, where highest pressures are required, and the correction is within errorbars.

Overall, and upon proper calibration, we have a good agreement between global bulk rheometry, local near-wall velocimetry and empirical model available in the literature. We will see in the next section that being able to measure *in situ* the rheological property of the fluid of interest will prove crucial to rationalize the apparent slip boundary condition in polymer solutions.

3.2.2 Boundary condition measurement

We now move on to the study of the flow boundary conditions over the bottom glass surface of the microfluidic channel. For neutral polymers similar the PAM(2082k) sample of figure 3.4 (a) we observe that the velocity profiles do not cross at zero at the wall, but a distance $D = 77 \pm 6$ nm within the channel. We interpret this observation by the presence of immobile layer of adsorbed chains, which shifts the no-slip plain. The impact of such a polymer layer on the flow profile is not trivial, but it has been theoretically shown that the situation depicted here is relevant [62]. This hypothesis is also corroborated by the reported adsorption of PAM on oxyde-based surface, in multiple contexts [30, 143, 31]. Furthermore, the experimental measurement of the adsorbed thickness D is close to the expected bulk size of PAM(2082k) chains in solution.

No clear dependence of D with concentration was identified, but the data indicate that D increases with chain length. For PAM(1284k) we have $\langle D_{1284} \rangle = 46 \pm 11$ nm, and for PAM(1284k) we have $\langle D_{2082} \rangle = 84 \pm 9$ nm. The thickness of

the adsorbed layer for polymers exposed to attractive surfaces is a question that was addressed by De Gennes [56], the result was that the characteristic length over which the near wall monomer concentration gradient builds up is the bulk correlation length in the semi-dilute regime, that should be significantly shorter that the bulk chain radius. Here we should be more precise when speaking of adsorption layer thickness. Considering that D is an extrapolation length, one should speak of hydrodynamic thickness. In the same paper, and by solving the flow equation within the adsorbed layer, De Gennes predicted that this hydrodynamic thickness indeed scales like the radius of gyration of the chain, in accordance with our data. The results also suggests that the thickness of the adsorbed polymer layer is not – or little impacted by shear. This is not trivial since we have seen that bulk chains change configuration under flow. Other experimental studies suggest that grafted change size under flow [144].

Moving on to polyelectrolytes, the profiles for HPAM(817k[-]) shown in figure 3.4 (b) displays the opposite behavior, with positive streamwise velocity at the wall, characteristic of slippage. Extrapolating the linear fits for these profiles to zero velocity, we measure the slip length b. Unlike the previously-mentioned adsorbed layer thicknesses, b is pressure- and concentration-dependent. In figure 3.6 we show b as a function of the driving pressure for four different concentrations. The slip length consistently increases with concentration and decreases with the pressure – *i.e.* the shear rate.

To rationalized these data, a model for slip of polymer solutions on a glass surface is needed. We use the stratified framework described in section 1.3.2. The model is based on the following ingredients: 1- an electrostatically medi-

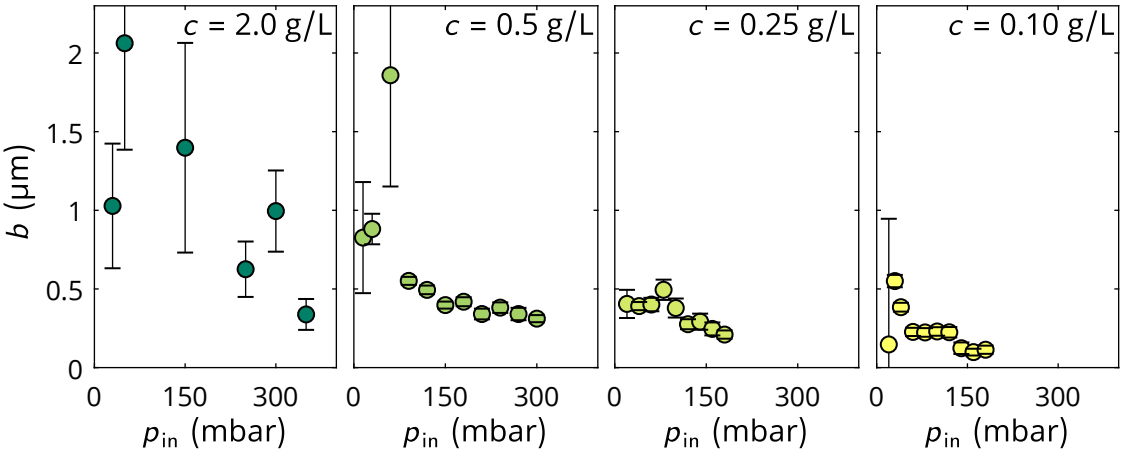

Figure 3.6: Experimental slip length as a function of the driving pressure, for four solutions of HPAM(817k[-]), with concentrations ranging between 0.1 and 2.0 g/L.

ated polymer concentration profile in the wall-normal direction, 2- scaling laws for polyelectrolyte chain conformation in the semi-dilute regime, and 3- non-Newtonian behavior of the flowing liquids.

The first ingredient relates to the chain-wall interaction. The polyelectrolyte nature of HPAM comes from partial hydrolyzation of amide groups, leaving a fraction $1/A$ of negatively-charged monomers, as depicted in figure 2.13. For our sample, and according to the supplier, the value of A, *i.e.* the average number of monomers between two charges, is approximately 10. As mentioned previously, the bottom wall of the channel is made of glass, which also gets negatively charged in water [135, 136]. Thus one can expect electrostatic repulsion between the chains and the wall. For such non-adsorbing surface, Joanny *et al.* computed the theoretical polymer concentration profile along z, for semi-dilute solutions [145]. The latter ranges from 0 to bulk concentration over a typical length ξ, the bulk correlation length of the polymer. As often when it comes to polymer physics, we will now rely on scaling arguments.

The situation can be simplified as depicted in figure 3.7 (a). A chain-free depletion layer expends over a thickness ξ, above which the polymer is at bulk concentration. Because the local viscosity is lower in the depleted zone, and by continuity of the shear stress, the velocity profile is expected to be shaped as depicted, with high shear close to the wall, and lower shear in the bulk. We assume the depletion layer to be essentially water-like, with a viscosity η_s and without any slip at the bottom wall. Extrapolating the bulk profile, an apparent slip arises, with a slip length scaling as follow:

$$b = \xi \left(\frac{\eta}{\eta_s} - 1 \right) . \tag{3.1}$$

This picture generalizes to any situation where a near-wall lubrication layer develops with a different viscosity from that of bulk.

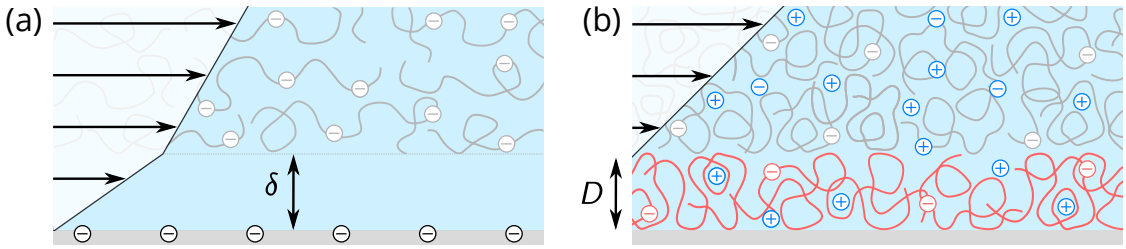

Figure 3.7: Schematic view of polymer flow boundary conditions. (a) apparent slip situation arising from electrostatic-driven depletion layer. (b) Adsorbing case, where a layer of immobile chains shifts the no-slip plane up. In the present situation, adsorption is supposed to result from the screening of the electrostatic repulsion due to the presence of salt (blue charges).

With that picture in mind, we now need a scaling for the correlation length ξ. For polyelectrolytes, specific interactions due to the presence of charges change the scalings as compared to the neutral case. Dobrynin *et al* computed scaling laws for charge-containing polymers in various regimes [18]. We place ourselves in good solvent conditions, without added salt, and we denote a the monomeric size, $\tilde{c}$ the monomer concentration, and $l_B = e^2/\varepsilon_0 k_B \Theta$ the Bjerrum length. The latter arises from balancing the thermal and electrostatic energies, and here e is the elementary charge, ε_0 is the dielectric constant, k_B is the Boltzmann constant and Θ is the absolute temperature. By adding monomer-monomer electrostatic repulsion to the standard excluded volume interaction, Dobrynin showed that polyelectrolyte chains adopt a rod-like conformation in the dilute regime, from

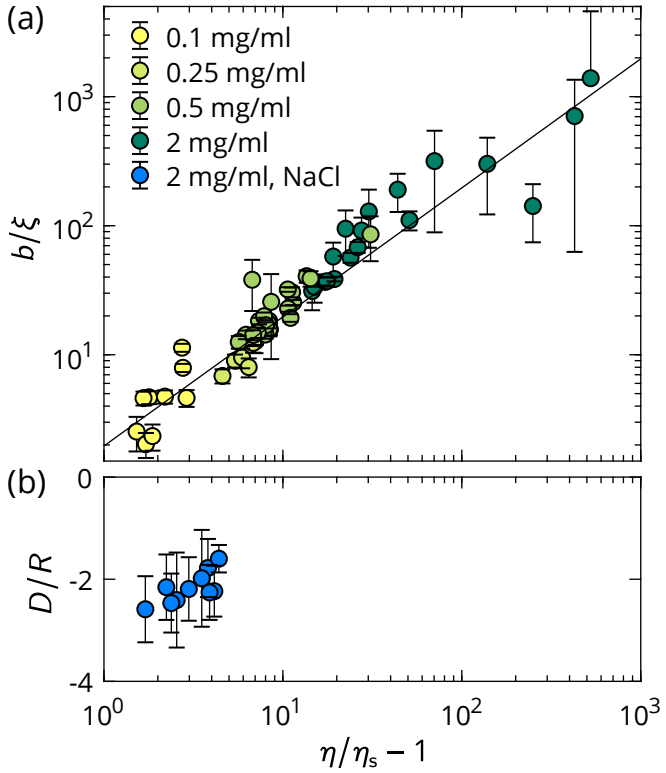

Figure 3.8: (a) slip length normalized by the polymer correlation length as a function of the specific viscosity, all measured during TIRFM experiments. The graph includes the data for four solutions of HPAM(817k[-]), with concentrations ranging between 0.1 and 2.0 g/L. The black line indicates the best slope-one fit of the log of the data. (b) adsorption layer thickness, normalized by the chain size, as a function of the specific viscosity for an HPAM(817k[-]) solution at 2.0 g/L including 1.61 g/L of salt.

which the following scaling scaling for ξ can be calculated:

$$\xi \sim \sqrt{\frac{A^2}{\tilde{c} l_B}} \propto c^{-1/2} . \tag{3.2}$$

The correlation length decreases with the concentration, which is understandable qualitatively: the more chains there are per unit volume, the more often chains encounter each other. One may notice that this scaling is different from the uncharged case, where, for good solvent, we have $\xi \propto c^{-3/4}$ [11]. Taking M = 71.08 g/mol for the acrylamide monomer molar mass, we obtain N = 1.15 $\times 10^4$ repeat units, from which we evaluate $\tilde{c}$. With polyelectrolyte concentrations ranging from 0.1 to 2.0 g/ L, and taking l_B = 0.71 nm, we have ξ comprised between 11 and 48 nm. Since tracer particles of TIRFM experiments cannot be imaged that close to the wall, flows properties are only accessible in the bulk region of figure 3.7 (a).

Using this scaling for ξ we plot the normalized slip length b/ξ as a function of the specific viscosity $\eta/\eta_s - 1$ for four different HPAM(817k[-]) solutions in figure 3.8 (a). Here both x and y axis quantities are TIRFM-measured. The data collapse a straight line of slope 1 in logarithmic scale, validating the scaling of equation 3.1. We also find a prefactor ($\approx$ 2) of order unity, which validates the order of magnitude for ξ. The collapse of the data also suggests that the entire dependence of b in the shear rate is included in the viscosity. In other words this means that the correlation length is independent of the shear rate, according to this modeling.

Finally, to emphasize the importance of charge in this problem, the experiment was also carried out with an HPAM(817k[-]) at a concentration of 2.0 g/L in the presence of NaCl at a concentration c_s = 1.61 g/L. In this situation the velocity profile displays a chain-sized adsorbed layer, that is independent on the shear rate, as shown in figure 3.8 (d). For the chain radius we also took the scaling from reference [18]:

$$R \sim a N^{1/2} \left(\tilde{c} a^3\right)^{-1/4} B^{-1/4} \left(1 + 2A c_s/\tilde{c}\right)^{-1/8} , \tag{3.3}$$

where $B = \left(a l_B^{-1} A\right)^{2/7}$ is shown to be the ratio of the chain contour length to chain size, in the dilute regime, for a good solvent. Taking $a \approx$ 1 nm, we have $R \approx$ 171 nm. This observation supports the hypothsesis of a charge-mediated depletion layer leading to apparent slip. When salt is added in large quantity, the charges are screened which we makes the behavior of polyelectrolytes more neutral-like, explaining adsorption by analogy with neutral PAM experiments. In other words, the salt concentration is a way to experimentally tune the apparent slip length.

In this section we have applied TIRFM velocimetry to neutral and anionic PAM and HPAM solutions, at different concentrations, and under various flow rates. The setup captured well the shear-thinning behavior of our sample solutions, while simultaneously accessing the slip length, with a macromolecular resolutions. Electrostatic interactions where shown to be crucial in rationalizing the hydrodynamic boundary conditions. Attractive surfaces cause chain adsorption, shifting the no-slip plane inside the channel. Conversely, in the case repulsive walls we observe apparent slip which can be explained by the presence of a lubrication layer that scales with the inverse square root of the polymer correlation length. Having characterized near-wall flow behaviors, we may now turn our attention to the impact of these effects at the scale of the whole channel.

3.3 Toward global flow measurements

So far, we focused on local flow mapping to measure hydrodynamic boundary conditions. Yet we have seen in section 1.3.3 that another possible route to indirectly access slip lengths, is to measure the flow rate within a thin channel. For rectangular channels in Hele-Shaw conditions, and generalizing the Poiseuille equation, we recall the following expressions for the boundary-dependent flow rate q, in the presence of a slip length b, or an adsorbed layer of hydrodynamic thickness D:

$$q = \frac{\Delta p}{r_c}\left(1 + \frac{6b}{h_0}\right), \tag{3.4}$$

and

$$q = \frac{\Delta p}{r_c}\left(1 - \frac{2D}{h_0}\right)^3 . \tag{3.5}$$

The prefactor $\Delta p/r_c = w h_0^3 \Delta p/12\eta L$ is the flow rate for a simple boundary condition. The equations above show that the boundary conditions impact significantly the flow rate, provided the channel thickness is of the order – or small – compared to b or D.

Flow rate measurements are complementary to TIRFM flow imaging: while the latter reveals the details of the near-wall flow, the former accesses the global integrated flow profile. Available tools, as those described in section 2.2.2 allow to measure flow rates and pressures in microfluidic environments with respective resolutions of 10 nL/min and 0.1 mbar. Furthermore, an advantage of such experiment is that it has a time resolution higher than particle tracking velocimetry, allowing convenient dynamic measurement of the boundary conditions.

Let us now attempt to find experimental conditions to obtain measurable boundary effects. With the microfabrication techniques available to us we tar-

geted a channel thickness h_0 = 5 µm. We also assumed a fluid viscosity of typically 10 times that of water, and set the channel length to 4 cm, to stay in Hele-Shaw conditions. With this in mind, let us list the experimental constraints. For a measurable relative flow rate difference, the flow rates must remain in the recommended range of our sensor, that is between 70 nL/min and 1500 nL/min. To couple this measurement with TIRFM velocimetry, the near-wall shear rate should not exceed 1000 s^{-1}. Finally, the maximum accessible pressure drop was 2000 mbar. With these constraints, the ideal volume in the parameter phase space is limited, yet increasing the flow rate without changing the near-wall shear rate can be achieved by increasing the channel width. Another possibility would be to have multiple channels in parallel, but to keep the system as simple as possible we will here focus on simple channels. Using microchannels of dimensions h_0 = 5 µm, w = 1 mm, and L = 4 cm, the system meets the previously-mentioned requirements.

To quantitatively extract information on the boundary condition from flow rate measurement, the system must be well characterized. While Poieuille law has proven robust and reliable there is an effect often overlooked when working with soft elastomers as fabrication material: channel compliance. There is no such thing as infinitely rigid material. When submitted to a pressure difference, any solid deforms. The simplest framework to study channel deformation under pressure is the elasticity theory, and without going into details for now, let us compute some orders of magnitude for our situation. Introducing E_Y the Young's modulus – the material property that quantifies its elastic response – the typical deformation in the z direction for a microchannel under pressure Δp reads $\delta h \sim w\delta P/E_Y$ [7]. With w = 1000 µm, Δp = 100 mbar and $E_Y = 10^6$ Pa, we have δh = 10 µm. This deformation is large compared to the underformed channel height, hence we can expect important effects on the flow.

The important consequence of the above calculation is that rationalizing the flow rate within our microfluidic channels, constructed using PDMS elastomer requires proper investigation of the elasto-hydrodynamic coupling between the flow and the elastic response of the surrounding material. This problem is non-trivial, even for simple fluids, and will be the topic of the next chapter.

Conclusion of the chapter

TIRFM microscopy associated to PTV allowed to map the flow field of microfluidic flows, in a submicron-thick region close to the bottom glass wall of the channel. Two quantities of interest were extracted from these velocity profiles: the near-wall shear rate and the slip length. The former is connected to the rheological behavior of the fluid, while the latter quantified the hydrodynamic boundary condition.

Having characterized the setup with simple Newtonian fluids, polymer solutions were investigated. A series of measurements in PAM and HPAM solutions were performed at various concentrations and flow rate. We first measured the shear rate-dependent viscosity of our sample, which was in accordance with bulk rotational rheometry. Regarding the boundary conditions, our solutions displayed two types of behaviors. While neutral polymers display a molecular-sized adsorbed layer, negatively-charged polymers show apparent slip, which could be rationalized with a two-layer model. In this framework the slip scales like the correlation length, amplified by a factor $\eta/\eta_s - 1$, which can be large, explaining the long slip lengths measured here. This model also revealed the importance of the local rheology in slip at the wall, and makes our experimental setup particularly well suited. , for it accesses simultaneously the boundary condition and the rheological behavior of the flowing material.

The local phenomena discussed in this section may have a measurable impact on the flow throughput in thin channels. However, at these scales channel compliance cannot be neglected, setting the need for an elasto-hydrodynamic model to disentangle compliance effect from boundary conditions.

Chapter 4

Soft hydraulics and its dynamical aspects

When studying flows within a conduit, it is natural to assume that the geometry is fixed and known. This implicitly supposes that the surrounding walls are infinitely rigid. Yet in microfluidics, softness of the fabrication materials, slenderness of the channel geometries and high pressure gradients make conduits easy to deform. The resulting coupling between the flow and compliant boundaries is an example of elastohydrodynamic (EHD) interaction, a concept that is actually ubiquitous in soft matter physics.

EHD is key to many biological situations, including joint lubrication [146], eyelid wiper mechanics[147], transport in blood vessels [148, 149, 150, 151], or in plants xylem networks [152]. Compliance is also at stake in modern microfluidics, with applications in organs-on-a-chip [153, 154] and wearable technologies [155, 156]. More precisely, and to name a few examples, targeted actuation of deformable pipes allows to generate and manipulate flows at the scale of a single channel [157, 158, 159], or in complex network [160]; and pressure-controlled soft valves serve as building blocks for state-of-the-art microfluidic devices [161, 162, 163].

In our rectangular PDMS channels EDH coupling leads to two notable effects. The first one is the non-linearity of the pressure-*vs.*-flow rate relation [7, 8], breaking Hagen-Poiseuille law. The second effect is the existence of a finite relaxation time scale upon pressure change, arising from a volume-storage capacity [164], analogous to the well-known charge-storage capacity in electronics. While the former has been well described in the literature, the latter has received less attention so far.

In this chapter we use our microfluidic setup to monitor the time-dependent flow rate and pressure at chip inlet, when the pressure is suddenly decreased. After showing raw data in section 4.1, we analyze steady-state experiments in

part 4.2, confirming the reported order-4-polynomial relation between pressure and flow rate. We also provide an *in situ* measurement of the channel deformation by interferometry, and discuss the impact of EHD on TIRFM data analysis. Finally, in section 4.3 we study the transient regime, which shows a pressure-dependent relaxation time scale and build our own EHD model to rationalize the data.

The majority of the results presented in this chapter were published in *Physical Review Letters*, a work involving F. Restagno and J. D. McGraw [165].

4.1 Time-signal analysis

The experimental setup is recalled in figure 4.1 (a). In this study all the pressures are given relative to the atmospheric pressure. A pressure p_{in} is applied in a water reservoir, which drives the flow in a flow sensor, a pressure sensor, and a deformable PDMS chip. While a series of decreasing steps of constant amplitude $\delta p_{in} \ll p_{in}$ are applied in input, the flow rate $q(t)$ and the pressure at channel inlet $p_0(t)$ are recorded. This experiment was performed in the 20 µm-tick, 180 µm-wide and 8.8 cm-long channels used in the previous chapter, as well as in dedicated channels of 5 µm in thickness, 4 cm in length, and variable widths. The experiment was also performed without any channel, *i.e* with no output resistance, and with the circuit plugged after the pressure sensor, *i.e.* with infinite output resistance. As we will see, this allowed to characterize the sensors.

An example of typical signal is given in figure 4.2, for (a) no chip, and (b) a

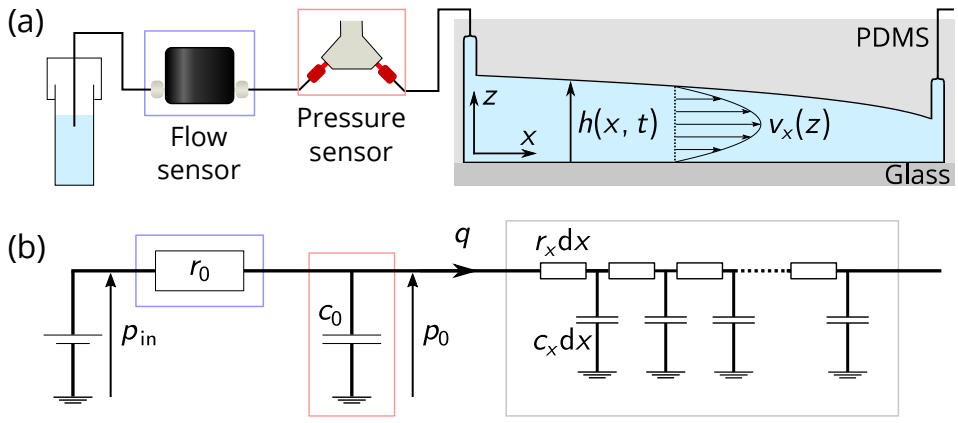

Figure 4.1: (a) Schematics of the microfluidic setup, involving a soft chip, a flow sensor and a pressure sensor located at channel inlet. (b) Equivalent electric circuit, where the flow sensor is an ideal resistance, the pressure sensor is a capacitance and the chip a transmission line.

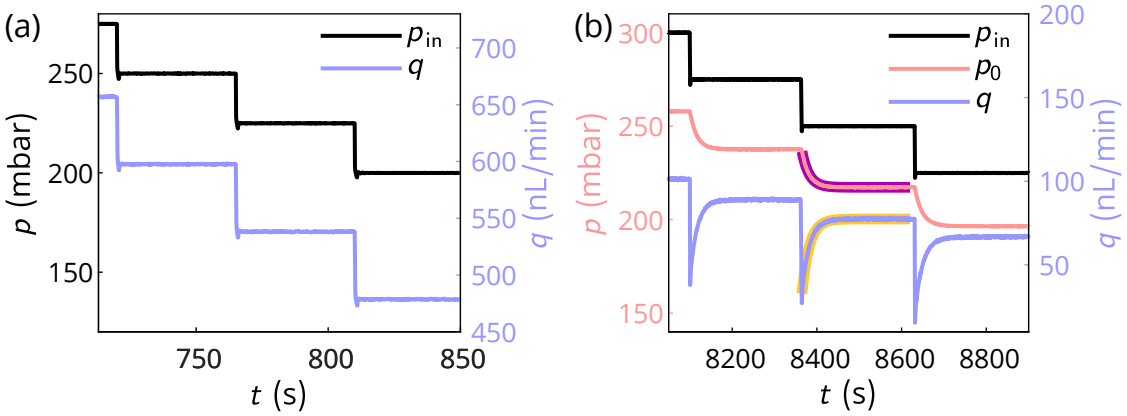

Figure 4.2: Selection temporal signals $p_{in}(t)$, $p_0(t)$, $q(t)$ recorded (a) with just a flow sensor and (b) with a $\{w, h_0, L\}$={200 µm, 5 µm, 4 cm} PDMS channel. Thicker lines show examples of exponential fits of the data.

5 µm-thick chip. With no channel connected, the response of the flow sensor alone is quasi-instantaneous, *i.e.* when the input pressure drops the flow rate drops with no measurable delay. Conversely with a chip plugged, and while p_{in} varies in typically 0.1 s, the system relaxes over a much longer time scale – of order 10 s. The relaxation is well fitted by an exponential decay, as exemplified in figure 4.2 (b), with a characteristic time τ_t that is the same for $q(t)$ and $p_0(t)$. After this transient regime, a steady state is reached, where the input pressure is denoted $p_{in,\infty}$, the flow rate q_∞ and the inlet pressure $p_{0,\infty}$.

4.2 Steady-state deformation analysis

4.2.1 Flow rate - pressure relation

Firstly we pay attention to the steady states. In figure 4.3 is shown the flow rate as a function of pressure for (a) the flow sensor only and (b) with a 20 µm-thick channel connected. The flow sensor shows a perfectly linear response, with an associated resistance $r_0 = 2.50 \pm 0.01$ kPa s/nL. This behavior is consistent with Poiseuille flow theory in a circular capillary of length L_0 and radius ρ_0, for which the predicted resistance is $r_0 = 8\eta L_0/\pi\rho_0^4$. Taking $\rho_0 = 12.5$ µm, as given by the manufacturer, we obtain $L_0 = 2.4$ cm, a length compatible with the size of the device. The resistance r_0 is of the same order of magnitude as that of the channels used in this study, therefore there is a finite pressure drop within the flow sensor, justifying the pressure measurement at chip inlet: $p_0 < p_{in}$.

The 20 µm-thick channel has a linear behavior for $p_{0,\infty}$ values up to approx-

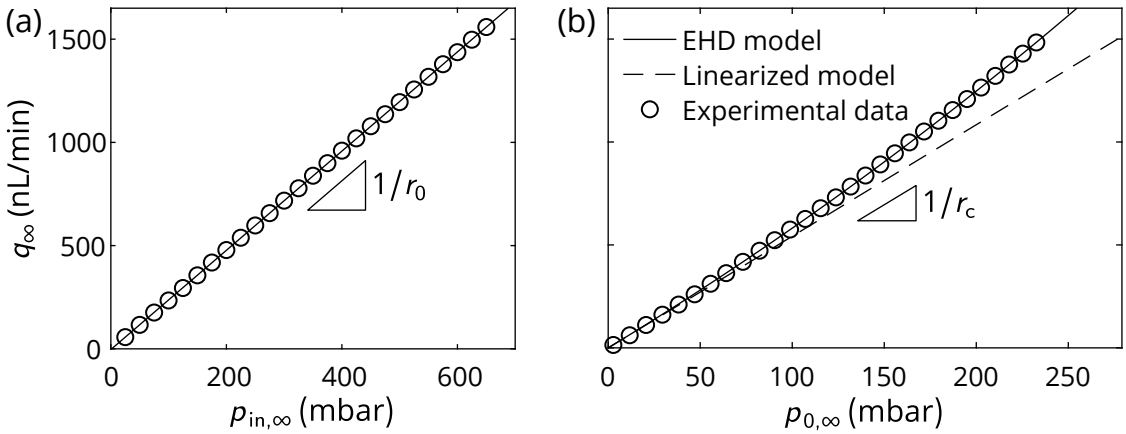

Figure 4.3: (a) Steady state flow rate as a function of input pressure for the flow sensor only, with the best fitting straight line. (b) Flow rate as a function a inlet pressure for a 20 µm-thick channel. The solid line is the best fit associated to equation 6.5, and the dashed line is the linearization of this model for low pressures.

imately 50 mbar, after what we observe a super-linear deviation. This observation can be rationalized in the context of EHD, by taking into account the deformation of the channel under pressure. Qualitatively, if a channel expends under pressure, its thickness increases and its resistance, proportional to h^{-3}, decreases. Said differently, when pushing harder in the channel, both the driving force increases and the friction decreases simultaneously, explaining the super-linearity of the flow-rate with respect to pressure.

We now provide a quantitative analysis of the problem. The flow is assumed to be Newtonian, incompressible, and at low Reynolds number. Since $h_0 \ll w \ll L$, – "≪" meaning at least 10 times smaller – we place ourselves in the one dimensional limit. Denote $h(x, t)$ the local height of the channel, and $p(x, t)$ the pressure field within. The Reynolds lubrication equation demonstrated in chapter 1 – see equation 1.13 –, expresses momentum and volume conservation in the thin channel:

$$\frac{\partial h}{\partial t} = \frac{1}{12\eta}\frac{\partial}{\partial x}\left(h^3\frac{\partial p}{\partial x}\right). \tag{4.1}$$

Additionally, we propose a local and linear response of the PDMS slab, assumed purely elastic of Young's modulus E_Y. We consider ourselves in the infinitely thick slab limit, an approximation shown to be valid as soon as the thickness of the slab is roughly twice the width of the channel [166], which was always the

case in practice. Using the framework described in [7, 167], we have:

$$h(x,t) = h_0 + w\frac{p(x,t)}{E^*}\,. \tag{4.2}$$

The modulus E^*, proportional to E_Y, contains the fine details of the specifically-applied elastic theory, [166]. Wang and Christov computed the following expression: $E^* = E_Y/0.5427(1-\nu_{PDMS}^2)$, where ν_{PDMS} is the Poisson's ratio of the material [167]. This expression ensures E^* is material- but not geometry-dependent.

Combining equations 4.1 and 4.2, we obtain the constitutive EHD equation for the pressure field within the channel:

$$\frac{\partial p}{\partial t} = \frac{E^* h_0^3}{12\eta w}\frac{\partial}{\partial x}\left[\left(1+\frac{pw}{E^* h_0}\right)^3\frac{\partial p}{\partial x}\right]. \tag{4.3}$$

With the latter equation comes the natural pressure scale $p^* = E^* h_0/w$ and time scale $\tau_c = 12\eta L^2/h_0^2 p^*$. Physically, p^* is the pressure required to deform the channel its own size, while τ_c is the time it takes to purge the channel, under a pressure drop p^*. We now make equation 6.4 dimensionless with the following scalings: $x = LX$, $p_k = p^* P_k$, where the subscript "k" may denote any pressure in the problem, and $t = \tau_c T$:

$$\frac{\partial P}{\partial T} = \frac{\partial}{\partial X}\left[(1+P)^3\frac{\partial P}{\partial X}\right]. \tag{4.4}$$

At steady state, this equation can be solved with the boundary condition $P(X=1) = 0$ and $P(X=0) = P_{0,\infty}$, which gives the steady pressure profile $P_\infty(X)$:

$$P_\infty(X) = \left[(1-X)\left((1+P_{0,\infty})^4 - 1\right) + 1\right]^{1/4} - 1\,. \tag{4.5}$$

We also note that from equation 4.2, this pressure profile is also , up to a prefactor, the height profile: $\Delta H = (h-h_0)/h_0 = P$. The steady-state flow rate q_∞ associated with such deformed profile is given by Poiseuille flow theory: $q_\infty = \left(w h(x)^3/12\eta\right)\mathrm{d}p/\mathrm{d}x$. In the latter expression, the x-dependence has to drop as a result of volume conservation. We obtain:

$$q_\infty = \frac{p^*}{4r_c}\left[\left(1+\frac{p_{0,\infty}}{p^*}\right)^4 - 1\right], \tag{4.6}$$

where $r_c = 12\eta L/w h_0^3$ is the hydraulic resistance of the undeformed channel. Defining the dimensionless flow rate $Q_\infty = q_\infty p^*/r_c$, and $\Pi = (1+P_{0,\infty})^4 - 1$, the flow rate *vs.* pressure relation simply reads $Q_\infty = \Pi/4$. We will see throughout this section and in the following one that Π is a relevant change of variable.

Equation 6.5 quantifies the super-linear behavior mentioned above. For small pressures with regard to p^*, we recover the linear relation $q_\infty = p_{0,\infty}/r_c$, otherwise the flow rate grows like an order-4 polynomial in $p_{0,\infty}$.

Let us now use equation 6.5 to fit the data of figure 4.3 (b). The model fits the data well with the two fitting parameters $p^* = 2120$ mbar and $r_c = 1.107$ kPa s/nL. A remarkable feature of r_c is its strong dependence in h_0, which makes the resistance measurement a precise way of measuring this quantity. To be even more accurate, we can use a higher order development of the hydraulic resistance for a rectangular channel [3]:

$$r_c = \frac{12\eta L}{w h_0^3}\left(\frac{1}{1 - 0.63 h_0/w}\right). \tag{4.7}$$

Solving the latter equation with $L = 8.8$ cm, $w = 180$ µm and $\eta = 1.00 \pm 0.05$ mPa s, we obtain $h_0 = 18.0 \pm 0.3$ µm, a value within experimental error of mechanical profilometry results, that predicted $h_0 = 18.1$. The relative error mentioned above mostly comes from the uncertainty on the water viscosity, that varies strongly with temperature [140] and which was not controlled in this experiment.

With $r_c \propto h_0^{-3}$ and $p^* \propto h_0$, equation 6.5 reveals that h_0 is crucial in this experiment, and motivated experiment with thinner channels. In figure 4.4 is plotted the flow rate as a function of inlet pressure, at steady state, for channels of 5 µm

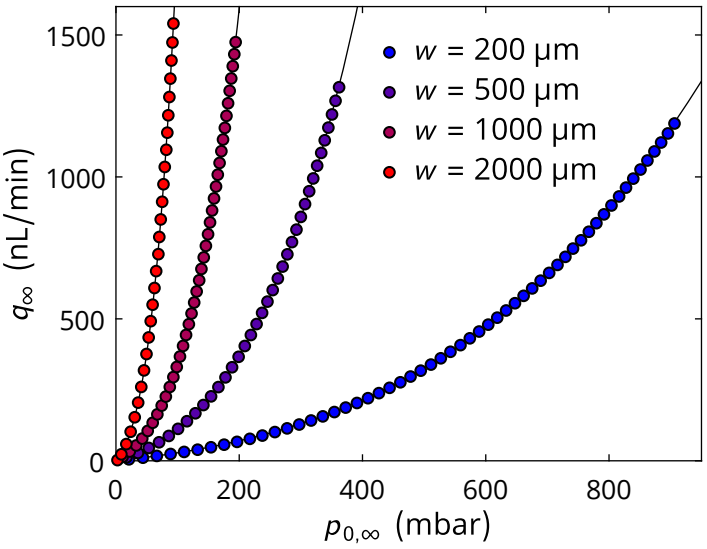

Figure 4.4: Steady state flow rate *vs.* pressure relation for 4 different microchannels of 5 µm in height, 4 cm in length, and different widths as indicated in the legend. The black lines represent the best fit according to equation 6.5.

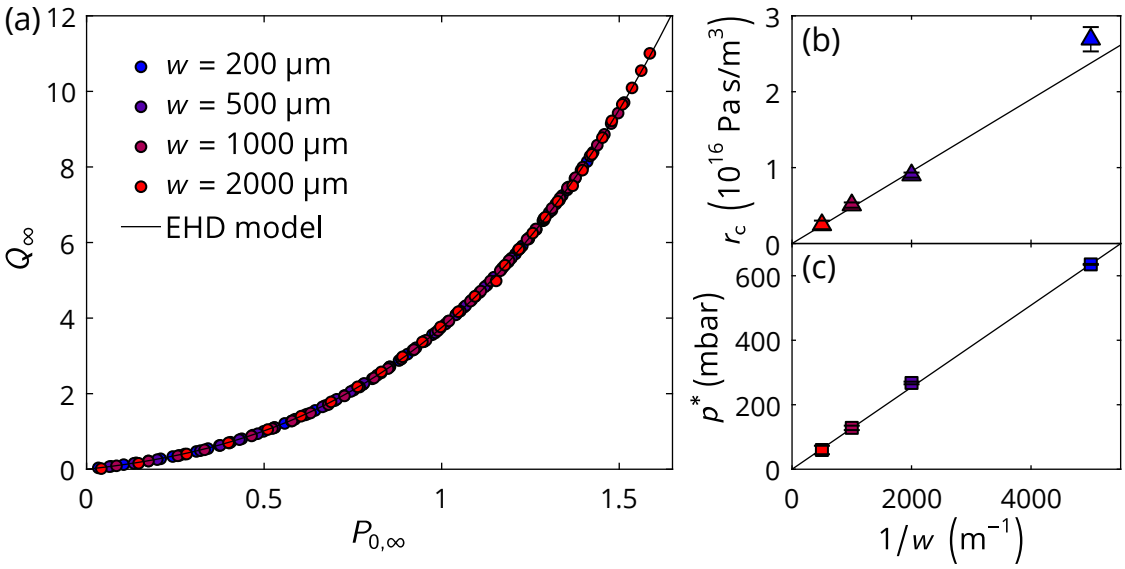

Figure 4.5: (a) Dimensionless steady state flow rate *vs.* pressure, for the same four microchannels as in figure 4.4. The black line is equation 6.5. (b) & (c)show the fitting parameters r_c and p^* plotted as a function of the inverted with of the channel. Black lines represent best linear fits of the data.

in thickness, 4 cm in length, and width varying between 200 and 2000 µm. All the data are well fitted by equation 6.5. Upon width increase, the non linear regime appears at lower pressure and the flow rate increases, consistent with deceasing p^* and r_c.

Associated normalized data can be seen in figure 4.5 (a). The data collapse well all along the accessible range of dimensionless pressures – *i.e.* up to 160% relative change in channel height. Fitting parameters r_c and p^* are plotted in (b) and (c), respectively. As expected, the two latter quantities scale linearly with $1/w$. The slope on graph (c) is a measurement of $h_0 E^*$. Since the chips come from the same wafer, and the same batch – exepted from the 2000-wide channel – the comparison is relevant. With $h_0 = 4.9 \pm 0.1$ µm, measured by profilometry, we obtain $E^* = 2.62 \pm 0.06$ MPa. With $\nu_{\text{PDMS}} = 0.5$, this corresponds to $E_Y = 1.07 \pm 0.03$ MPa, an order of magnitude that is expected for such elastomers [168].

4.2.2 Measurement of channel deformatioin by interferometry

So far, our data provided a validation of the elatsoydrodynamic model based on global – *i.e.* integrated – measurements. In other words, we did not measure

the channel deformation directly, but it's impact in the flow rate *vs.* pressure relation, which is the consequence of the deformation integrated along the entire length of the channel. To complement this analysis we now propose a local measurement of the deformation.

We used an interfermometry setup with visible light, well suited because all the material used here are transparent, and because we expect micrometric deformations. The setup is sketched in figure 4.6. A mercury lamp and a filter (545 ± 12 nm) were used to generate monochromtic light at the wavelength $\lambda = 546$ nm, that was guided with an optical fiber toward a collimator, and a microscope objective (Leica HC PL Fluotar, 20x, NA = 0.40), so that the sample was illuminated by a plane wave, in normal incidence. The objective also served for visualization and data were recorded with a grayscale camera (Pixellink). A small 1.6 mm-long portion of the chip, center around $x/L = 0.95$ was observed while inflated with a flow of air, controlled by the pressure controller. The experiment was performed in a channel of dimensions $\{w, h_0, L\} = \{500\ \mu m, 5\ \mu m, 4\ cm\}$.

Working in air, of index $n_{air} \approx 1.00$, rather that water ($n_w \approx 1.33$), provides better index mismatch with PDMS ($n_{PDMS} \approx 1.43$) and thus better contrast for the interference fringes, while not changing the deformation according to equation 4.5. With an air flow, the Reynold number increases up to 0.2 in this experiment, such that Poiseuille flow theory is still valid. Equation 4.5 also justifies working close to the outlet, where the deformation gradient is the largest.

As shown in figure 4.7 (a), one observes interference fringes, signature of uneven channel height within the field of view. The images displayed were processed with standard procedures, including background substraction, and noise filtering. When increasing the pressure drop across the chip, the number of

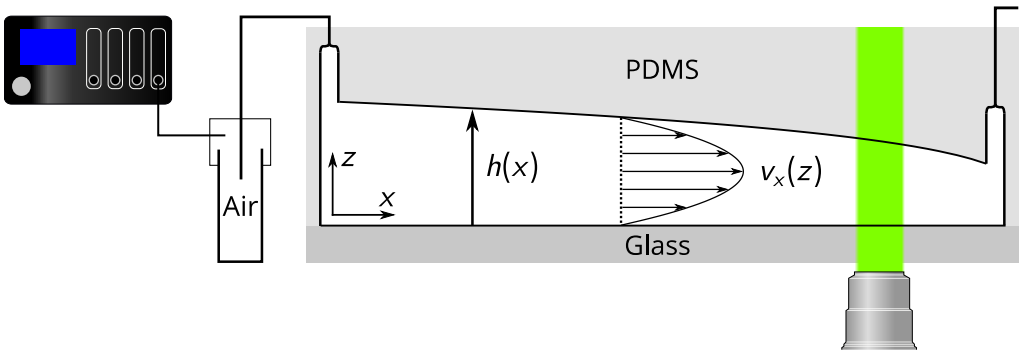

Figure 4.6: Schematics of the interferometry setup for channel height measurement. A pressure controller inflates the chip by blowing air within. A region close to the outlet is observed under a microscope while illuminated with monochromatic light.

fringes increases, meaning that the height changes quicker in space.

While the interference pattern reveals the deformation along y, we will focus on x-profile in this analysis. In figure 4.7 (a), the intensity profile along the central line of the channel is superimposed to the raw images. Such profiles are oscillating in space, with a characteristic wavelength. The intensity profile shown here were band-pass filtered around this wavelength, and the peaks were isolated. According to standard wave optics theory, the distance between two consecutive intensity maxima corresponds to a difference in height of $\lambda/2$ [169].

Since interferometry is based on phase difference for the illuminating light, we do not measure the absolute height, but the height difference Δh, with respect to an arbitrary reference. We also cannot distinguish a height increase from a height decrease, but the later would be nonphysical here. In figure 4.7 (b) we plot $-\Delta h$ as a function of the shifted coordinate Δx (the reference being taken on the left of the image), for two different input pressures. The data are well fitted by a straight line, allowing to extract a local slope $\partial h/\partial x$. At the scale of the observation zone, small compared to the full channel length, we observe a local linearization of the height profile.

This experiment was performed for many different input pressures, and the inverse normalized slope $-\partial H/\partial X = -(L/h_0)\,\partial h/\partial x$ is plotted as a function of the dimensionless pressure in figure 4.8. The normalizing pressure p^* was obtained by independantly fitting the pressure *vs.* flow rate curve as described in the previous section. The theory obtained by differentiating equation 4.5 is also

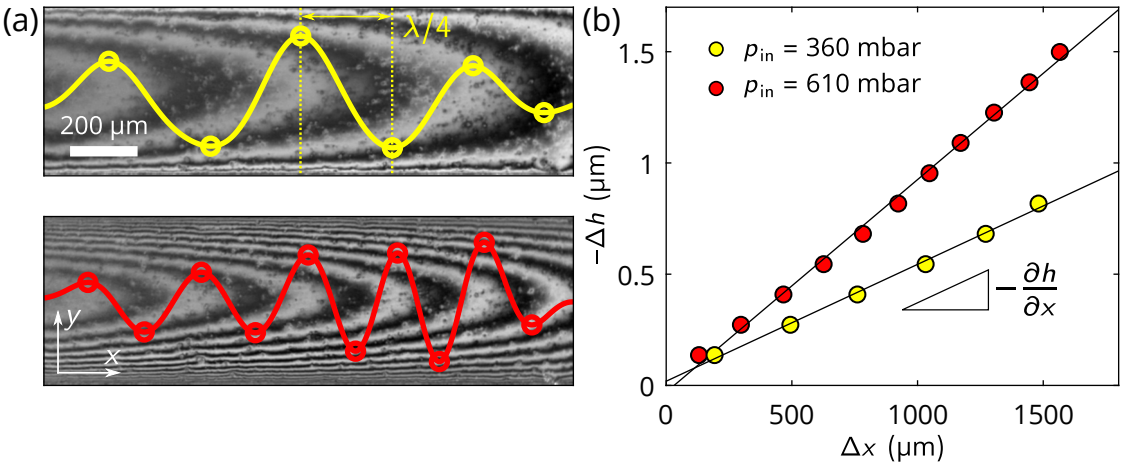

Figure 4.7: (a) Interference pattern observed on the camera, for two input pressures, (top) 360 mbar and (bottom) 610 mbar. The intensity profile, measured at the center of the channel, is superimposed. (b) Height difference as a function of x-coordinate, extracted for the two images of (a), with best fitting straight lines.

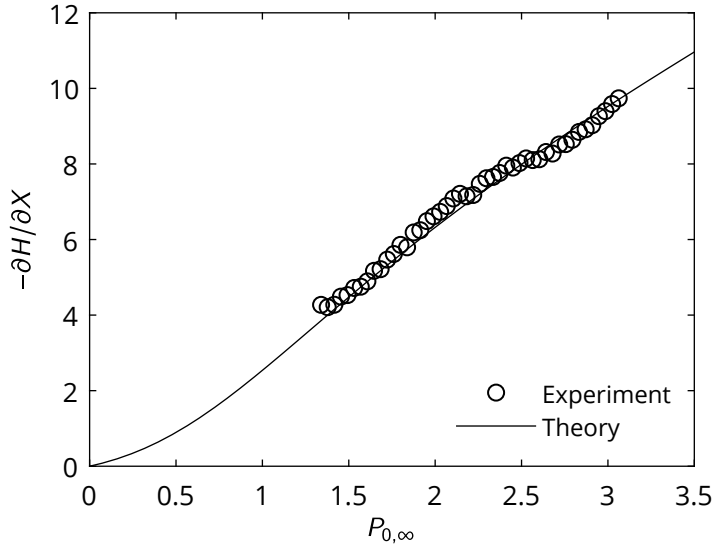

Figure 4.8: Dimensionless deformation gardient, taken close to the outlet, as a function of input pressure. The circles are the experimental data measured by interferometry and the solid line is the EHD theory (equation 4.8).

plotted for comparison. Namely, the theory predicts:

$$-\frac{\partial H}{\partial X} = \frac{1}{4}\left((1+P_{0,\infty})^4-1\right)\left((1-X)\left((1+P_{0,\infty})^4-1\right)+1\right)^{-3/4} . \tag{4.8}$$

The theory matches the experimental data quantitatively, with no adjustable parameter, providing a local validation of the EHD model for soft channel deformations.

4.2.3 Impact on TIRFM experiments

A natural question that arises from these results is the impact of channel deformation on TIRFM velocimetry experiment. TIRFM microscopy provides local measurements of the near-wall shear rate and hydrodynamic boundary condition at the bottom of the channel. While compliance is not expected to have a direct impact on these quantities, it is not without consequence on the local shear stress, used in viscosity evaluation. In section 4.2.1, we computed the nonlinear flow rate *vs.* pressure relation, we now do a similar analysis for the shear rate and the shear stress. We place ourselves at steady-state and the flow is assumed to be Newtonian and incompressible. The local Poiseuille law reads:

$$-\frac{\mathrm{d}p_\infty}{\mathrm{d}x} = \frac{12\eta}{h(x)^3 w} q_\infty , \tag{4.9}$$

where we recall that $p_\infty(x)$ is the pressure profile within the channel at steady state, and q_∞ is the constant flow rate. To compute the velocity profile, we use Stokes' equation:

$$\eta \frac{\partial^2 v_x}{\partial z^2} = \frac{\mathrm{d}p_\infty}{\mathrm{d}x} . \tag{4.10}$$

Combining equation 4.9 and 4.10, then integrating twice with respect to z, and using a zero-velocity at top and bottom walls, we have:

$$v_x(x,z) = \frac{6q_\infty}{h(x)^3 w}\left(h(x)z - z^2\right) . \tag{4.11}$$

This formula is a generalization of the parabolic Poiseuille profile, for channels of slowly varying profile $h(x)$. We now extract the shear rate near the bottom wall:

$$\dot\gamma = \left.\frac{\partial v_x}{\partial z}\right|_{z=0} = \frac{6q_\infty}{h(x)^2 w} . \tag{4.12}$$

Finally injecting the expressions of equations 4.5 and 6.5 for $h(x)$ and q_∞, we find the following relation for the near-wall shear rate as a function of pressure:

$$\frac{2L\eta\dot\gamma}{h_0 p^*} = \frac{1}{4}\left[\left(1+\frac{p_{\text{in}}}{p^*}\right)^4 - 1\right]\left[\left(1-\frac{x}{L}\right)\left(\left(1+\frac{p_{\text{in}}}{p^*}\right)^4 - 1\right) + 1\right]^{-1/2} . \tag{4.13}$$

Using $\sigma_{xz} = \eta\dot\gamma$, we can compute the shear stress at the wall, and its deviation from the rigid case $h_0 p_{\text{in}}/2L$:

$$\frac{2\sigma_{xz}L}{h_0 p_{\text{in}}} = \frac{1}{4}\frac{p^*}{p_{\text{in}}}\left[\left(1+\frac{p_{\text{in}}}{p^*}\right)^4 - 1\right]\left[\left(1-\frac{x}{L}\right)\left(\left(1+\frac{p_{\text{in}}}{p^*}\right)^4 - 1\right) + 1\right]^{-1/2} . \tag{4.14}$$

Figure 4.9 (a) displays this theoretical normalized shear rate $2\eta\dot\gamma L/h_0 p^*$ as a function of the dimensionless pressure, for different positions x/L along the channel. For $p_{\text{in}} \ll p^*$, the deformation is negligible and the curves collapse on the $y = x$ line. When p_{in} is no longer small compared to p^*, the local shear rate becomes x-dependent, and deviates from the rigid case, especially close to the outlet. The shear-rate growing faster with respect to pressure than in the rigid case, the effect of channel deformation could be mistinterpreted as shear thinning. To take into account channel compliance in TIRFM velocimetry experiments, let us now pay attention to the near-wall shear stress.

The shear stress also becomes pressure- and position-dependent when the channel deforms. Figure 4.9 (b) shows the compliant shear stress at the wall normalized by its rigid counterpart, as a function of the dimensionless pressure. In

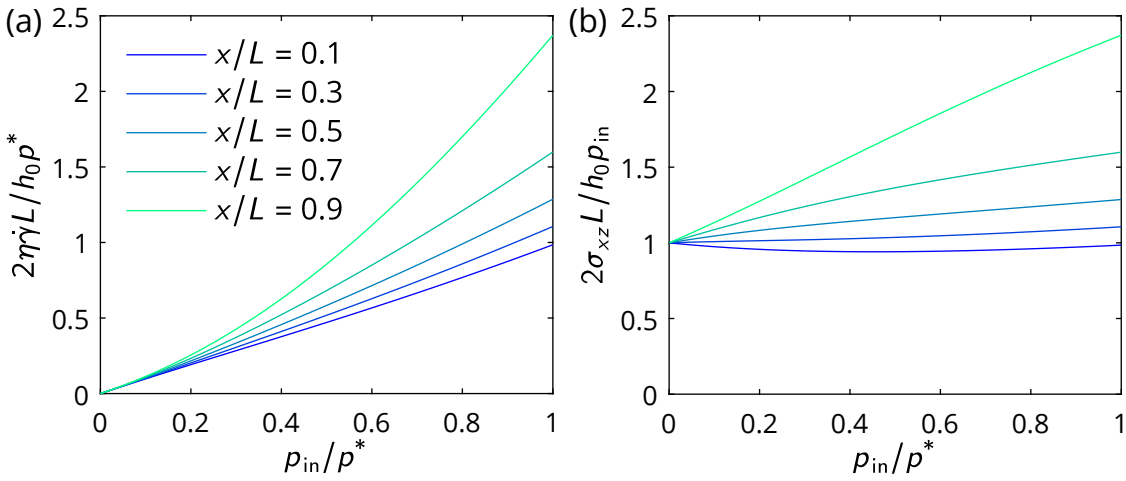

Figure 4.9: (a) dimensionless shear rate as a function of the dimensionless pressure in the case of a soft deformable chip, and computed for different positions along the channel. (b) Shear rate in the deformable case normalized the shear rate in the rigid limit, as a function of the dimensionless pressure. These two graphs refer to equation 4.13 and 4.14, respectively.

the TIRFM experiment, the largest pressure used, for viscous polymer solutions, corresponded to $p_{in}/p^* \approx 0.35$. According to the last graph this indicates a deviation of typically 15% in shear stress – and thus viscosity – evaluation. However performing the same experiment in more compliant channels, like the 5 µm-thick channels used in this chapter, this effect may become significant. In the annex at the end of this chapter, we show how taking into account compliance affects the results of figures 3.5 and 3.8 of chapter 3.

The EHD model discussed here, arises from two ingredients: the lubrication equation and the elasticity of the channel. It describes quantitatively the non-linearity of experimentally measured the flow rate *vs.* pressure data, as well as the local deformation observed by interferometry. We also showed that compliance may bias the estimate of the local shear stress, with possible impact on TIRFM velocimetry data. Having described the system at steady state, we now move on to the study of the transient regime.

4.3 Transient regime analysis

Upon a pressure drop, the system relaxes exponentially to a new steady state, with a characteristic time τ_t which we now focus on. The time τ_t is not constant across the pressure cascade. In figure 4.10 is plotted the inlet pressure $p_0(t)$, shifted by its steady state plateau value $p_{0,\infty}$ as a function of time. The straight lines in semi logarithmic axis indicate a purely exponential decay, and the various slopes show that τ_t decreases with $p_{0,\infty}$. More precisely, τ_t is plotted as a function of $p_{0,\infty}$ in figure 4.10(b). Rationalizing this systematic pressure-dependence of τ_t is the objective of this section.

4.3.1 Pushing the microfluidics-electronics analogy

Throughout this section, we will use the analogy between microfluidics and electronics, which, we think, facilitates the understanding of the systems [4, 5]. However all the equations written here rely on hydrodynamic laws. In this framework, the pressure is analogous to the voltage, the fluid volume to the electric charge, and the flow rate to the current. One reason why the analogy holds is that volume and charge, or their respective fluxes, obey the same conservation laws.

The exponential relaxations of figure 4.10 recall the transient regime of an RC circuit. With Poiseuille law, we have seen the microfluidic equivalent of a re-

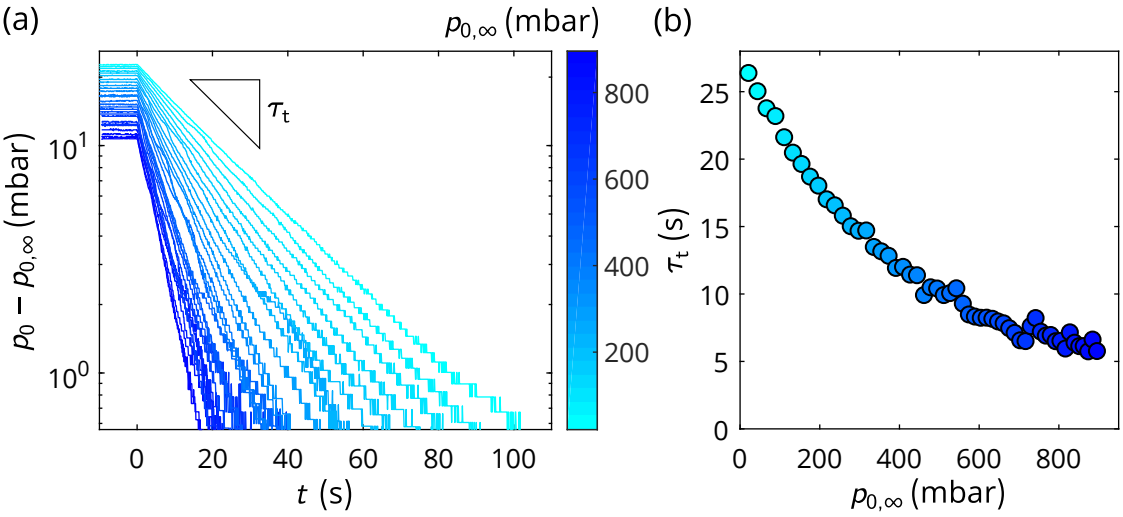

Figure 4.10: (a) Shifted pressure $p_0(t) - p_{0,\infty}$ as a function of time, for the relaxation toward different steady-states. (b) Associated relaxation times, measured by exponential fits of the data, as a function of steady-state pressure.

sistance. Introducing deformable parts, capacitance behavior arise. In electronics, a capacitance store charges upon voltage increase. Similarly, a microfluidic objects that swells upon pressure increase can store some extra fluid volume within. More precisely, we can define the microfluidic capacity by the volume stored per unit pressure. Therefore, compliant channels feature both ingredients to make a fluidic RC circuit. Yet the complete description of these objects required more sophistication, and a more appropriate model is the transmission line, depicted in figure 4.1 (b). The latter consists of a series of infinitesimal RC circuits. In electronics, the latter model gives a propagation equation for the voltage $V(x, t)$, known as the telegrapher's equation. Denoting r_x and c_x the resistance and capacitance per unit length in the latter model, we have:

$$\frac{\partial V}{\partial t} = \frac{1}{c_x}\frac{\partial}{\partial x}\left[\frac{1}{r_x}\frac{\partial V}{\partial x}\right]. \tag{4.15}$$

Taking a constant $c_x = w^2/E^*$ and a pressure-dependent $r_x = r_c\left(1 + p/p^*\right)^{-3}/L$, we recover equation 6.4 for the pressure field within the chip.

In addition to the microfluidic chip, the setup is composed of pressure and flow sensors, which are not passive. We may now wonder the analogous of these devices. The data of figures 4.2 (a) and 4.3 (a) suggest that the flow sensor is an ideal resistance, with quasi-instantaneous response and linear flow rate *vs.* pressure relation. On the other hand the pressure sensor works with a deformable membrane, suggesting it could have a capacitance behavior. To investigate its response, the pressure sweep experiment was performed with the circuit plugged after the pressure sensor, as depicted in figure 4.11 (a).

The experimental relaxation time for this experiment is plotted as a function of the steady state pressure in figure 4.11 (c). We observe a finite relaxation time, confirming the presence of a capacity in the system, that can only be caused by the pressure sensor since there is no channel here. Surprisingly, the relaxation time decreases with $p_{0,\infty}$. With just the flow sensor and the pressure sensor, the setup is analogous to an open RC circuit, as sketched in (b) and for which the relaxation time is $r_0 c_0$. Since r_0 is constant, the data suggests that the pressure sensor is a non-linear capacitance.

We rationalize this observation by assuming that the capacity c_0 results from two components: a constant capacity describing the mechanical deflection of the internal membrane, and a non-linear part due to an air bubble trapped in the internal volume of the sensor. Denote Ω_0 such volume of air under atmospheric pressure, p_{atm}. In the ideal gas limit, its volume Ω under pressure $p_{\text{atm}} + p_{0,\infty}$ reads $\Omega = \Omega_0/(1 + p_{0,\infty}/p_{\text{atm}})$. By definition the capacity of this object is $\mathrm{d}\Omega/\mathrm{d}p_{0,\infty} = \Omega_0/p_{\text{atm}}(1 + p_{0,\infty}/p_{\text{atm}})^2$. Finally we model the capacity of the sensor

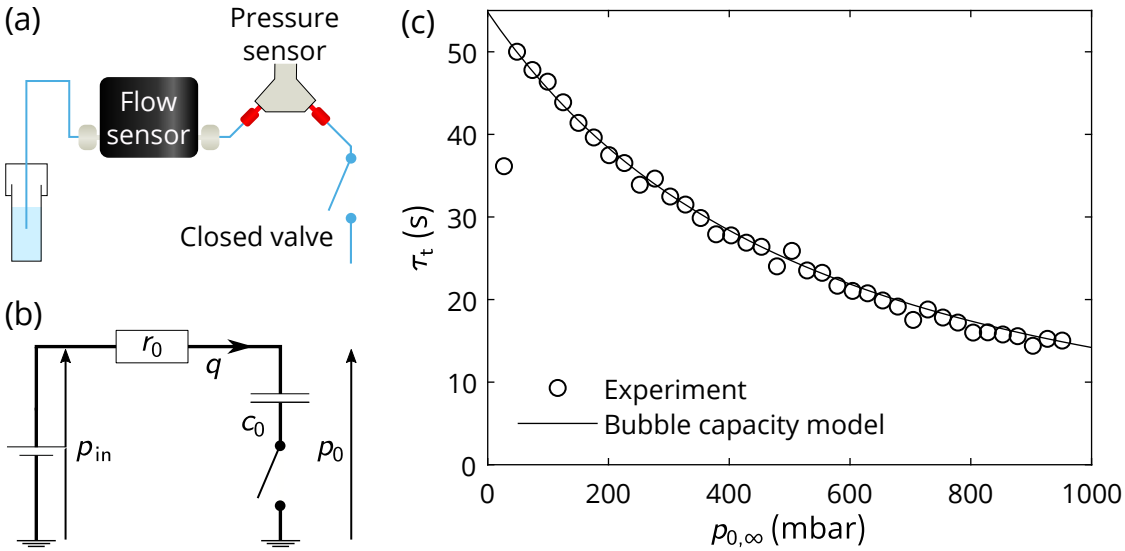

Figure 4.11: (a) Schematics of the plugged experiment and (b) equivalent electric circuit. (c) Relaxation time as a function of pressure for the depicted experiment. The black circles represent the experimental data point, and the solid line the best fitting line for the model described by equation 4.16, with fitting parameters c_1 and c_2.

by the following expression:

$$c_0 = c_1\left(1 + \frac{p_{0,\infty}}{p_{atm}}\right)^{-2} + c_2\,, \tag{4.16}$$

where $c_1 = \Omega_0/p_{atm}$ and c_2 are fitting parameters. With $\tau_t = r_0 c_0$, this model describes the data well for $c_1 = 20.9 \pm 0.1$ nL/kPa and, $c_2 = 0.2 \pm 0.1$ nL/kPa as can be seen in figure 4.11. The value of c_1 corresponds to a resting gas volume of 2.1 µL, which compares reasonably the the internal volume of the sensor, 7.5 µL according to the manufacturer.

We now have a full description of our microfluidic setup, as sketched in figure 4.1 (b). The flow sensor is an ideal resistance r_0, the pressure sensor is a pressure-dependent capacitance c_0 and the soft channel is a nonlinear transmission line. With that in mind we move on to the computation of the theoretical relaxation time τ_t.

4.3.2 Theoretical model for the relaxation time

To solve the dynamical part of this problem, we benefit from the small pressure drop amplitude δp_{in} to linearize equation 4.4. We introduce $\delta P(X,T) = P(X,T) -$

$P_\infty(X)$, where $P_\infty(X)$ is defined in equation 4.5. At order 1 in δP, equation 4.4 becomes:

$$\frac{\partial}{\partial T}\delta P = \frac{\partial^2}{\partial X^2}\left[(1+P_\infty(X))^3\,\delta P\right]. \tag{4.17}$$

We do the change of variable $\tilde{X} = (1-X)\Pi + 1$, where Π was introduced above as $\Pi = (1+P_{0,\infty})^4 - 1$, and $\tilde{T} = \Pi^2 T$. The new boundary for $\tilde{X}$ are $1+\Pi$ and 1 and the latter equation becomes:

$$\frac{\partial}{\partial \tilde{T}}\delta P = \frac{\partial^2}{\partial \tilde{X}^2}\left[\tilde{X}^{3/4}\delta P\right]. \tag{4.18}$$

We look for a separable solution of the form $\delta P(\tilde{X},\tilde{T}) = A(\tilde{X})B(\tilde{T})$. Injecting this *ansatz* in equation 4.18, we obtain the following relation:

$$\frac{B'_\zeta}{B_\zeta} = \frac{\left[\tilde{X}^{3/4}A_\zeta\right]''}{A_\zeta} = -\zeta\,, \tag{4.19}$$

where we have introduced the unknown constant eigenvalue ζ. The subscripts ζ in A and B recalls their ζ-dependence, and prime symbol means the derivative with respect to the natural variable. The left-hand side of the former equation gives:

$$B_\zeta(\tilde{T}) = \exp(-\zeta\tilde{T})\,, \tag{4.20}$$

where the integration constant is absorbed in A_ζ. This last equation predicts that the relaxation of the system is exponential, as seen in the experiments. To access τ_t, we need to find the allowed values for ζ. Differentiating twice the right-hand side of equation 4.19, we obtain:

$$0 = \left(\zeta\tilde{X}^{5/4} - \frac{3}{16}\right)A_\zeta + \frac{3}{2}\tilde{X}A'_\zeta + \tilde{X}^2 A''_\zeta\,. \tag{4.21}$$

This equation has an analytic solution, that involves Bessel functions. Using the boundary condition $\delta P(X=1,T) = 0$ – *i.e.* $A(\tilde{X}=1) = 0$, we have:

$$A_\zeta(\tilde{X}) = \alpha_\zeta \tilde{X}^{-1/4}\mathcal{C}_{4/5}(\tilde{\chi})\,, \tag{4.22}$$

where $\tilde{\chi} = 8\sqrt{\zeta}\tilde{X}^{5/8}/5$ and $\mathcal{C}_\gamma(\tilde{\chi}) = Y_{4/5}\left(8\sqrt{\zeta}/5\right)J_\gamma(\tilde{\chi}) - J_{4/5}\left(8\sqrt{\zeta}/5\right)Y_\gamma(\tilde{\chi})$ is a linear combination of Bessel functions J_γ and Y_γ, and α_ζ is an integration constant.

To close the problem we need the boundary condition at $X = 1$, or $\tilde{X} = 1+\Pi$. By analogy with electronics, we write the following equation, equivalent to volume conservation at channel inlet:

$$\frac{p_{\text{in}} - p_0}{r_0} - c_0\frac{\mathrm{d}p_0}{\mathrm{d}t} = \left(-\frac{wh^3}{12\eta}\frac{\partial p}{\partial x}\right)\Bigg|_{x=0}. \tag{4.23}$$

We introduce the dimensionless parameters $\mathcal{T} = r_0 c_0/\tau_c$ and $\mathcal{R} = r_0/r_c$, and we non-dimensionalize the former equation:

$$P_{in} - P_0 - \mathcal{T}\frac{dP_0}{dT} = -\mathcal{R}\left[(1+P)^3\frac{\partial P}{\partial X}\right]\Bigg|_{X=0} . \tag{4.24}$$

We proceed similarly to the EHD constitutive equation, starting by linearizing at order 1 in δP. We also use pressure continuity, namely $P(X=0,T) = P_0(T)$:

$$\left[-\delta P - \mathcal{T}\frac{\partial \delta P}{\partial T}\right]\Bigg|_{X=0} = -\mathcal{R}\left[\frac{\partial}{\partial X}\left((1+P_\infty)^3\delta P\right)\right]\Bigg|_{X=0} . \tag{4.25}$$

Doing the change of variable from (X,T) to $(\tilde{X},\tilde{T})$ we obtain:

$$\left[\delta P + \Pi^2\mathcal{T}\frac{\partial \delta P}{\partial \tilde{T}}\right]\Bigg|_{\tilde{X}=1+\Pi} = \left[-\mathcal{R}\Pi\frac{\partial}{\partial \tilde{X}}\left[\tilde{X}^{3/4}\delta P\right]\right]\Bigg|_{\tilde{X}=1+\Pi} . \tag{4.26}$$

We now inject the separable *ansatz* arising from equations 4.20 and 4.22, that reads $\delta P(\tilde{X},\tilde{T}) = \alpha_\zeta \tilde{X}^{-1/4}\mathcal{C}_{4/5}(\tilde{\chi})\exp\left(-\zeta\tilde{T}\right)$, and we use tabulated formula for the derivative of Bessel functions that can be found in [170]. We obtain:

$$\left[\mathcal{C}_{4/5}(\tilde{\chi}) - \Pi^2\mathcal{T}\zeta\mathcal{C}_{4/5}(\tilde{\chi})\right]\Big|_{\tilde{X}=1+\Pi} = \left[-\mathcal{R}\Pi\sqrt{\zeta}\tilde{X}^{3/8}\mathcal{C}_{-1/5}(\tilde{\chi})\right]\Big|_{\tilde{X}=1+\Pi} . \tag{4.27}$$

Introducing $\tilde{X}_0 = 1+\Pi$, and finally evaluating this equation at $\tilde{X} = \tilde{X}_0$, we obtain:

$$\frac{1}{\mathcal{R}(1+\Pi)^{3/8}}\left(\mathcal{T}\Pi\sqrt{\zeta} - \frac{1}{\Pi\sqrt{\zeta}}\right) = \mathcal{C}_{-1/5}\left(\frac{8\sqrt{\zeta}}{5}\tilde{X}_0^{\,5/8}\right)\Big/\,\mathcal{C}_{4/5}\left(\frac{8\sqrt{\zeta}}{5}\tilde{X}_0^{\,5/8}\right) . \tag{4.28}$$

This equation provides a condition on the allowed values for ζ. According to equation 4.20, allowed relaxation times are of the form $\tau_c/\zeta\Pi^2$. Since we experimentally observed the longest allowed relaxation, we must look for the smallest allowed value of ζ, denoted ζ_s, and we have:

$$\tau_t = \frac{\tau_c}{\Pi^2\zeta_s(\Pi,\mathcal{R},\mathcal{T})} . \tag{4.29}$$

This equation shows that the τ_t depends on the pressure through Π, but also on the dimensionless numbers $\mathcal{R}$ and $\mathcal{T}$, which involve not only the chip but the peripheral sensors.

To the best of our knowledge, equation 4.28 does not have an analytic solution, yet we can solve it numerically. Example of such solving is provided in figure 4.12 for two different values of Π. The asymptotic behaviors for small or large Π can also be derived, using asymptotic development of Bessel functions.

While the details of the calculation are provided in an annex at the end of this chapter, we now give the main results.

First, we turn our attention to the low pressure behavior. For small Π – *i.e.* small $P_{0,\infty}$ – we have in particular $P_{0,\infty} \ll p^*$, such that the channel does not deform significantly, and behaves like an ideal resistance. This simplifies the problem, and by analogy with an electronic RC circuit, we do not expect a pressure-dependent relaxation time. According to equation 4.29, this suggests that $\zeta_s = \beta^2 \Pi^{-2}$ when $\Pi \to 0$, where β is independent of Π. This scaling was verified to be compatible with equation 4.28, in the low-Π limit, and, injecting this power law, we have the following condition for β: $\mathcal{T}\beta^2 - \mathcal{R}\beta/\tan(\beta) - 1$. The latter equation does not solve simply, but always has solution in $[0,\pi]$.

We now move on to the large-Π regime. As the pressure increases, the resistance of the channel decreases as a result of the change in height, until it eventually becomes negligible compared to r_0. By analogy with the RC circuit, the relaxation time should be proportional to the smallest resistance of the system, leading to a scaling of the form $\tau_t \propto h^{-3} \propto p_{0,\infty}^{-3}$. Again according to equation 4.29, this suggests for a scaling of the form $\zeta_s = \beta^2 \Pi^{-5/4}$, a scaling shown to be compatible with equation 4.28 in the large Π limit. Injecting the scaling in the latter equation provides the following condition for β: $\frac{\mathcal{T}}{\mathcal{R}}\beta = \mathrm{J}_{-1/5}\left(\frac{8\beta}{5}\right)/\mathrm{J}_{4/5}\left(\frac{8\beta}{5}\right)$. A

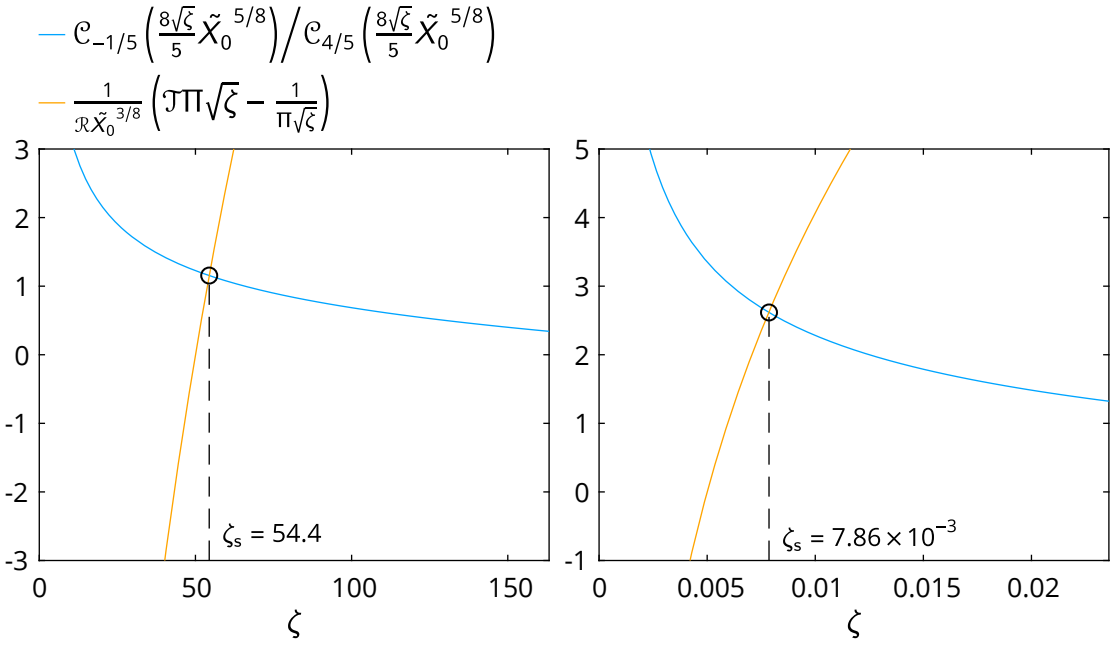

Figure 4.12: Numerical resolution of equation 4.28, for (a) $\{\Pi,\mathcal{T},\mathcal{R}\} = \{0,1,2,0,1\}$ and (b) $\{\Pi,\mathcal{T},\mathcal{R}\} = \{10,2,0,1\}$

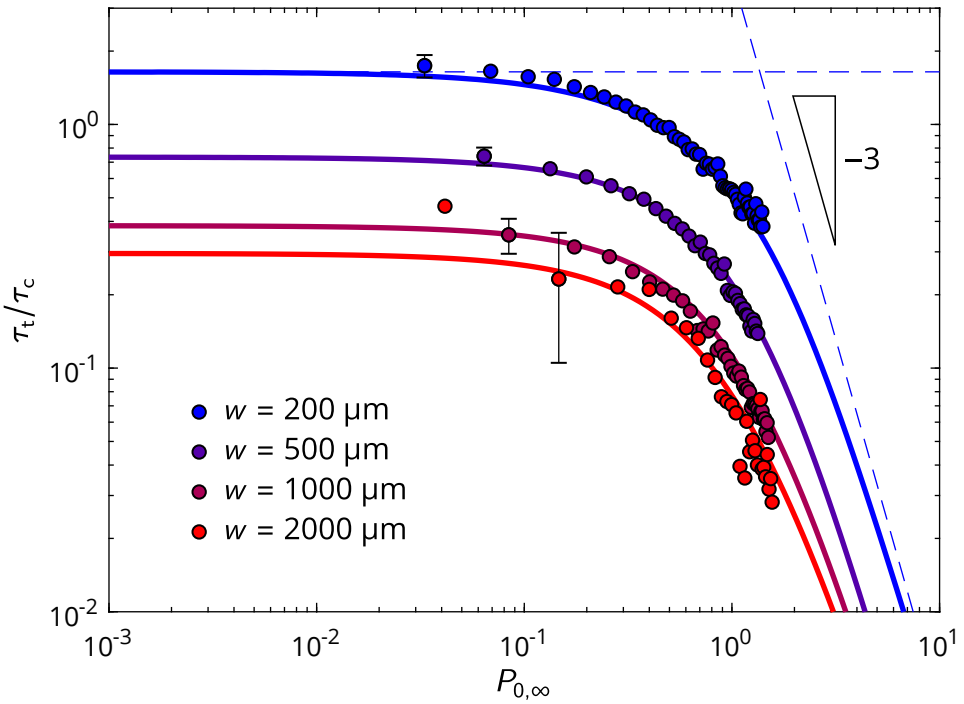

Figure 4.13: Normalized relaxation time scale, as a function of the dimensionless pressure for four chips of different widths. The circles are the experimental results, with one typical error bar displayed for each curve. The solid lines indicate the numerical resolution of the model described in section 4.3.2, the dashed lines are the asymptotic developments of this model, for the 200 µm-wide channel.

simple analysis of the function $z \to \mathrm{J}_{-1/5}(z)/\mathrm{J}_{4/5}(z)$ demonstrates that this equation always has a real solution. To sum up, we have the following asymptotic behaviors:

$$\text{for } \Pi \ll 1 \quad : \quad \frac{\tau_t}{\tau_c} = \frac{1}{\beta^2} \quad \text{with} \quad \mathcal{T}\beta^2 - \mathcal{R}\beta/\tan(\beta) - 1\,, \tag{4.30}$$

$$\text{for } \Pi \gg 1 \quad : \quad \frac{\tau_t}{\tau_c} = \frac{1}{\beta^2 P_{0,\infty}^3} \quad \text{with} \quad \frac{\mathcal{T}}{\mathcal{R}}\beta = \frac{\mathrm{J}_{-1/5}\left(\frac{8\beta}{5}\right)}{\mathrm{J}_{4/5}\left(\frac{8\beta}{5}\right)}\,. \tag{4.31}$$

Note that $\mathcal{T}$ is pressure dependent in the bubble capacity model described earlier. Thus in the two latter equation, $\mathcal{T}$ must be taken to its low- and large-$P_{0,\infty}$ limit, which are both finite according to equation 4.16.

In figure 4.15 is plotted the normalized relaxation time scale τ_t/τ_c as a function of the dimensionless pressure $P_{0,\infty}$ for the four 5 µm-thick channels. The model described in this section is superimposed in thick lines, and its asymp-

totic development in dashed lines. The model describes the data well, for all the channels and across mode than one order of magnitude in $P_{0,\infty}$. The only fitting parameters were $c_1 = 8.6 \pm 0.4$ nL/kPa and $c_2 = 2.1 \pm 0.2$ nL/kPa from equation 4.16, describing the inlet capacity. As discussed before c_1 is the volume of trapped air at atmospheric pressure – here 0.86 µL, we can also provide a physical picture for c_2. The channel design features a circle or radius R_{in} at inlet and outlet to allow easy tubing connection. Such patterns also have an volume-storage capacity, estimated to be $R_{\text{in}}^3/E^* \approx 1$ nL/kPa, a value close the experimental evaluation of c_1.

Conclusion of the chapter

In this chapter we have characterized and modeled the flow of simple fluids in soft deformable channels. First, the non-linearity of the flow rate *vs.* pressure relation at steady-state was measured to be an order-4 polynomial. This behavior is in accordance with the framework available in the literature, that couples lubrication theory and linear elasticity. We associated these data with a local interferometry measurment of the channel height, that confirmed the expected scalings for the top wall deformation.

Then extending this framework to dynamical experiments, and taking into account the effects of the peripheral microfluidic equipment, we were able to rationalize the pressure-dependent relaxation time of the system upon pressure change. This work, demonstrates that great care should be taken when doing microfluidic experiments with soft elastomers, and provides a simple criterion to assess whether EHD is at play, that is when $p/p^* \gtrsim 1$. Altough performed at the scale of a single channel, this study paths the way toward more complex soft networks, with potential in biology and microtechnologies.

This analysis is also complementary to TIRFM velocimetry experiments, for it provides integrated information on the flow, where microscopy reveals its local properties. However unlike TIRFM, the experiments described throughout this chapter are not easily applicable to complex fluids, essentially because the microfluidic sensors do not operate with fluids that are not water. Bypassing this limit is a challenge which we attempt to overcome in the next chapter.

Annex 1: Asymptotic relaxation time calculation

In this section we provide details on the calculation leading to equations 4.30 and 4.31.

Low pressure analysis

We start with the low-Π analysis. We gave a physical intuition justifying the attempt of a behavior of the form $\zeta_s \sim \beta^2 \Pi^{-2}$, which we now demonstrate. Assuming such a scaling, the left-hand side of equation 4.28 reads:

$$\frac{1}{\mathcal{R}\tilde{X_0}^{3/8}}\left(\mathcal{T}\sqrt{\zeta}\Pi - \frac{1}{\sqrt{\zeta}\Pi}\right) \sim \frac{1}{\mathcal{R}}\left(\mathcal{T}\beta - \frac{1}{\beta}\right). \tag{4.32}$$

For the right-hand side, let us first note that the argument inside the Bessel functions $\frac{8}{5}\sqrt{\zeta}\tilde{X_0}^{5/8}$ goes to infinity when Π goes to zero such that we can use the asymptotic developments of Bessel functions at infinity. Namely, for any complex number z: $J_\nu(z) \sim \sqrt{\frac{2}{\pi z}}\cos\left(z - \frac{\nu\pi}{2} - \frac{\pi}{4}\right)$ and $Y_\nu(z) \sim \sqrt{\frac{2}{\pi z}}\sin\left(z - \frac{\nu\pi}{2} - \frac{\pi}{4}\right)$. Using these formulas, the definition of $\mathcal{C}_\nu$, and basic trigonometric sum identities, we find:

$$\mathcal{C}_\nu\left(\frac{8\sqrt{\zeta}}{5}\tilde{X_0}^{5/8}\right) \approx \frac{5}{4\pi\sqrt{\zeta}}\tilde{X_0}^{-5/16}\sin\left(\frac{8}{5}\sqrt{\zeta}\left(4 - \tilde{X_0}^{5/8}\right) + \frac{5\nu - 4}{10}\pi\right).$$

Thus we have:

$$\frac{\mathcal{C}_{-1/5}\left(\frac{8\sqrt{\zeta}}{5}\tilde{X_0}^{5/8}\right)}{\mathcal{C}_{4/5}\left(\frac{8\sqrt{\zeta}}{5}\tilde{X_0}^{5/8}\right)} \approx \frac{\sin\left(\frac{8}{5}\sqrt{\zeta}\left(1 - \tilde{X_0}^{5/8}\right) - \frac{\pi}{2}\right)}{\sin\left(\frac{8}{5}\sqrt{\zeta}\left(1 - \tilde{X_0}^{5/8}\right)\right)} \approx -\mathrm{cotan}\left(\frac{8}{5}\sqrt{\zeta}\left(1 - \tilde{X_0}^{5/8}\right)\right). \tag{4.33}$$

Developing the argument inside the cotan function, we have $\frac{8}{5}\sqrt{\zeta}\left(1 - \tilde{X_0}^{5/8}\right) \approx -\beta$. Finally combining equations. 4.28, 4.32 and 4.33, and by using the unicity of the limit we obtain:

$$\frac{1}{\mathcal{R}}\left(\mathcal{T}\beta - \frac{1}{\beta}\right) = \mathrm{cotan}\left(\beta\right), \tag{4.34}$$

which can be written as follow:

$$\mathcal{T}\beta^2 - \mathcal{R}\beta\mathrm{cotan}(\beta) - 1 = 0. \tag{4.35}$$

This equation always has a positive solution for $\beta \in [0, \pi]$, provided $\mathcal{R} > 0$. This justifies the postulated scaling $\zeta_s \propto \Pi^{-2}$ and we have $\tau_t = \tau_c/\beta^2$ for low pressures.

High pressure analysis

We now turn our attention to the large-Π case, and proceed similarly. This time we assume a power law behavior of the form $\zeta_s \approx \beta^2 \Pi^{-5/4}$ when Π goes to infinity. In this case $\sqrt{\zeta}\Pi \to \infty$, and we have, for the left-and side of equation 4.28:

$$\frac{1}{\mathcal{R}\tilde{X_0}^{3/8}}\left(\mathcal{T}\sqrt{\zeta}\Pi - \frac{1}{\sqrt{\zeta}\Pi}\right) \sim \frac{\mathcal{T}}{\mathcal{R}}\beta\,. \tag{4.36}$$

For the right-and side, and with the intuited power law behavior for ζ_s, we have $\zeta_s \to 0$ and $\frac{8\sqrt{\zeta}}{5}\tilde{X_0}^{5/8} \to \frac{8\beta}{5}$ in the large pressure limit. Therefore, using development of Bessel functions at 0:

$$\mathrm{J}_{4/5}\left(\frac{8\sqrt{\zeta}}{5}\right) \sim \frac{1}{\Gamma(9/5)}\left(\frac{4\sqrt{\zeta}}{5}\right)^{4/5} \quad , \quad \mathrm{Y}_{4/5}\left(\frac{8\sqrt{\zeta}}{5}\right) \sim -\frac{\Gamma(4/5)}{\pi}\left(\frac{5}{4\sqrt{\zeta}}\right)^{4/5} \quad , \tag{4.37}$$

and using the definition of $\mathcal{C}_\nu$ we have

$$\mathcal{C}_{-1/5}\left(\frac{8\sqrt{\zeta}}{5}\tilde{X_0}^{5/5}\right) \sim -\frac{\Gamma(4/5)}{\pi}\left(\frac{5}{4\sqrt{\zeta}}\right)^{4/5} \mathrm{J}_{-\frac{1}{5}}\left(\frac{8\beta}{5}\right), \tag{4.38}$$

$$\mathcal{C}_{4/5}\left(\frac{8\sqrt{\zeta}}{5}\tilde{X_0}^{5/8}\right) \sim -\frac{\Gamma(4/5)}{\pi}\left(\frac{5}{4\sqrt{\zeta}}\right)^{4/5} \mathrm{J}_{\frac{4}{5}}\left(\frac{8\beta}{5}\right). \tag{4.39}$$

Substituting in the right-hand-side of equation 4.28, we obtain:

$$\frac{\mathcal{C}_{-1/5}\left(\frac{8\sqrt{\zeta}}{5}\tilde{X_0}^{5/8}\right)}{\mathcal{C}_{4/5}\left(\frac{8\sqrt{\zeta}}{5}\tilde{X_0}^{5/8}\right)} \sim \frac{\mathrm{J}_{-1/5}\left(\frac{8}{5}\beta\right)}{\mathrm{J}_{4/5}\left(\frac{8}{5}\beta\right)}\,. \tag{4.40}$$

Then, combining Eqs. 4.28, 4.36 and 4.40, and using the unicity of the limit we have:

$$\frac{\mathcal{T}}{\mathcal{R}}\beta = \frac{\mathrm{J}_{-1/5}\left(\frac{8}{5}\beta\right)}{\mathrm{J}_{4/5}\left(\frac{8}{5}\beta\right)}. \tag{4.41}$$

A simple analysis of the function $z \to \mathrm{J}_{-1/5}(z)/\mathrm{J}_{4/5}(z)$ shows that Eq. 4.41 always has a real solution, which validates the hypothesis on the scaling. We finally have $\tau_t = \tau_c \Pi^{-3/4}/\beta^2 = \tau_c/(\beta^2 P_{0,\infty}^3)$ for large pressures.

Annex 2: Impact of soft compliance for TIRFM experiments

Here we show a corrected version of figure 3.5 and 3.8, that takes into account the channel deformation for shear-stress evaluation. The correcting factor was calculated using equation 4.14, assuming $p^* = 2000$ mbar, and $x/L = 0.5$. The correction is negligible at low pressure, and minor for the highest pressure used (700 mbar), such that the difference between the graphs with and without correction remains within error bars.

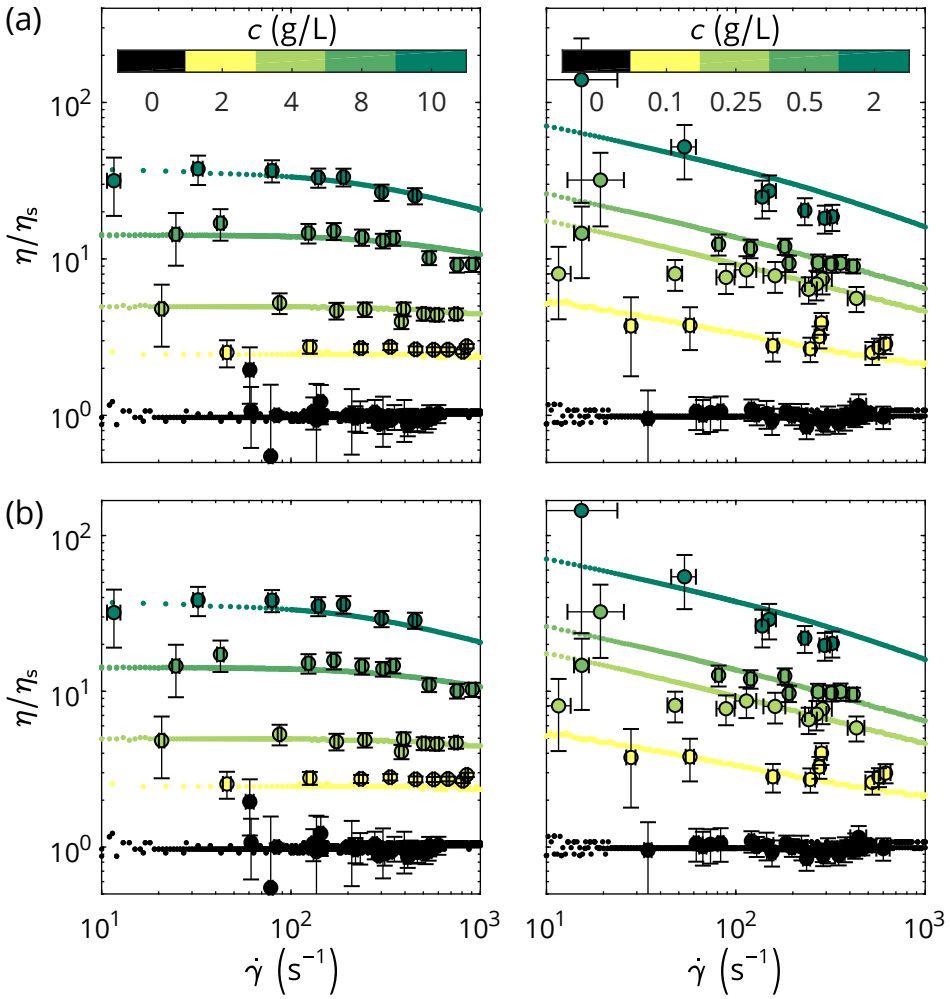

Figure 4.14: Reproduction of figure 3.5, (a) without and (b) with shear stress correction.

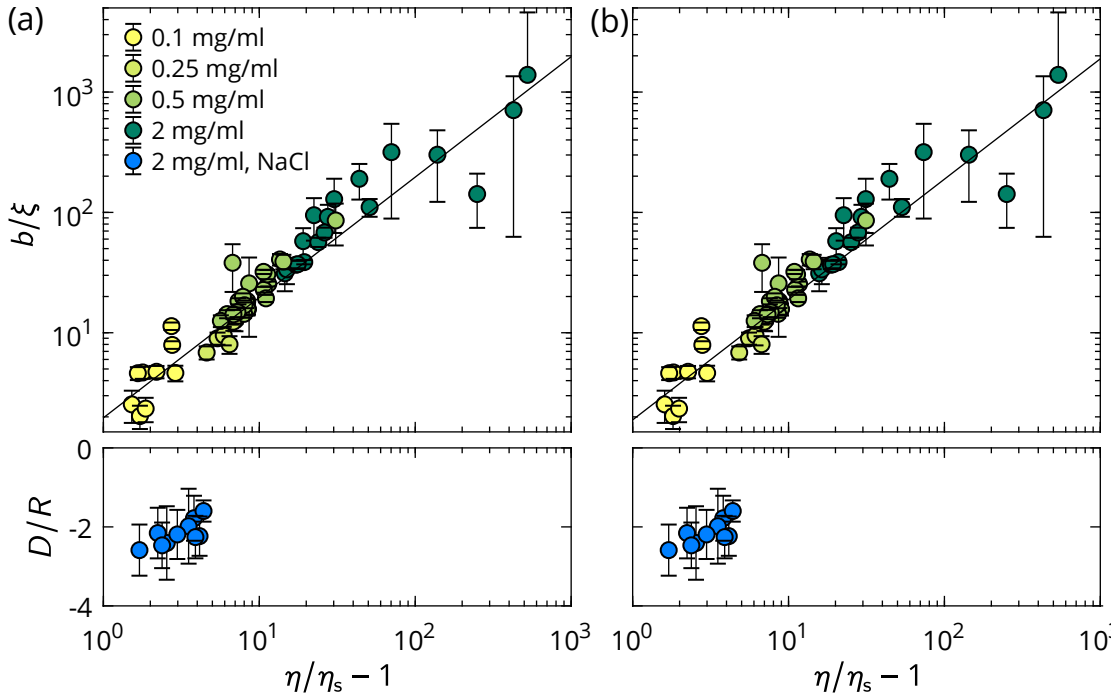

Figure 4.15: Reproduction of figure 3.8, (a) without and (b) with shear stress correction.

Chapter 5

Perspectives

The idea of this last part is to explore new routes for possible future work, in the light of the results obtained in the previous chapters. Below we provide a description of two experiments, accompanied with preliminary results. In section 5.1 we combine the tools described chapter 3 and 4 to provide simultaneous investigation of local and global flow properties, in a dynamic way. In section 5.2 we attempt to generalize the elasto-hydrodynamic experiment to oscillatory flows.

5.1 Simultaneous dynamical flow rate and TIRFM measurement

In chapter 3 we have shown how TIRFM allows to investigate hydrodynamics in the near-surface region of a solid surface for both simple and complex fluids. Conversely in chapter 4 we have shown a flow rate analysis in microfluidic channels, the latter arising from the integration of the velocity profile over the entire cross section. We now attempt to combine these two experimental methods to propose descriptions that are both local and global. Achieving such simultaneous measurements is a challenge. The main issue is that the fluidic sensors are to be used with utrapure water only. Tracer particles, but more importantly complex fluids may clog the thin 25-µm-diameter glass capillary of the flow sensor and make data unreliable. To bypass this problem, we propose to use a sequential fluid injection procedure. In section 5.1.1, we described the associated experimental setup, and in section 5.1.2 we give some preliminary result regarding the dynamic of polymer adsorption.

5.1.1 Experimental setup

Microfluidic circuit and injection procedure

The microfluidic and TIRFM equipment used here were the same as described in chapter 2. The setup, sketched in figure 5.1 was built around a large-volume intermediate chamber, with two T-junctions at its inlet and outlet. Practically, this reservoir consisted of a plastic transparent tube of length 1 m, and internal diameter 0.8 mm, ensuring a quasi-infinite internal volume of 0.5 mL, and a negligible hydraulic resistance of approximately 1×10^{11} Pa s/m^3 compared to the resistance of the microchannel filled with water. The two inlet branches, labeled 1 and 2, were filled with independent fluid reservoirs, respectively connected to the 0-2000 mbar and the 0-200 mbar channels of the pressure controller. Denote $p_{\text{in},1}$ and $p_{\text{in},2}$ the applied pressures in these reservoirs. Along branch 1 were placed the flow sensor and the pressure sensor, while branch 2 was directly connected to the T-junction. The two outlet branches, 3 and 4, were respectively connected to the microfluidic chip, and to a flushing container. The channel dimension used for this experiment was $\{h_0, w, L\}$ = {5 µm, 1000 µm, 4 cm}. All branches featured manually actuated ON/OFF valves, labeled V1 to V4, that let the fluid through with negligible resistance when open.

The injection procedure consisted of three steps, sketched in figure 5.1. (Step 1) At first, with all valves open the whole setup was flooded with ultrapure water. Reservoir 2 was then filled with the tracer-containing solution of interest. (Step 2) With valves V2 and V4 closed, the intermediate chamber was filled by setting $p_{\text{in},2} > 0$. Note that, despite the fluid of interest being possibly viscous, and the reservoir of large volume, this filling step was actually fast because of the small resistance of branches 2 and 4. (Step 3) Finally, V2 and V4 were closed and V1 and V3 were opened. With ultrapure water in reservoir 1, and by setting $p_{\text{in},1} > 0$, the fluid contained in the intermediate chamber was pushed toward the chip. This way, the flooding of the microchannel was monitored by measuring in real time the flow rate $q(t)$, the inlet pressure $p_0(t)$, while the flow was imaged by TIRF microscopy. Steps 2 and 3 may be repeated for sequential injection with different fluids.

In this experiment TIRFM was used in a dynamic way. With the same acquisition settings as in chapter 3, a recording took a snapshot of the flow over a 5-second window, and accounting for the buffering lag, a video was taken typically every minute. The particle tracking and data analysis procedure were then the same as described in chapter 2, and the observation zone was set in the middle of the chip, at $x/L = 0.5$.

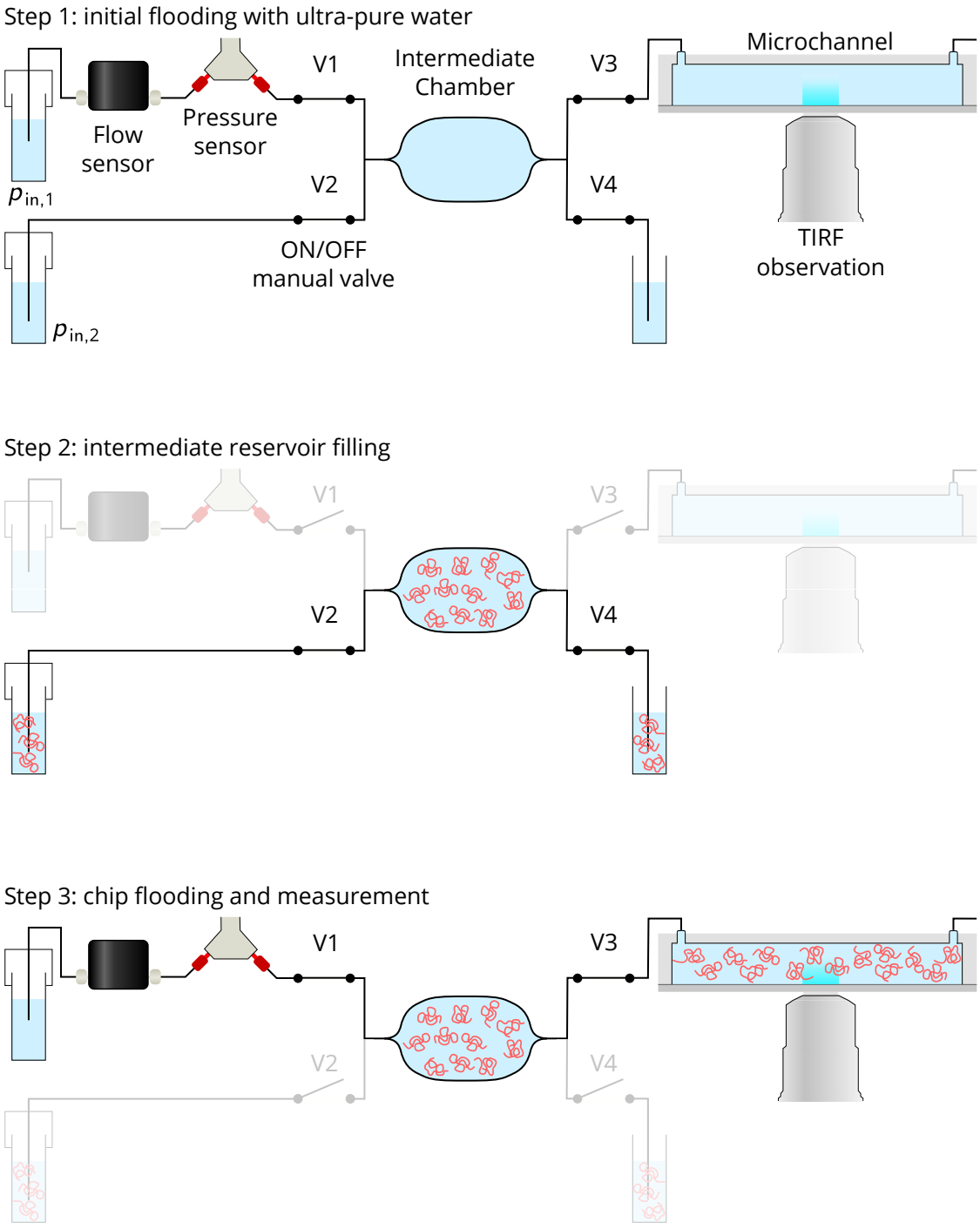

Figure 5.1: Schematics and injection procedure for combined TIRFM and flow rate measurement.

Solution preparation

For this experiment, a different kind of polymer were used. While still belonging to the family of hydrolized polyacrylamide, the commercially available Flopaam 3630S (SNF Floerger) has an estimated molecular weight of 16×10^6 g/mol, and a hydrolization rate of 30 %. These polymers are widely used for enhanced oil recovery and have been extensively studied in this context [132, 171]. In this study they were used at a concentration of 1 g/L, and with 6 g/L of salt. With such a long molecular weight, sample solutions were prepared with particular care, as we now describe. To start with, the salt-containing solvent was prepared by dissolving solid NaCl (Sigma Aldrich,>99 %) in ultra-pure water (Milli-Q, 18.2 MΩ cm). A volume of typically 200 mL of this brine was transferred in a beaker and vigorously agitated with a magnetic stirrer. Solid HPAM was slowly and carefully added in the vortex grain by grain to achieve homogeneous dispersion of the grains. After the introduction of solid polymer grains the mixing velocity is decreased, and the solution is left under agitation, for a total mixing time of 10 minutes. The mixture was then transferred to a sealed bottle and left under gentle agitation on an orbital shaker for 40 hours. Finally, the solution was filtered using a nitrocellulose membrane filter (Merck, 5 µm pore size), kept in a fridge and used within a week. For TIRFM experiments, tracer particles were added as described in section 2.3.1.

The sequence of injection for this experiment was the following. First, a solution of tracer-particles in ultrapure water was injected, and a pressure sweep was performed for calibration purposes. Then the HPAM and tracer-containing solution was injected at constant pressure $p_{\text{in},1}$ = 100 mbar for 16 hours, during which the flooding process is monitored. After that, the channel was flushed with water. Finally a solution of water and particles was injected and a last pressure sweep was carried out. The origin of time is taken at the beginning of HPAM injection.

5.1.2 Results

Before and after flooding comparison

To start, we focus the comparison between the water flows, measured before and after flooding with HPAM. In figure 5.2 is shown the steady state flow rate as a function of pressure in the two cases. Both data sets are well fitted by the soft hydraulics model described in chapter 4, see equation 6.5. However we notice a decrease in permeability after polymer flooding, which can quantified by studying the curve fitting parameters. In the following we use the subscripts BF and AF to refer to the calibration data and the after flooding data, respectively. We have

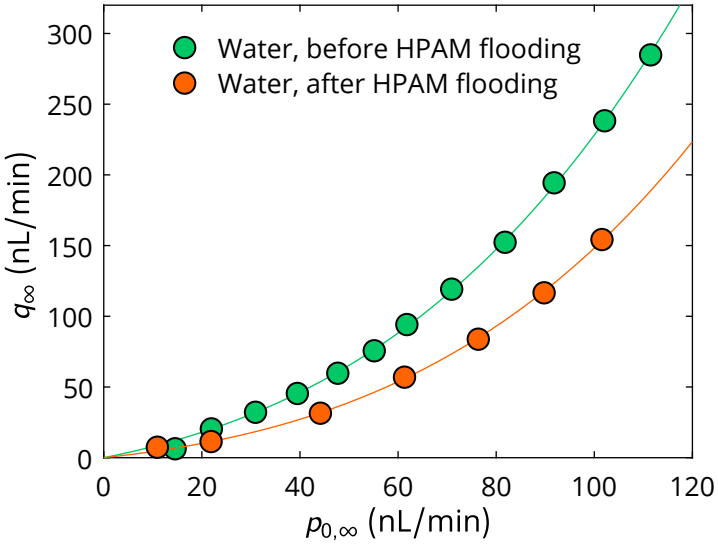

Figure 5.2: Flow rate as a function of inlet pressure measured for a flow of water in a thin microfludic channel, before and after flooding of HPAM, at steady state. The solid lines are fits to equation 6.5.

$p^*_{BF} = 113 \pm 1$ mbar and $r_{c,BF} = (8.7 \pm 0.3) \times 10^{15}$ Pa s/m^3, while $p^*_{AF} = 94 \pm 2$ mbar and $r_{c,BF} = (1.6 \pm 0.1) \times 10^{16}$ Pa s/m^3.

Recalling the theoretical expressions $p^* = E^* h_0/w$ and $r_c = 12\eta L/w h_0^3$, the experimental results can be explained by an apparent decrease of the underformed height h_0, since we have $p^*_{AF}/p^*_{BF} \approx (r_{c,AF}/r_{c,BF})^{-1/3} \approx 0.8$. In the same spirit as chapter 3, we explain this observation by the presence of an adsorbed layer at channel walls, that decreases the effective channel height by approximately 1 µm. This number is to be compared to the bulk chain size, which is here difficult to estimate. Equation 3.3 provides the order of magnitude $R \approx 900$ nm in our experimental conditions, while the value of $R = 292$ nm is reported in the literature in similar conditions [172]. From equation 1.33, and the intrinsic viscosity value $[\eta] = 4.982$ L/g according to [132], we obtain $R = 680$ nm. In all cases, the order of magnitude is compatible with the observed decrease of permeability.

To further compare the effect of HPAM flooding on the flow, let us now turn our attention to TIRFM data. In figure 5.3 are plotted the TIRFM-measured velocity profiles for water flows before and after HPAM flooding. The wall position was determined using the before-flooding experiment, and the penetration length from the pressure *vs.* shear rate curve, as detailed in the next paragraph. After flooding, the profiles extrapolate to zero velocity approximately 100 nm inside the channel, similarly to the neutral polymer data describes in section: 3.2.2.

We provide here the same explanation: after flooding, an immobile layer of adsorbed chains shift the no-slip plane. This observation is consistent with the behavior described in chapter 3 for samples containing HPAM and salt. The new data suggest that the adsorbed layer survives flushing with pure water. However the numbers measured here do not match quantitatively the permeability loss of previous section, that are associated to an effective decrease in height of 1 µm. Even if adsorption may occur at the top surface, where TIRFM cannot measure the flow, there seem to be a discrepancy between the locally-measured velocity profiles and the global flow rate.

We now study the experimentally measured shear rate for this set experiments. In figure 5.4 (a) we plot the experimentally-measured shear rate as a function of pressure. The penetration length Π could not be measured with the *in situ* incident angle measurement, but was estimated to 92 nm with a method described later. For now we use the variable $\Pi\dot{\gamma} = -\partial v_x/\partial \log(I)$ expressed in µm/s. After flooding, the data shows a decrease of permeability, that is qualitatively consistent with the data of figure 5.2. To account for the channel deformation, which is clearly significant in this experiment, judging by the superlinear flow rate *vs.* pressure curves, we use the expression of equation 4.12, namely:

$$\sigma_{xy} = \frac{h_0 p^*}{8L}\left[\left(1+\frac{p_{0,\infty}}{p^*}\right)^4 - 1\right]\left[\left(1-\frac{x}{L}\right)\left(\left(1+\frac{p_{0,\infty}}{p^*}\right)^4 - 1\right) + 1\right]^{-1/2} . \tag{5.1}$$

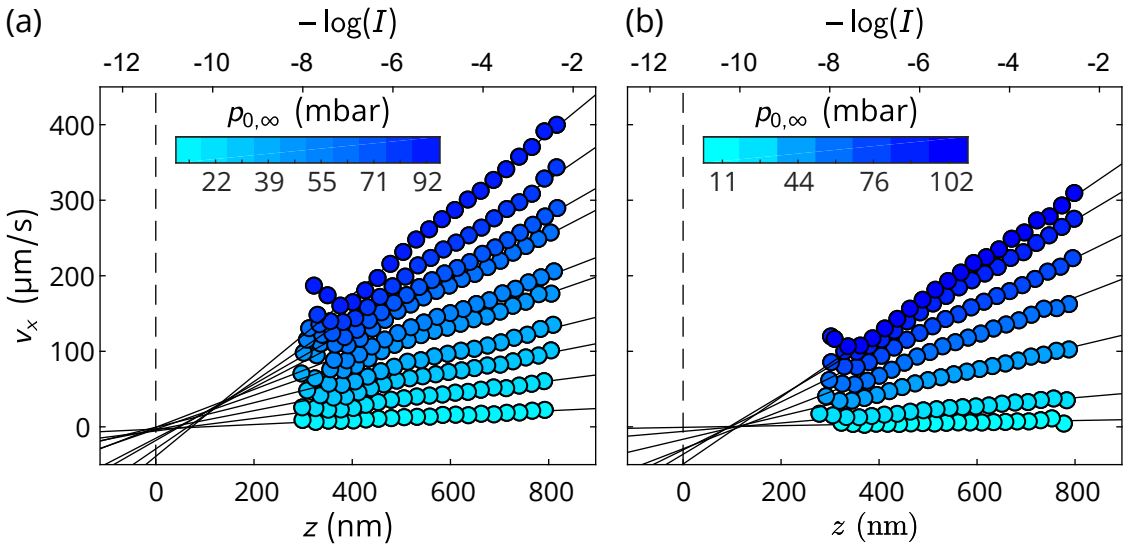

Figure 5.3: Streamwise velocity v_x as a function of the distance z to the wall – or equivalently as a function of $-\log(I)$ – for different inlet pressures, (a) before and (b) after flooding with HPAM.

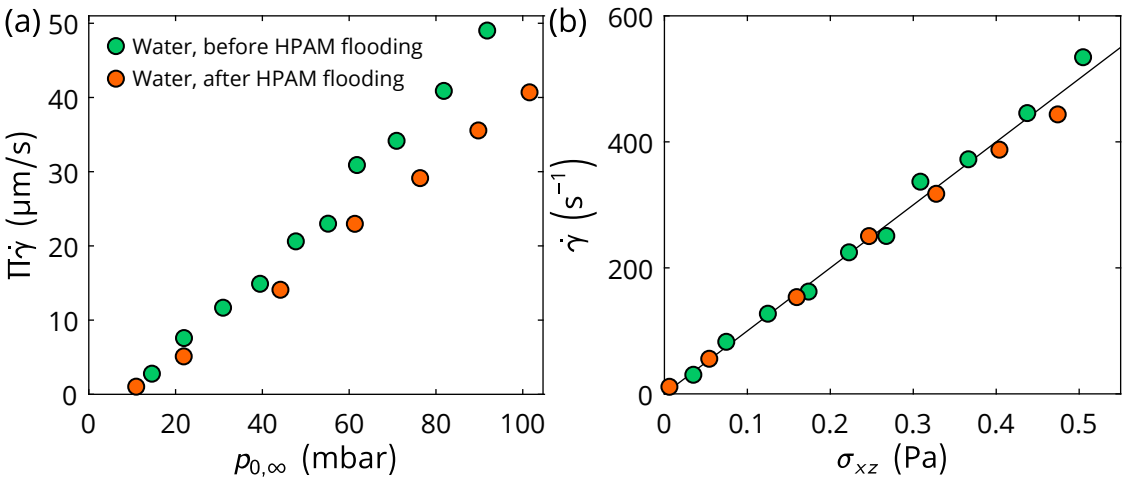

Figure 5.4: Flow rate as a function of inlet pressure in a thin microfludic channel, before and after flooding of HPAM, and measured at steady state. The solid lines are fits to equation 6.5.

Using for h_0 and p^* the values extracted from the fitting of the flow rate *vs.* pressure curves of figure 5.2, and choosing Π such that the data is compatible with the accepted value of the water viscosity, 1.0 mPa s, the two dataset collapse on a straight line, as can be seen in figure 5.4 (b). The value of the penetration length extracted with this method is Π = 92 nm, a value that is in the range of what is typically obtained in our TIRFM experiments.

To achieve the collapse of the strain *vs.* stress curve, measured locally with near-wall velocimetry, we had to use global parameters that quantifies the channel size and mechanical deformation. This example thus illustrates the complementarity of TIRFM and flow rate measurement.

In this section we have measured the adsorption of HPAM on glass surfaces in the presence of salt, with two independent methods. Although showing a quantitative discrepancy, the local TIRFM, and global flow rate measurements both indicate a decrease in the permeability of the microfluidic channel, after it has been exposed to polymers for several hours. We now address the question of the adsorption dynamics as they were measured in the intervening period between the pre- and post-flooding water measurements.

Dynamical adsorption

In this section we study the flooding process and adsorption dynamics of the HPAM solution in a microchannel. In figure 5.5 we show the-real time flow rate $q(t)$ and inlet pressure $p_0(t)$. A striking feature of these two signals is that they

are symmetrical. This can be rationalized by writing the pressure *vs.* flow rate relation of the flow sensor, which has been demonstrated in section 4.2 to be an ideal resistance r_0; hence we have $p_{\text{in}} - p_0(t) = r_0 q(t)$. The latter formula being valid at all times, and p_{in} being constant, the two signals are logically inverted, so we will arbitrarily focus only on the flow rate.

In the curve of q(t), we observe four main regions:

- a first constant domain until $t_1 \approx 2700$ s
- a quickly decaying window between t_1 and $t_2 \approx 3100$ s
- a slowly decreasing zone between t_2 and $t_3 \approx 7300$ s
- a final constant domain for $t > t_3$.

We interpret this signal as follows. Until t_1, the polymer is traveling in the pipes, and has not reached yet the chip. At t_1, the polymers start flooding the chip. As more and more viscous material enters the channel, the flow rate decreases. At t_2, the chip is entirely filled with polymers. This statement is consistent with the fact that the volume injected between t_1 and t_2 is close to the internal volume of the deformed channel: $\int_{t_1}^{t_2} q(t)\mathrm{d}t = 380\ \text{nL} \approx wLh_0(1 + p_0/p^*)$. Note that the

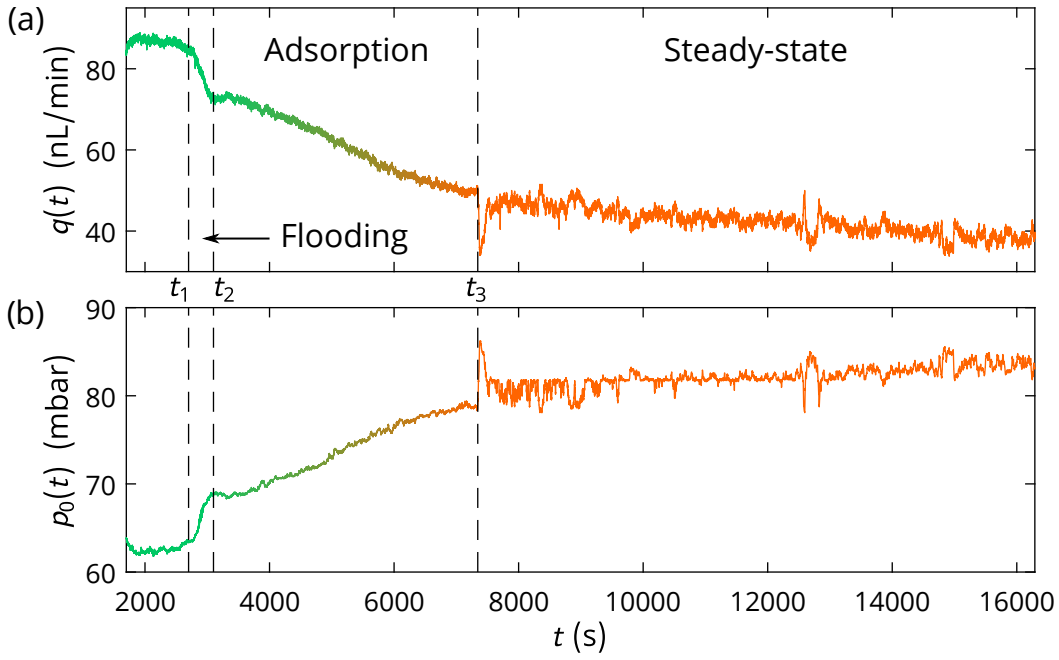

Figure 5.5: Dynamical (a) flow rate and (b) pressure measured at channel inlet, upon flooding with an HPAM solution.

actual internal volume required proper integration of the x and y-dependent height profile of the channel, which is beyond the scope of this study but was done elsewhere [167].

After t_2, adsorption starts to occur, gradually clogging the channel by decreasing its effective height. As a result of the associated permeability drop, the flow rate decreases from 73 nL/min to 45 nL/min, and the inlet pressure increases from 69 mbar to 82 mbar. These numbers are compatible with a decrease in the apparent channel height of 20 %, consistent with the flow rate measurements in water before and after flooding. While the filling of the chip takes typically 5 minutes, the adsorption process takes approximately 70 minutes.

With such long time scales, dynamic TIRFM measurements are possible. In figure 5.6 is plotted a sequence of velocity profiles measured during the adsorption phase, between t_2 and t_3. From these profiles we extract the shear rate $\dot{\gamma}$ and the adsorbed layer thickness D, which are plotted as a function of time in figure 5.7. We observe a decrease of the shear rate that is consistent with a permeability drop. However the curve of D as a function of time also decreases, which is inconsistent with the previous observation. The velocity profiles also do not seem perfectly straight, an effect for which we do not have an explanation so far, so far, and which was not seen in the experiments with the salted polyelectrolytes used in chapter 3. A hypothesis not considered so far is that the

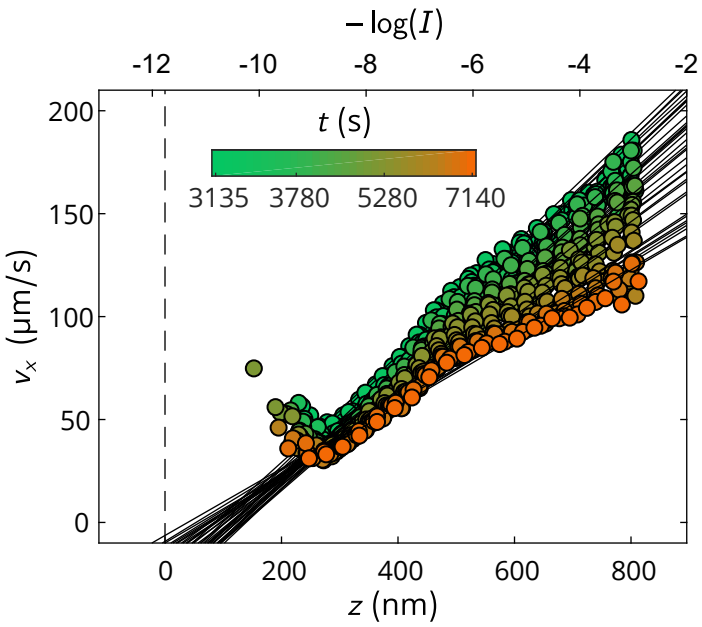

Figure 5.6: Time-dependent velocity profiles, measured in HPAM between t_2 and t_3 during the adsorption phase. Straight lines are linear fits of the data.

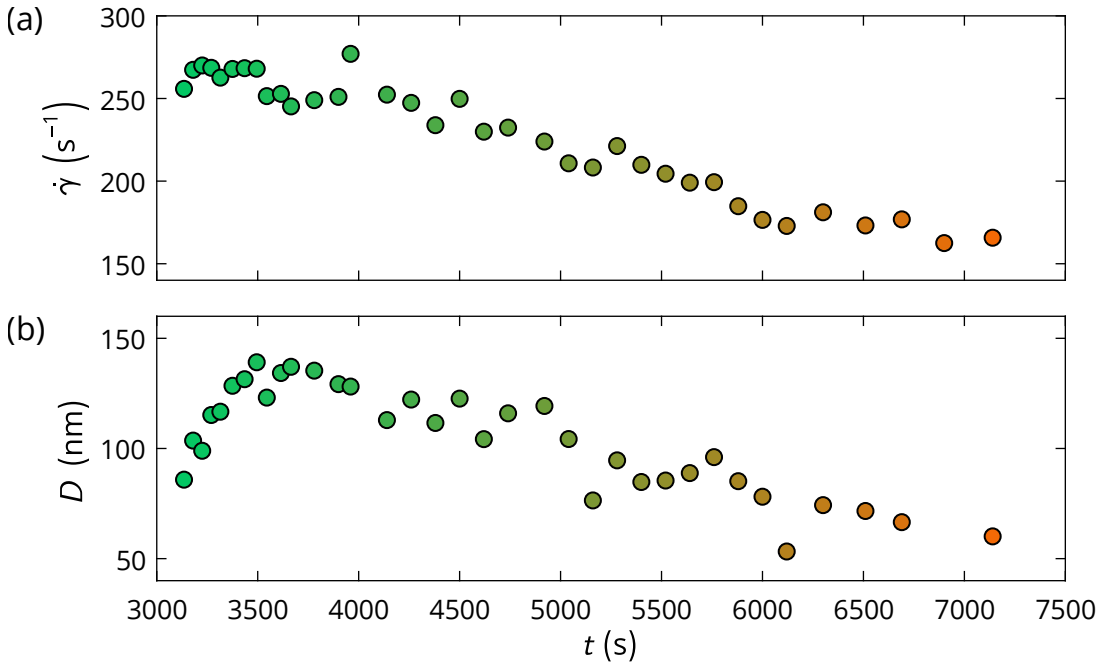

Figure 5.7: (a) Shear rate and (b) adsorbed layer thickness as a function of time, extracted from the profiles of figure 5.6.

observed extrapolation length may be the result of both adsorption and slip. In the situation where there would be slip over an immobile layer, the two effects may compensate for TIRFM observation.

Overall the combined local and global approaches to polymer microchannel flooding and fouling presented here show qualitative agreement; however, a quantitative discrepancy remains. When flowing an polymer solution on an adsorbing surface, we observe a decrease of permeability, which has an impact on the near-wall shear rate and the flow throughput. With dynamical measurement we were able to establish the permeability loss occurs over typically one hour, which we associate to the adsorption equilibrium time scale. From a practical point of view, this preliminary experiment demonstrates that, with a proper injection setup, it is possible to use water-only fluidic sensors with complex fluids, and that TIRFM velocimetry can be use to perform time-dependent measurements. These features pave the way toward more sophisticated experiments in the near future.

5.2 Oscillatory flows in compliant microchannels

In chapter 4 we investigated the transient relaxation dynamics of compliant microchannels under a sudden change of pressure. The results notably highlighted a pressure-dependent time scale τ_{exp}, which was rationalized using an elasto-hydrodynamic model. A follow-up question that arises is the response of these microchannels to any input signal $p_{in}(t)$. We know from Fourier analysis that any physical signal may be described as a superposition of oscillatory functions. This remarkable feature makes it particularly interesting to know the response of a linear system to sinusoidal inputs. In electronics it is common to work with oscillatory signals – every-day life appliances work on alternative current – such electronic setups are often characterized with frequency diagrams. These so-called Bode diagrams typically show the gain and phase of an output signal, with respect to an input signal, as a function of frequency.

From a fluidic point of view, oscillatory flows offer many relevant applications, as review by Dincau *et al.* [173]. Fluid manipulation perspectives include enhanced mixing [174], clog mitigation [175] or particle separation [176], to name a few examples. In biological systems, too, oscillations are ubiquitous, as in blood flows for example [177]. Here, we provide here an analysis of the response our soft microchannels to oscillatory pressure input.

5.2.1 Experiment

We used the exact same setup as in chapter 4 and depicted in figure 2.8, with a channel of dimensions $\{h_0, w, L\}$={5 µm, 200 µm, 4 cm}. This time instead of applying a cascade of pressure drops, we applied an oscillatory input pressure of the form:

$$p_{in}(t) = \langle p_{in} \rangle + A_{in} \sin(\omega t)\,. \tag{5.2}$$

In the latter equation, $\langle p_{in} \rangle$ denotes the pressure offset, A_{in} is the oscillation amplitude, and ω is the angular frequency. The pressure controller we used has a response time of approximately 0.1 s, allowing to input sinusoidal signals of frequency up to typically 0.2 Hz. With such signal as input, we recorded the inlet pressure $p_0(t)$ and flow rate $q(t)$ in the steady-state regime. These output signals were fitted with a sinusoidal curve, from which we extract the amplitudes A_p and A_q, and the phases ϕ_p and ϕ_q of $p_0(t)$ and $q(t)$, respectively. In this experiment, both $\langle p_{in} \rangle$ and ω were varied, while the input amplitude A_{in} = 20 mbar was kept constant.

5.2.2 Results and discussion

A typical data set is shown in figure 5.8, with $\langle p_{in} \rangle = 475$ mbar, and $\omega = 4.31 \times 10^{-3}$ rad/s. In the top graph, (a) is shown the sinusoidal input signal $p_{in}(t)$, while the bottom graph, (b), displays the output signals $p_0(t)$ and $q(t)$ as colored lines. The latter curves are purely sinusoidal, as indicated by the fits in black lines. The absence of visible deviation from a sine shape is characteristic of a linear response. Yet the output signals display a phase difference with one another, and with respect to the input. We now study the frequency response of the system by plotting Bode diagrams.

Figure 5.9 shows (a) the gain G, defined as A_p/A_q, and (b) the phase difference $\Delta\phi = \phi_p - \phi_q$ as a function of the angular frequency, for different input offsets. For all the curves, the gain plateaus at low frequencies, and decays as a power law above a characteristic frequency. Simultaneously the phase $\Delta\phi$ continuously decreases from 0 to $-\pi/2$. The curves also strongly depend on the pressure offset.

We now attempt to rationalize these observations. As described in chapter 3, soft microfluidic channels display both resistance and capacitance. We also emphasized the important role of the sensors. Here, we will simplify the problem, assuming that the flow sensor is an ideal resistance r_0, and the ensemble { channel + pressure sensor } is a pressure-dependent resistance $\tilde{r}_c$ in parallel with a pressure-dependent capacity $\tilde{c}_0$. The equivalent electric circuit is schematized in figure 5.10. Since the oscillations are small, we assume that the system

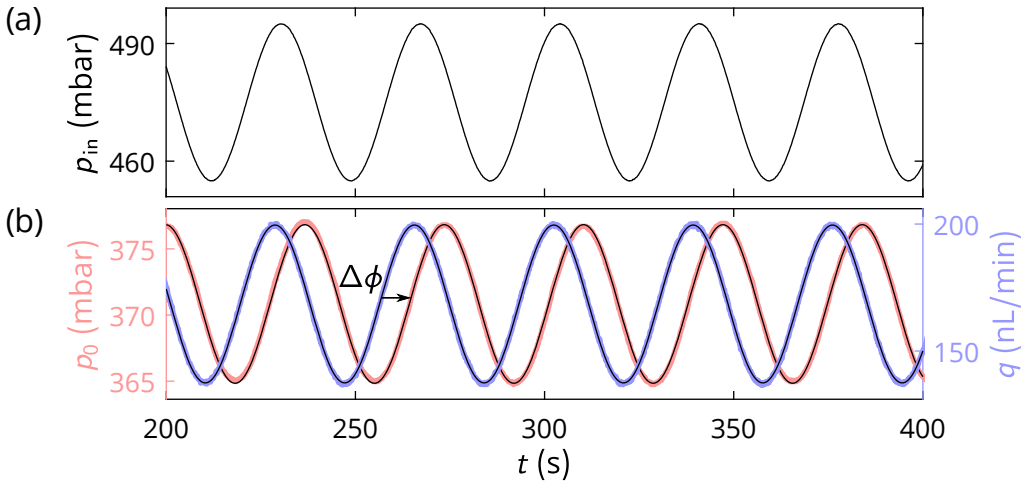

Figure 5.8: (a) Input signal $p_{in}(t)$ and (b) output signal $p_0(t)$ and $q(t)$ for an oscillatory flow at the angular frequency $\omega = 4.31 \times 10^{-3}$ rad/s and an offset $\langle p_{in} \rangle = 475$ mbar. Thin black lines are sinusoidal fits of the data.

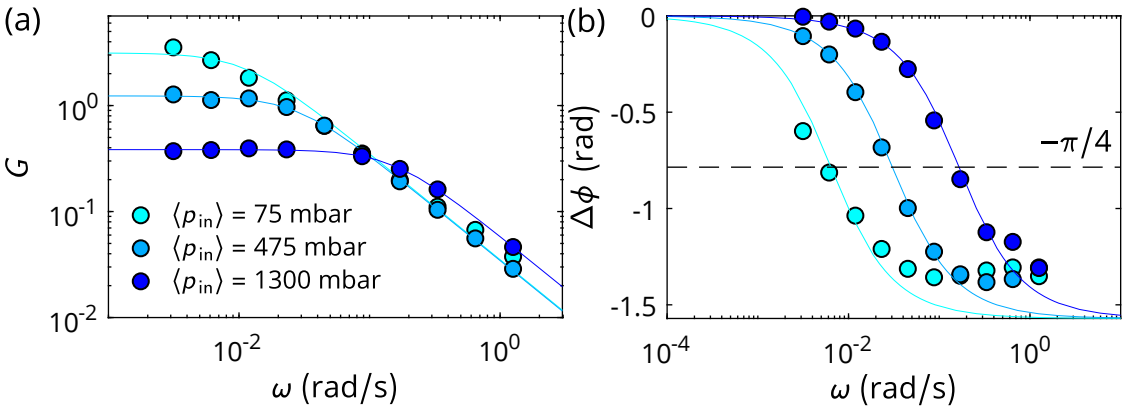

Figure 5.9: (a) Gain, defined as the ratio A_p/A_q (unit: mbar min/nL), and (b) phase difference $\Delta\phi = \phi_p - \phi_q$ as a function of the angular frequency, for different offset values. Solid lines are fit according to equations 5.4 and 5.5, respectively.

can be locally linearized, such that we can apply the linear filter theory in spite of the non-linear components. In this framework, the complex amplitudes $\underline{q}$ and $\underline{p_0}$ of the oscillating flow rate and inlet pressure are connected by the complex impedance $Z(j\omega)$, that is an order-1 low-pass filter:

$$\underline{p_0} = Z(j\omega)\underline{q} \quad \text{with} \quad Z(j\omega) = \frac{G_0}{1 + j\omega/\omega_0} . \tag{5.3}$$

In the model we also have $G_0 = \tilde{r}_c$ and $\omega_0 = 1/\tilde{r}_c\tilde{c}_0$. The frequency-dependent gain $G(\omega)$ and phase shift $\Delta\phi$ read:

$$G(\omega) = |Z(j\omega)| = G_0 \left(1 + \frac{\omega}{\omega_0}\right)^{-1/2} , \tag{5.4}$$

$$\Delta\phi(\omega) = \arg\left(Z(j\omega)\right) = -\arctan\left(\frac{\omega}{\omega_0}\right) . \tag{5.5}$$

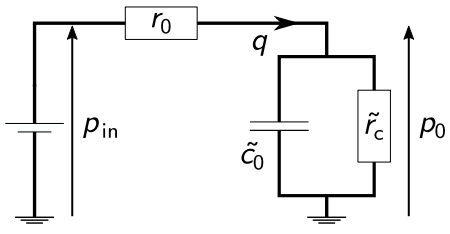

Figure 5.10: Equivalent electric circuit, to model the oscillation response of a soft microfluidic chip.

Using ω_0 and G_0 as free parameters, the data of figure 5.9 are fitted with this model. Concerning the gain curve the two largest-offset curves are well described by this model. The lowest-offset curve show a power law decay slightly below 1, and the plateau could not clearly be be reached. For the phase curves, all the data show a discrepancy at large frequency: the curves do not saturate at the predicted value of $-\pi/2$. At low frequency, the two-darkest curves shows good agreement, while the lowest-offset curve only show qualitative agreement, with an less sharp inflection point.

The values obtained for G_0 and ω_0 are offset-dependent: when $\langle p_{\text{in}} \rangle$ increases, G_0 decreases and ω_0 decreases. This observation is consistent with the expressions derived above, and our analysis of chapter 4. For the three offset values tried here, we obtained $1/\omega_0 = \{ 160, 34, 6.6 \}$ s for $\langle p_{\text{in}} \rangle = \{75, 475, 1300\}$ mbar. This broad range of time scales is systematically larger than the times obtained for the relaxation experiment, especially in the low-pressure limit, which is another proof that the linear theory developed here does not capture the entire complexity of the system.

Overall, the model described here catches qualitatively the behavior of compliant microfluidic chips under oscillatory flows. We observe an order-1 low pass filter behavior, with an offset-dependent cutoff frequency. Rationalizing the experimental data quantitatively would probably require a complete elasto-hydrodynamic model adapted from the one described in chapter 4. A remarkable feature of these systems is the sharp variation of the phase around the cutoff frequency. As a perspective we anticipate that this feature may be used to measure subtle effects. The cutoff frequency is likely to depend strongly on the fluid rheology, the channel geometry, and the boundary condition, therefore any change in those quantity may cause a phase shift. To make the connection with time-resolved adsorption measurement of section 5.1, a decrease in permeability would decrease ω_0, and thus increase the phase shift. In other word, the phase of the measured signals possibly encodes the quantity of adsorbed chains in the channel.

Conclusion of the chapter

In this final chapter we proposed two follow-up experiments to those described in chapter 3 and 4. First we showed how to simultaneously measure local and integrated flow properties in microchannels by combining TIRFM and flow rate *vs.* pressure measurements. This allowed us to provide preliminary results on the adsorption dynamics of HPAM polymer chains on glass in the presence of salt, and under flow. Second, generalizing the flow characterization in compliant channels to oscillatory flows, we demonstrated the low-pass filter behavior of these objects, which may be exploited to measure subtle effects in the future.

Conclusion

This fundamental study aimed at investigating flows of polymer solutions in micrometer-sized channels, with particular focus on the importance of boundaries. To achieve that goal, two complementary techniques were used. First, the microfluidic toolbox allowed us to design and fabricate microchannels efficiently. Within such devices, flows were pressure-controlled, and integrated sensors allowed the measurement of the flow rate and the pressure. Then, our lab-made evanescent wave TIRF microscope proved to be particularly well suited to image the 3D motion of tracer-particles in the vicinity of the solid bottom wall of our rectangular channel, under flow. In spite of the complex motion of these tracers, a combination of advection and Brownian diffusion, the use of tracking algorithms allowed us to extract relevant information on the local flow properties.

This setup enabled to simultaneously access the non-trivial rheology and hydrodynamic boundary conditions of complex fluids. Rationalizing our experimental data with hydrodynamics and polymer physics theories, we demonstrated that the boundary condition of semi-dilute polyacrylamide solution flows on glass surfaces were governed by electrostatic phenomena. Neutral chains adsorb at the wall strongly enough to shift the boundary condition a distance close to the polymer chain size. On the other hand charged hydrolized polyacrylamide samples, a common example of polyanionic polymers, effectively slip at the wall, with micrometric slip lengths reported. Quantitatively, the observed slip lengths were rationalized by the presence an electrostatically mediated, low-viscosity lubrication layer at the surface.

To evaluate the impact of local boundary conditions on global flow throughput we highlighted another kind of flow-boundary interaction: the mechanical elasto-hydrodynamic coupling between a soft wall and a low-Reynolds number flow. This soft hydraulics was here characterized in thin and soft rectangular microchannels. On the one hand steady state analysis revealed non-linear flow rate with respect to imposed pressure, violating Poiseuille law. On the other hand dynamical analysis emphasized the fluidic capacitance behavior of these objects, causing a finite relaxation time of the system that cannot be rationalized

by simple dimensional analysis. Our model revealed that in the small deformation limit, a constant transient time is expected, while at large deformation the latter decreases with the third power of the inlet pressure. We also showed that compliant channels behave like low pass-filters for oscillatory flows.

Finally, we proposed a experimental setup to investigate simultaneously and dynamically microscale flows combining the tools previously developed. While evanescent wave microscopy enabled local near-wall flow mapping, flow rate analysis provided global integrated measurements. Encouraging preliminary results uncovered the adsorption dynamics of hydrolized polyacrylamide on glass in the presence of salt, accompanied by a reduction of permeability.

The concluding message of the present work is that in spite of the apparent simplicity of the Stokes' equation, there is a vast phenomenolgy at interfaces that make confined flows a complex problem, especially when polymers are at play. Here we pointed out two examples: 1 – molecular interaction between a surface and a complex fluid may change the hydrodynamic boundary conditions in a non-trivial way, and 2 – mechanical coupling between a flow and its soft boundaries has a tremendous impact on large scale flows. We anticipate that proper understanding of these phenomena will prove crucial in any situation where complex microscale flows are involved.

Chapter 6

Résumé de la thèse en français

Introduction

Les milieux poreux ou confinés sont remarquables par leur large rapport surface/volume. Pour caractériser le transport de fluides dans ces systèmes, il est donc crucial de décrire la physique aux interfaces solide/liquides qui entourent les écoulements. La présence de murs immobiles impacte un champs de vitesse hydrodynamique en créant localement une condition aux limites qu'il faut caractériser. D'autre part, l'étude d'un écoulement nécessite de connaitre les propriétés rhéologiques des fluides d'intérêt. Les fluides simples, dits newtoniens, ont une réponse linéaire caractérisée par leur viscosité, cependant la matière molle offre pléthore de matériaux pouvant avoir des réponses non-linéaires ou dépendantes du temps, comme les fluides à seuils ou viscoélastiques [178].

Le but de ces travaux est d'étudier expérimentalement le comportement de solutions de polymères lorsqu'elles s'écoulent dans des milieux confinés. Cette situation est typiquement rencontrée en récupération assistée du pétrole, où de grandes quantités de mélange eau-polymère sont injectées dans des roches poreuses. Les matériaux polymères sont connus pour avoir à la fois une rhéologie complexe, et pour présenter des conditions aux limites hydrodynamiques non triviales. On parle de glissement lorsque la vitesse du fluide est non nulle à la paroi. Ce comportement s'oppose à l'hypothèse naturelle, répandue et souvent valide d'un fluide immobile au voisinage direct d'un mur fixe. On définit la longueur de glissement comme la distance sous la paroi à laquelle le profile de vitesse s'extrapole linéairement à zero. Un fort glissement a été mesuré pour les fondus de polymère avec des longueurs de glissement pouvant atteindre plusieurs microns [47, 179], et la modélisation en est aujourd'hui bien comprise [180]. Le cas des solutions diluées a lui aussi atteint une certaine maturité [181]. En revanche la situation intermédiaire des solutions de polymères

semi-diluées, régime de concentration dans lequel le chaines se recouvrent, mais qui laisse encore une part importante au interactions polymère-solvant, est encore à explorer.

Dans cette étude nous utilisons un montage de microscopie à ondes évanescentes TIRF [80] pour caractériser l'écoulement de solutions semi-diluées de polyacrylamide, dans un microcanal. Associée à un protocole de vélocimétrie par suivi de particules (PTV), cette méthode permet de mesurer le champs de vitesse de l'écoulement à proximité immédiate d'une paroi en verre avec une résolution nanométrique. Ces données renseignent simultanément sur la rhéologie de l'échantillon et sur les conditions aux limites hydrodynamiques. Nos efforts pour augmenter le niveau de confinement ont ensuite mis en lumière un couplage entre l'écoulement et la réponse élastique de l'élastomère utilisé pour fabriquer nos microcanaux. Ce couplage élastohydrodynamique sera étudié dans un second temps.

6.1 Matériel et méthodes

Nous travaillons à l'échelle d'un pore unique, en utilisant les technologies microfluidiques. Un canal rectangulaire de dimensions $\{L, w, h_0\} = \{8.8\,\text{cm}, 180\,\mu\text{m}, 20\,\mu\text{m}\}$ est fabriqué en verre/PDMS par des méthodes de lithographie décrites dans la littérature [109]. À l'intérieur de ce canal les écoulements sont générés par application d'une suppression contrôlée p_{in} en entrée de puce.

Ces écoulements sont imagés par microscopie à onde évanescente TIRF – total internal reflection fluorescence microscopy. Des traceurs sphériques fluorescents de 110 nm de diamètre sont introduits dans le fluide d'intérêt, à une concentration de 8.6×10^{13} L^{-1} soit une fraction volumique d'environ 6.0×10^{-5}. Ces traceurs sont illuminés par une onde évanescente générée par réflexion totale d'un laser, de longueur d'onde $\lambda = 488$ nm, à l'interface verre-échantillon, comme schématisé en figure 6.1 (a). Le mouvement des traceurs est observé avec une caméra haute-sensibilité, à une fréquence d'échantillonnage de 400 Hz. Le suivi individuelle des particules est réalisé par un algorithme de détection et de reconstruction des trajectoires. Un ajustement gaussien du profile d'intensité permet une détermination nanométrique de la position, et de l'intensité de fluorescence de chacun des objets détectés.

Les solutions utilisés lors de ces expériences sont faites à partir de polyacrylamides (PAM) synthétisés en laboratoire, de masse molaire 1284 et 2082 kg/mol ainsi que des échantillons du même polymère partiellement hydrolisé (HPAM) – donc possédant environ 10% de monomères chargés négativement – de masse molaire 817 kg/mol [130]. Les solutions, dont on note c la concentration massique en polymère, sont préparées par dissolution des polymères lyophilisés

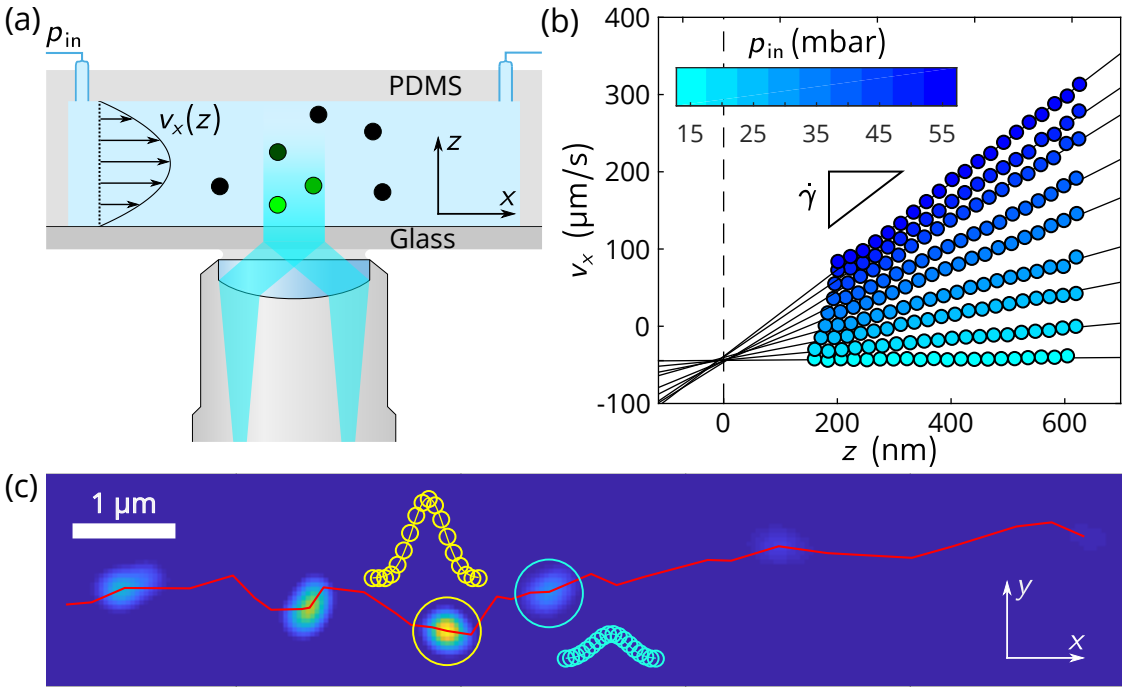

Figure 6.1: (a) Schéma d'un écoulement microfluidique observé par microscopie TIRF. Le schéma n'est pas à l'échelle. (b) Profiles de vitesse mesurés pour des écoulements d'eau pure sous différentes pressions. (c) Chronophotographie d'un traceur advecté dans un écoulement, observé par microscopie TIRF, avec la trajectoire reconstruite. La particule est montrée toute les 15 ms, et pour deux instant sont affichés le profils d'intensité du traceur.

dans de l'eau déionisée ou dans une solution de sel (NaCl). Chaque échantillon est caractérisé par une mesure de rhéologie standard en cellule de Couette.

6.2 Vélocimétrie dans les solutions de polymères

Nous nous intéressons dans cette section aux résultats de vélocimétrie en microscopie TIRF. L'intérêt de travailler avec une onde évanescente est double. Premièrement, seul une fine couche proche de l'interface est illuminée, ce qui est approprié pour étudier les phénomènes aux interfaces. En effet le champs d'onde I décroit exponentiellement dans la direction z normale à l'interface verre-échantillon:

$$I(z) = I_0 \exp(-z/\Pi)\,, \tag{6.1}$$

où I_0 désigne l'intensité du champs à $z = 0$ et Π la longueur caractéristique de décroissance de l'exponentielle. On peut démontrer en optique ondulatoire la

formule suivante: $\Pi = \lambda/4\pi\sqrt{n_g^2 \sin^2\theta - n_w^2}$, où θ est l'angle d'incidence du laser, que l'on contrôle expérimentalement, et n_g et n_w sont respectivement les indices de réfraction du verre et de l'échantillon, assimilable à de l'eau pure. L'autre avantage d'un éclairage évanescent est de pouvoir inférer l'altitude z d'un objet par la mesure de son intensité de fluorescence. En calibrant l'expérience, on peut avoir accès aux paramètres I_0 et Π, ce qui permet, en inversant l'équation 6.1, de mesurer la cote z des traceurs et donc de faire de la vélocimétrie à trois dimensions.

La figure 6.1 (b) montre plusieurs profiles de vitesse mesurés pour un écoulement d'eau pure, à différentes pressions. La vitesse moyenne des particules v_x est tracée en fonction de la distance z au mur. Chaque courbe est bien ajustée par une ligne droite, dont la pente est une mesure du taux de cisaillement local $\dot{\gamma}$. Bien que non montré dans ce document, ce dernier augmente linéairement avec la pression. Ces données sont en accord avec la théorie de Poiseuille pour les écoulements de fluides newtoniens dans les canaux rectangulaires. La linéarité des profiles de vitesse vient du fait que la zone d'observation, épaisse de 600 nm environ est très mince devant la hauteur de 20 µm du canal, le profile mesuré est donc une linéarisation proche de la paroi du profile parabolique théorique.

Deux informations importantes peuvent être tirées d'un tel graphique. Premièrement, la condition aux limites hydrodynamique, qui s'obtient par extrapolation des profiles de vitesse linéaires à $z = 0$. Ici tous les profiles se croisent au même point, que nous prenons comme définition de l'origine des z et position du mur, en supposant une condition de non glissement. Cette hypothèse est la plus naturelle pour une interface eau-verre [39]. Deuxièmement l'évolution de $\dot{\gamma}$ avec p_{in} permet de mesurer la viscosité du fluide, si l'on connait la géométrie du canal. L'expérience de vélocimétrie que nous venons de décrire permet donc de mesurer indépendamment les conditions aux limites et la rhéologie des fluides à l'interface. Pour un fluide simple comme l'eau pure, les résultats servent de calibration, notamment pour localiser le plan $z = 0$. Une expérience de la sorte est donc réalisée en amont de toute mesure dans les fluides plus complexes que nous allons maintenant étudier.

Des courbes similaires à celle de la figure 6.1(b) ont été mesurées dans des solutions de PAM et HPAM à différentes concentrations, en régime dilué ou semi-dilué. Des exemples sont montrés en figure 6.2 pour une solution de PAM de masse molaire 2082 g/mol à 2.0 g/L et pour une solution de HPAM à 0.5 g/L. Intéressons nous d'abord au comportement rhéologique de ces solutions. Pour un taux de cisaillement $\dot{\gamma}$ donnée, on peut mesurer la viscosité apparente η par la formule suivante: $\eta = p_{in} h_0/2L\dot{\gamma}$. Ainsi, chaque profile de vitesse donne accès à un point de la courbe $\eta(\dot{\gamma})$.

Les courbes de rhéologie sont affichées en figure 6.3 (a), pour plusieurs solutions de PAM de masse molaire 2082 g/mol, de concentrations comprises entre 0 et 10 g/L. La viscosité normalisée par la viscosité du solvant η_s y est tracée en fonction du taux de cisaillement. Pour les solutions les moins concentrées, jusqu'à environ 4 g/L, une concentration qui correspond approximativement à la concentration de transition entre les régime dilués et semi-dilués, la viscosité est constante sur toute la plage de taux de cisaillement accessible. Ce comportement est celui d'un fluide newtonien. Aux plus fortes concentrations en revanche, on constate un comportement rhéo-fluidifiant: la viscosité diminue avec le taux de cisaillement. Cette observation est classique dans les solutions de polymères et est comprise dans le cadre des théories standards [11, 25]. Ainsi normalisées, les données sont en accord avec les données de rhéologies mesurées en cellule de Couette, et avec un modèle théorique spécifiquement développé pour les PAM [132]. Les mesures de velocimétrie par suivie de particule en microscopie TIRF permettent donc de mesurer localement et *in situ* les propriétés rhéologiques des fluides. Passons maintenant à l'étude des conditions aux limites.

Les profiles de vitesse en figure 6.2 montrent un comportement différents dans les PAM et dans les HPAM. Dans les PAM les profiles de vitesse s'extrapolent à vitesse nulle à une distance d'environ 80 nm a l'intérieur du canal. Cette observation s'interprète par la présence d'une couche immobile de polymères absorbés à la paroi. L'adsorption de PAM sur du verre a déjà été documentée [143], et des études théoriques on montré que de l'adsorption modifie le profile de

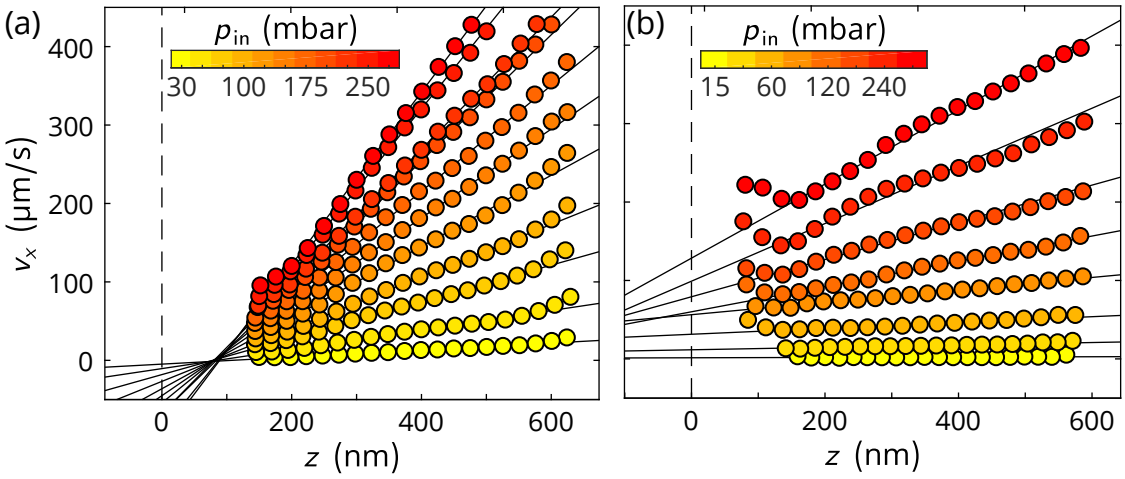

Figure 6.2: Profiles de vitesse mesurés pour différentes pressions dans (a) un solution de PAM de masse molaire 2082 g/mol et de concentration 2.0 g/l, et (b) dans une solution de HPAM à une concentration de 0.5 g/L.

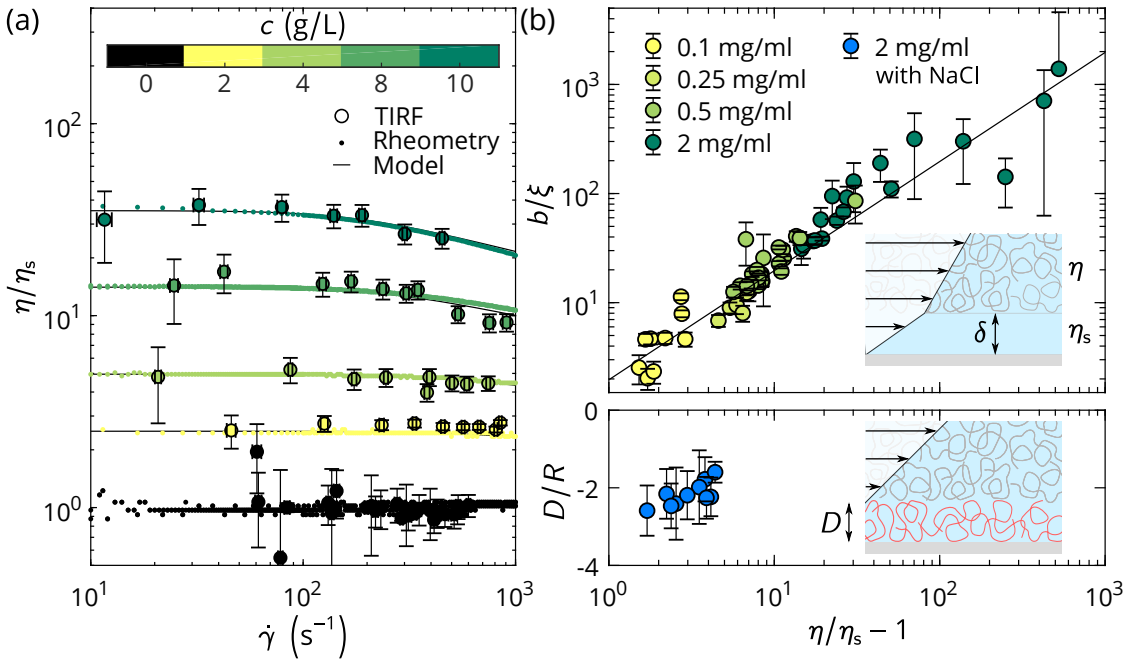

Figure 6.3: (a) Viscosité normalisée en fonction du taux de cisaillement pour différentes solutions de PAM de masse molaire 2082 g/mol. Les données mesurées par microscopie TIRF, par rhéométrie standard ainsi qu'un modèle théorique sont superposés. (b) Longueur de glissement normalisée (en haut) et épaisseur de la couche adsorbée (en bas) en fonction de la viscosité spécifique pour différentes solutions de HPAM. Les schémas illustrent dans chacun des cas le comportement des polymères à l'interface.

vitesse exactement comme observé ici [62]. En outre, l'épaisseur D de la couche adsorbée correspond à la taille attendue pour les chaines de PAM en solution. Il est à noter que D est indépendante du taux de cisaillement. Les mesures effectuées avec des chaines plus courtes (1284 g/mol), non montrées ici, présentent une épaisseur absorbée légèrement plus faible.

Les HPAM ont un comportement opposé. Les profiles de vitesse indiquent une vitesse non nulle à la paroi, que l'ont peut quantifier par une longueur de glissement dépendante du taux de cisaillement et de la concentration. Pour expliquer ces observations, nous utilisons un modèle stratifié schématisé en figure 6.3 (b). Parce que les HPAM et la surface de verre sont tout deux chargés négativement, nous faisons l'hypothèse d'une couche de dépletion, d'épaisseur δ, à l'interface verre/échantillon, dans laquelle il n'y a pas de polymères. Cette région, où la viscosité est donc plus faible, agit comme une couche de lubrification. Par continuité de la contrainte, le profile de vitesse résultant loin de l'interface

semble donc présenter un glissement apparent, dont la longueur de glissement suit la loi suivante: $b = \delta(\eta/\eta_s - 1)$. La physique des polymères prévoit que δ doit être de l'ordre de la longueur de corrélation ξ, c'est-à-dire la taille de la maille dans un réseau de chaines régime semi-dilué [145, 56]. Une loi d'échelle pour cette dernière prévoit $\xi \propto c^{-1/2}$ pour les polyélectrolytes [18]. En estimant ξ pour nos concentrations expérimentales, on trace en figure 6.3 (b) b/ξ en fonction de la viscosité spécifique $\eta/\eta_s - 1$. Les données tombent sur une droite de pente 1 en échelle logarithmique indiquant la proportionnalité attendue entre les grandeurs affichées, ce qui corrobore le modèle à deux couches. En outre le coefficient de proportionnalité est bien de l'ordre de l'unité. Notons que nos estimations pour ξ sont de l'ordre de la dizaine de nanomètres, ce qui explique que l'on ne puisse pas voir la couche déplétée au microscope TIRF. Pour donner un ordre de grandeur, les longueurs de glissement apparent les plus importantes mesurées ici sont de l'ordre du micron.

L'expérience a aussi été réalisée en présence de sel. L'ajout d'électrolytes dans une solution de polymères chargés change les propriétés du liquide en écrantant les interactions électrostatiques, à la fois entre monomères mais aussi entre les chaines de polymères et la paroi en verre. En diminuant la répulsion électrostatique avec le mur, on retrouve une condition aux limites de type couche adsorbée, comme l'indique la figure 6.3. De nouveau, D est l'ordre de la taille de R de la chaine, estimée selon une loi d'échelle de la littérature [18].

Nos résultats ont donc montré que les solutions PAM peuvent présenter différentes conditions aux limites hydrodynamique sur une surface en verre en fonction de leur état de charge, et la présence de sel dans la solution. Par sa capacité à mesurer simultanément et indépendamment rhéologie et conditions aux limites, l'utilisation de la microscopie TIRF se révèle un outil performant pour traiter les problématiques d'hydrodynamique des polymères aux interfaces.

6.3 Écoulements dans les canaux déformables

Dans la section précédente nous avons mesuré du glissement de façon locale et directe en imageant des écoulements à la paroi. Une autre méthode consiste à mesurer l'impact macroscopique du glissement sur le débit de fluide obtenu pour une pression donnée. En effet on peut montrer que la condition aux limites hydrodynamique influence le débit, d'autant plus que le système est confiné à des tailles de l'ordre de la longueur de glissement. Une telle approche nécessite d'une part de mesurer précisément débits et pressions, et d'autre part de comprendre et quantifier l'ensemble des phénomènes qui régissent les écoulements. Lorsqu'on travaille en microfluidique avec les matériaux standards et que l'on tente confiner les systèmes à des tailles de l'ordre du micron, il est

un effet à ne pas négliger: le couplage élastohydrodynamique entre le canal et l'écoulement [6]. Nous proposons maintenant une étude de ce phénomène.

Pour ces expériences d'élastohydrodynamique, réalisées avec de l'eau pure, des mesures en temps réel du débit et de la pression sont réalisées à l'entrée du canal avec des capteurs commerciaux. Le montage est schématisé en figure 6.4 (a). Le réponse du système est mesurée de façon dynamique alors que la pression d'entrée p_{in} est subitement abaissée de $\delta p_{in} \ll p_{in}$. L'expérience est réalisée dans les canaux de longueur $L = 4$ cm, de hauteur $h_0 = 5$ µm et de largeur $w = 200$, 500, 1000 et 2000 µm.

On note $p_{in}(t)$ la pression imposée, et $q(t)$ et $p_0(t)$ le débit et la pression mesurés en entrée de canal; t désigne ici le temps. Des exemples de signaux expérimentaux sont montrés en figure 6.4 (b). L'équilibre est subitement rompu, le système relaxe de façon exponentielle vers un nouvel état stationnaire. On note τ_t le temps caractéristique de décroissance de l'exponentielle, mesuré par un ajustement des données, et $p_{0,\infty}$ et q_∞ les valeurs plateau respectives de p_0 et q. Les principales observations sont les suivantes: la relation entre $p_{0,\infty}$ et q_∞ est non-linéaire, et τ_t diminue avec la pression.

Ces observations peuvent être rationalisées en invoquant la déformation de la puce faite en polydiméthylsiloxane (PDMS), un élastomère transparent répandu en microfluidique, sous l'effet de la pression appliquée. Nous proposons maintenant une modélisation de ce phénomène. Dans la limite unidimensionnelle et pour une réponse élastique du PDMS, la variation de hauteur du canal $h(x,t) - h_0$ (x désigne la direction de l'écoulement) sera proportionnelle à p_0. Or la théorie de Poiseuille pour les écoulements microfluidiques prévoit que la ré-

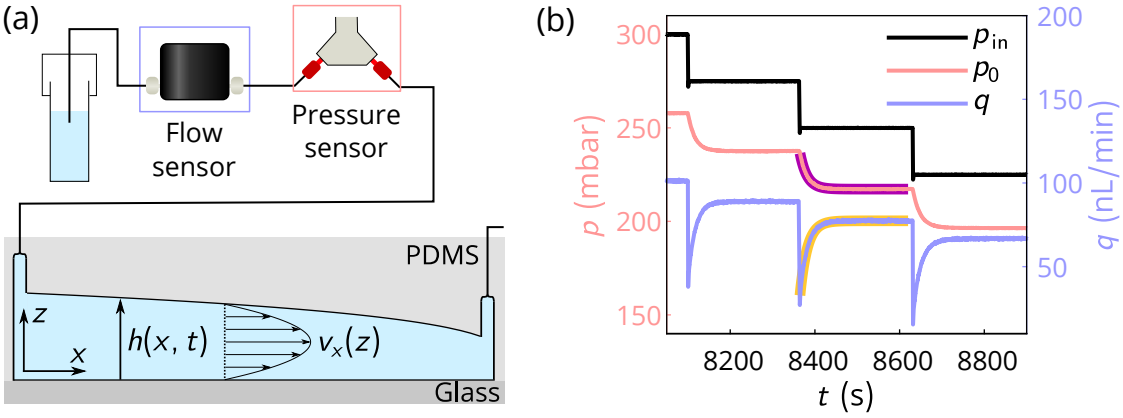

Figure 6.4: (a) Schéma du montage microfluidique pour la mesure de pression et de débit. (b) Échantillon de signaux temporels pour p_{in}, p_0 et q. Les traits épais représentent l'ajustement exponentiel des données.

sistance hydraulique d'une puce – le rapport pression/débit par analogie avec la loi d'Ohm – décroit fortement avec h. L'effet d'une augmentation de pression sur le débit est donc double: d'une part la force motrice de l'écoulement augmente, et d'autre part la résistance diminue. Cette vision explique qualitativement la caractère super-linéaire de la relation pression-débit. D'autre part la déformation élastique de la puce a pour effet d'augmenter le volume interne du canal. De la même manière qu'un condensateur stockant des charges électriques induit une relaxation exponentielle dans un circuit RC, stocker du fluide dans une puce déformable est à l'origine de la relaxation du système en un temps fini.

Pour rationaliser quantitativement les résultats expérimentaux, l'analogie électrique avec des résistances ohmiques et des condensateurs ne suffit pas. Le modèle que nous avons développé se base sur l'équation de lubrification de Reynolds, l'élasticité locale du PDMS, et prends en compte l'effet des capteurs de pression et de débit. Les premières étapes du raisonnement sont explicitées ci-dessous, mais l'entièreté de la théorie de sera pas développée ici. On note respectivement $h(x, t)$ et $p(x, t)$ la hauteur et la pression locale dans le canal. Le premier ingrédient de la modélisation est l'équation de Reynolds, qui est issue de l'équation Stokes pour la quantité de mouvement, et de la conservation du volume [2]:

$$\frac{\partial h}{\partial t} = \frac{1}{12\eta}\frac{\partial}{\partial x}\left(h^3\frac{\partial p}{\partial x}\right). \tag{6.2}$$

D'autre part, nous utilisons un modèle d'élasticité locale pour décrire la réponse linéaire du PDMS:

$$h(x, t) = h_0\left(1 + \frac{p(x, t)w}{E^* h_0}\right), \tag{6.3}$$

où E^* est une constante d'élasticité, égale en ordre de grandeur au module d'Young et qui peut être calculée dans le cadre de la mécanique des milieux continus [166]. En combinant ces deux équations on obtient l'équation élasohydrodynamique constitutive pour le champs de pression:

$$\frac{\partial p}{\partial t} = \frac{E^* h_0^3}{12\eta w}\frac{\partial}{\partial x}\left[\left(1 + \frac{pw}{E^* h_0}\right)^3\frac{\partial p}{\partial x}\right]. \tag{6.4}$$

Cette equation fait apparaitre une pression caractéristique $p^* = E^* h_0/w$ et un temps caractéristique $\tau_c = 12\eta L^2/h_0^2 p^*$. On peut aussi définir un débit caractéristique $q^* = p^*/r_c$ ou $r_c = 12\eta L/w h_0^3$ est la résistance de la puce non déformée.

Cette equation peut être résolue en régime stationnaire, on trouve alors une relation polynomiale d'ordre 4 entre pression et débit:

$$\frac{q_\infty}{q^*} = \frac{1}{4}\left[\left(1 + \frac{p_{0,\infty}}{p^*}\right)^4 - 1\right] \tag{6.5}$$

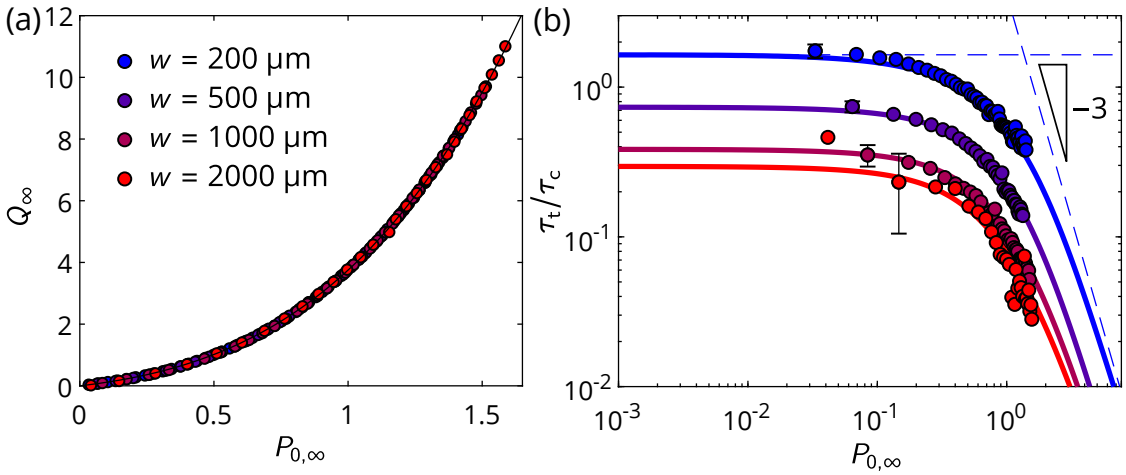

Figure 6.5: (a) Courbe adimensionnée du débit en fonction de la pression d'entrée. Les cercles sont les données expérimentales pour quatre microcanaux de différentes largeurs, et la ligne représente l'équation 6.5. (b) Temps de relaxation expérimentaux normalisé en fonction de la pression d'entrée adimensionnée pour les quatre même canaux. Les traits pleins représentent les prédictions de la théorie élastohydrodynamique, et les traits pointillés montrent le comportements asymptotique associé.

Les paramètres q^* et p^* sont des paramètre d'ajustement du modèle.

La figure 6.5 (a) montre, à l'état stationnaire le débit adimentionnée $Q_\infty = q_\infty/q^*$ en fonction de la pression d'entrée adimentionnée $P_{0,\infty} = p_{0,\infty}/p^*$ pour quatre puces de différentes largeurs. Toutes les données suivent bien l'équation 6.5, prouvant ainsi la validité du modèle à l'état stationnaire.

Pour résoudre le problème dynamique, et rationaliser la dépendance de τ_t en $p_{0,\infty}$ il faut une condition aux limites à l'entrée de la puce. La présence des capteurs rend cette dernière non triviale. En modélisant le capteur de débit comme une résistance idéale et le capteur de pression comme un condensateur, on peut résoudre le problème semi-analytiquement, en faisant une analyse perturbative valable dans la limite des petits changements de pression. La résolution fait néanmoins appel à la résolution numérique d'une équation. Le comportement asymptotique peut cependant être compris par des arguments physiques. Aux basses pressions, le temps de relaxation ne dépend pas de la pression, alors qu'aux fortes pressions, ce dernier décroit comme $p_{0,\infty}^{-3}$. Les résultats expérimentaux ainsi que la solution théorique du problème sont montrés en figure 6.5 (b). Pour les quatre puces testées le modèle capture bien le temps de relaxation en fonction de la pression d'entrée.

Le modèle que nous avons développé propose un cadre pour expliquer à

l'échelle globale le couplage élastohydrodynamique dans les canaux flexibles. Avec l'aide de celui-ci nous avons pu rationaliser les données expérimentales de mesure de pression et de débit dans des puces microfluidiques, à la fois en régime stationnaire et sur les aspects dynamiques. Nous pensons que ce travail ouvre la voie vers la compréhension des écoulements dans les systèmes plus complexes comme les réseaux de canaux flexibles.

6.4 Perspectives et conclusion

Les études décrites ci-dessus ont montré comment la microscopie TIRF permet d'étudier de façon locale des écoulements de fluides complexes dans les milieux confinés. De façon complémentaire, la mesure de la pression et du débit dans un microcanal permet de comprendre le couplage élastohydrodynamique dans ces systèmes, un phénomène qui est d'importance majeure sur l'écoulement à l'échelle globale. La mesures simultanées en microscopie TIRF et en débitmétrie représente un défi expérimental. Un protocole est proposé et appliqué à la mesure dynamique de la couche absorbée dans des écoulements de HPAM en présence sel. Les premiers résultats sont encourageants, mais les données de vélocimétrie et de débimétrie sont quantitativement en désaccord. Des expériences plus approfondies permettraient d'améliorer la méthode en vue d'une étude plus systématique du comportement des solutions de polymères aux interfaces de façon dynamique.

Bibliography

[1] Etienne Guyon, Jean-Pierre Hulin, Luc Petit, and Catalin D Mitescu. *Physical hydrodynamics*. Oxford University Press, 2015.

[2] Alexander Oron, Stephen H Davis, and S George Bankoff. Long-scale evolution of thin liquid films. *Reviews of modern physics*, 69(3):931, 1997.

[3] Niels Asger Mortensen, Fridolin Okkels, and Henrik Bruus. Reexamination of hagen-poiseuille flow: Shape dependence of the hydraulic resistance in microchannels. *Physical Review E*, 71(5):057301, 2005.

[4] Kwang W. Oh, Kangsun Lee, Byungwook Ahn, and Edward P. Furlani. Design of pressure-driven microfluidic networks using electric circuit analogy. *Lab Chip*, 12:515–545, 2012.

[5] Daniel J Preston, Philipp Rothemund, Haihui Joy Jiang, Markus P Nemitz, Jeff Rawson, Zhigang Suo, and George M Whitesides. Digital logic for soft devices. *Proceedings of the National Academy of Sciences*, 116(16):7750–7759, 2019.

[6] Ivan C Christov. Soft hydraulics: from newtonian to complex fluid flows through compliant conduits. *Journal of Physics: Condensed Matter*, 2021.

[7] Thomas Gervais, Jamil El-Ali, Axel Günther, and Klavs F Jensen. Flow-induced deformation of shallow microfluidic channels. *Lab on a Chip*, 6(4):500–507, 2006.

[8] Ivan C Christov, Vincent Cognet, Tanmay C Shidhore, and Howard A Stone. Flow rate–pressure drop relation for deformable shallow microfluidic channels. *Journal of Fluid Mechanics*, 841:267–286, 2018.

[9] George Gabriel Stokes et al. On the effect of the internal friction of fluids on the motion of pendulums. 1851.

[10] Rep Kubo. The fluctuation-dissipation theorem. *Reports on progress in physics*, 29(1):255, 1966.

[11] Michael Rubinstein, Ralph H Colby, et al. *Polymer physics*, volume 23. Oxford university press New York, 2003.

[12] Pierre-Gilles De Gennes. *Scaling concepts in polymer physics*. Cornell university press, 1979.

[13] Paul J Flory. *Principles of polymer chemistry*. Cornell university press, 1953.

[14] M Daoud, JP Cotton, B Farnoux, Gerard Jannink, G Sarma, H Benoit, C Duplessix, Cl Picot, and PG De Gennes. Solutions of flexible polymers. neutron experiments and interpretation. *Macromolecules*, 8(6):804–818, 1975.

[15] JP Cotton, M Nierlich, F Boue, M Daoud, B Farnoux, G Jannink, R Duplessix, and C Picot. Experimental determination of the temperature–concentration diagram of flexible polymer solutions by neutron scattering. *The Journal of Chemical Physics*, 65(3):1101–1108, 1976.

[16] B Farnoux, F Boue, JP Cotton, M Daoud, G Jannink, M Nierlich, and PG De Gennes. Cross-over in polymer solutions. *Journal de physique*, 39(1):77–86, 1978.

[17] Paul J Flory. The configuration of real polymer chains. *The Journal of Chemical Physics*, 17(3):303–310, 1949.

[18] Andrey V Dobrynin, Ralph H Colby, and Michael Rubinstein. Scaling theory of polyelectrolyte solutions. *Macromolecules*, 28(6):1859–1871, 1995.

[19] Rod Cross. Elastic and viscous properties of silly putty. *American Journal of Physics*, 80(10):870–875, 2012.

[20] Kwang Soo Cho. Viscoelasticity of polymers. In *Springer Series in Materials Science*, pages 437–457. Springer, 2016.

[21] Nicole Heymans and J-C Bauwens. Fractal rheological models and fractional differential equations for viscoelastic behavior. *Rheologica acta*, 33(3):210–219, 1994.

[22] Moumita Dasgupta, Bin Liu, Henry C Fu, Michael Berhanu, Kenneth S Breuer, Thomas R Powers, and Arshad Kudrolli. Speed of a swimming sheet in newtonian and viscoelastic fluids. *Physical Review E*, 87(1):013015, 2013.

[23] Maurice L Huggins. The viscosity of dilute solutions of long-chain molecules. iv. dependence on concentration. *Journal of the American Chemical Society*, 64(11):2716–2718, 1942.

[24] David G Thomas. Transport characteristics of suspension: Viii. a note on the viscosity of newtonian suspensions of uniform spherical particles. *Journal of colloid science*, 20(3):267–277, 1965.

[25] Ralph H Colby, DC Boris, WE Krause, and S Dou. Shear thinning of unentangled flexible polymer liquids. *Rheologica acta*, 46(5):569–575, 2007.

[26] Bi-min Zhang Newby, Manoj K Chaudhury, and Hugh R Brown. Macroscopic evidence of the effect of interfacial slippage on adhesion. *Science*, 269(5229):1407–1409, 1995.

[27] Bi-min Zhang Newby and Manoj K Chaudhury. Effect of interfacial slippage on viscoelastic adhesion. *Langmuir*, 13(6):1805–1809, 1997.

[28] Jean Francois Joanny. Lubrication by molten polymer brushes. *Langmuir*, 8(3):989–995, 1992.

[29] B Vincent. The effect of adsorbed polymers on dispersion stability. *Advances in Colloid and Interface Science*, 4(2-3):193–277, 1974.

[30] Yasufumi Otsubo and Kaoru Umeya. Adsorption of polyacrylamide on silica particles and its effect on the rheological properties of suspensions. *Journal of colloid and interface science*, 95(1):279–282, 1983.

[31] P Auroy, L Auvray, and L Leger. Building of a grafted layer. 1. role of the concentration of free polymers in the reaction bath. *Macromolecules*, 24(18):5158–5166, 1991.

[32] Heather S Davies, Delphine Débarre, Nouha El Amri, Claude Verdier, Ralf P Richter, and Lionel Bureau. Elastohydrodynamic lift at a soft wall. *Physical review letters*, 120(19):198001, 2018.

[33] Morton M Denn. Extrusion instabilities and wall slip. *Annual Review of Fluid Mechanics*, 33(1):265–287, 2001.

[34] Howard A Barnes. A review of the slip (wall depletion) of polymer solutions, emulsions and particle suspensions in viscometers: its cause, character, and cure. *Journal of Non-Newtonian Fluid Mechanics*, 56(3):221–251, 1995.

[35] T Kiljański. A method for correction of the wall-slip effect in a couette rheometer. *Rheologica acta*, 28(1):61–64, 1989.

[36] Halil Gevgilili and Dilhan M Kalyon. Step strain flow: Wall slip effects and other error sources. *Journal of Rheology*, 45(2):467–475, 2001.

[37] CLMH Navier. Mémoire sur les lois du mouvement des fluides. *Mémoires de l'Académie Royale des Sciences de l'Institut de France*, 6(1823):389–440, 1823.

[38] David M Huang, Christian Sendner, Dominik Horinek, Roland R Netz, and Lydéric Bocquet. Water slippage versus contact angle: A quasiuniversal relationship. *Physical review letters*, 101(22):226101, 2008.

[39] Lydéric Bocquet and Elisabeth Charlaix. Nanofluidics, from bulk to interfaces. *Chemical Society Reviews*, 39(3):1073–1095, 2010.

[40] Eric Lauga, Michael P Brenner, and Howard A Stone. Microfluidics: the no-slip boundary condition. *arXiv preprint cond-mat/0501557*, 2005.

[41] Chiara Neto, Drew R Evans, Elmar Bonaccurso, Hans-Jürgen Butt, and Vincent SJ Craig. Boundary slip in newtonian liquids: a review of experimental studies. *Reports on progress in physics*, 68(12):2859, 2005.

[42] Pierre Joseph, Cecile Cottin-Bizonne, J-M Benoit, Christophe Ybert, Catherine Journet, Patrick Tabeling, and Lyderic Bocquet. Slippage of water past superhydrophobic carbon nanotube forests in microchannels. *Physical review letters*, 97(15):156104, 2006.

[43] Choongyeop Lee, Chang-Hwan Choi, et al. Structured surfaces for a giant liquid slip. *Physical review letters*, 101(6):064501, 2008.

[44] Savvas G Hatzikiriakos. Slip mechanisms in complex fluid flows. *Soft Matter*, 11(40):7851–7856, 2015.

[45] Michel Cloitre and Roger T Bonnecaze. A review on wall slip in high solid dispersions. *Rheologica Acta*, 56(3):283–305, 2017.

[46] Marceau Hénot, Eric Drockenmuller, Liliane Léger, and Frédéric Restagno. Friction of polymers: from pdms melts to pdms elastomers. *ACS Macro Letters*, 7(1):112–115, 2018.

[47] L Léger, H Hervet, G Massey, and E Durliat. Wall slip in polymer melts. *Journal of Physics: Condensed Matter*, 9(37):7719, 1997.

[48] Pierre-Gilles De Gennes. Viscometric flows of tangled polymers. *Comptes Rendus Hebdomadaires Des Seances De L Academie Des Sciences Serie B*, 288(14):219–220, 1979.

[49] Pierre-Gilles De Gennes. Reptation of a polymer chain in the presence of fixed obstacles. *The journal of chemical physics*, 55(2):572–579, 1971.

[50] Oliver Bäumchen, Renate Fetzer, and Karin Jacobs. Reduced interfacial entanglement density affects the boundary conditions of polymer flow. *Physical review letters*, 103(24):247801, 2009.

[51] Marceau Hénot, Marion Grzelka, Jian Zhang, Sandrine Mariot, Iurii Antoniuk, Eric Drockenmuller, Liliane Léger, and Frédéric Restagno. Temperature-controlled slip of polymer melts on ideal substrates. *Physical Review Letters*, 121(17):177802, 2018.

[52] Joshua D McGraw, Oliver Bäumchen, Mischa Klos, Sabrina Haefner, Matthias Lessel, Sebastian Backes, and Karin Jacobs. Nanofluidics of thin polymer films: Linking the slip boundary condition at solid–liquid interfaces to macroscopic pattern formation and microscopic interfacial properties. *Advances in colloid and interface science*, 210:13–20, 2014.

[53] F Brochard and PG De Gennes. Shear-dependent slippage at a polymer/solid interface. *Langmuir*, 8(12):3033–3037, 1992.

[54] Vijay Mhetar and LA Archer. Slip in entangled polymer melts. 1. general features. *Macromolecules*, 31(24):8607–8616, 1998.

[55] Mark Ilton, Thomas Salez, Paul D Fowler, Marco Rivetti, Mohammed Aly, Michael Benzaquen, Joshua D McGraw, Elie Raphaël, Kari Dalnoki-Veress, and Oliver Bäumchen. Adsorption-induced slip inhibition for polymer melts on ideal substrates. *Nature communications*, 9(1):1–7, 2018.

[56] Pierre-Gilles De Gennes. Polymer solutions near an interface. adsorption and depletion layers. *Macromolecules*, 14(6):1637–1644, 1981.

[57] H Bessaies-Bey, J Fusier, Simon Harrisson, Mathias Destarac, S Jouenne, N Passade-Boupat, F Lequeux, J-B d'Espinose de Lacaillerie, and N Sanson. Impact of polyacrylamide adsorption on flow through porous siliceous materials: State of the art, discussion and industrial concern. *Journal of colloid and interface science*, 531:693–704, 2018.

[58] Philip Geoffrey Saffman and Geoffrey Ingram Taylor. The penetration of a fluid into a porous medium or hele-shaw cell containing a more viscous liquid. *Proceedings of the Royal Society of London. Series A. Mathematical and Physical Sciences*, 245(1242):312–329, 1958.

[59] George M Homsy. Viscous fingering in porous media. *Annual review of fluid mechanics*, 19(1):271–311, 1987.

[60] Yoshikimi Uyama, Koichi Kato, and Yoshito Ikada. Surface modification of polymers by grafting. *Grafting/Characterization Techniques/Kinetic Modeling*, pages 1–39, 1998.

[61] H Müller-Mohnssen, D Weiss, and A Tippe. Concentration dependent changes of apparent slip in polymer solution flow. *Journal of Rheology*, 34(2):223–244, 1990.

[62] Harry J Ploehn, William B Russel, and Carol K Hall. Self-consistent field model of polymer adsorption: generalized formulation and ground-state solution. *Macromolecules*, 21(4):1075–1085, 1988.

[63] Marion Grzelka, Iurii Antoniuk, Eric Drockenmuller, Alexis Chennevière, Liliane Léger, and Frédéric Restagno. Slip and friction mechanisms at polymer semi-dilute solutions/solid interfaces. *Macromolecules*, 54(10):4910–4917, 2021.

[64] NV Churaev, VD Sobolev, and AN Somov. Slippage of liquids over lyophobic solid surfaces. *Journal of Colloid and Interface Science*, 97(2):574–581, 1984.

[65] J-T Cheng and N Giordano. Fluid flow through nanometer-scale channels. *Physical review E*, 65(3):031206, 2002.

[66] Chang-Hwan Choi, K Johan A Westin, and Kenneth S Breuer. Apparent slip flows in hydrophilic and hydrophobic microchannels. *Physics of fluids*, 15(10):2897–2902, 2003.

[67] Amandine Cuenca and Hugues Bodiguel. Submicron flow of polymer solutions: Slippage reduction due to confinement. *Physical review letters*, 110(10):108304, 2013.

[68] Saurabh Mishra, Achinta Bera, and Ajay Mandal. Effect of polymer adsorption on permeability reduction in enhanced oil recovery. *Journal of Petroleum Engineering*, 2014, 2014.

[69] Patrick EG Idahosa, Gbenga Folorunso Oluyemi, MB Oyeneyin, and Radhakrishna Prabhu. Rate-dependent polymer adsorption in porous media. *Journal of petroleum science and engineering*, 143:65–71, 2016.

[70] Olga I Vinogradova. Drainage of a thin liquid film confined between hydrophobic surfaces. *Langmuir*, 11(6):2213–2220, 1995.

[71] Chloé Barraud, Benjamin Cross, Cyril Picard, Fréderic Restagno, Lilianne Léger, and Elisabeth Charlaix. Large slippage and depletion layer at the polyelectrolyte/solid interface. *Soft matter*, 15(31):6308–6317, 2019.

[72] Gerd Binnig, Calvin F Quate, and Ch Gerber. Atomic force microscope. *Physical review letters*, 56(9):930, 1986.

[73] Jacob N Israelachvili and GE Adams. Direct measurement of long range forces between two mica surfaces in aqueous kno3 solutions. *Nature*, 262(5571):774–776, 1976.

[74] J Israelachvili, Y Min, M Akbulut, A Alig, G Carver, W Greene, K Kristiansen, E Meyer, N Pesika, K Rosenberg, et al. Recent advances in the surface forces apparatus (sfa) technique. *Reports on Progress in Physics*, 73(3):036601, 2010.

[75] Dirk Peschka, Sabrina Haefner, Ludovic Marquant, Karin Jacobs, Andreas Münch, and Barbara Wagner. Signatures of slip in dewetting polymer films. *Proceedings of the National Academy of Sciences*, 116(19):9275–9284, 2019.

[76] Derek C Tretheway and Carl D Meinhart. Apparent fluid slip at hydrophobic microchannel walls. *Physics of fluids*, 14(3):L9–L12, 2002.

[77] Pierre Joseph and Patrick Tabeling. Direct measurement of the apparent slip length. *Physical Review E*, 71(3):035303, 2005.

[78] Marceau Hénot, Alexis Chennevière, Eric Drockenmuller, Liliane Léger, and Frédéric Restagno. Comparison of the slip of a pdms melt on weakly adsorbing surfaces measured by a new photobleaching-based technique. *Macromolecules*, 50(14):5592–5598, 2017.

[79] Daniel Axelrod. Cell-substrate contacts illuminated by total internal reflection fluorescence. *The Journal of cell biology*, 89(1):141–145, 1981.

[80] Daniel Axelrod, Thomas P Burghardt, and Nancy L Thompson. Total internal reflection fluorescence. *Annual review of biophysics and bioengineering*, 13(1):247–268, 1984.

[81] Yan Fu, Peter W Winter, Raul Rojas, Victor Wang, Matthew McAuliffe, and George H Patterson. Axial superresolution via multiangle tirf microscopy with sequential imaging and photobleaching. *Proceedings of the National Academy of Sciences*, 113(16):4368–4373, 2016.

[82] Yicong Wu and Hari Shroff. Faster, sharper, and deeper: structured illumination microscopy for biological imaging. *Nature methods*, 15(12):1011–1019, 2018.

[83] Katie A Rose, Mehdi Molaei, Michael J Boyle, Daeyeon Lee, John C Crocker, and Russell J Composto. Particle tracking of nanoparticles in soft matter. *Journal of Applied Physics*, 127(19):191101, 2020.

[84] Stacey G Bike and Dennis C Prieve. Measurements of double-layer repulsion for slightly overlapping counterion clouds. *International journal of multiphase flow*, 16(4):727–740, 1990.

[85] R Burchett Liebert and Dennis C Prieve. Species-specific long range interactions between receptor/ligand pairs. *Biophysical journal*, 69(1):66–73, 1995.

[86] Dennis C Prieve. Measurement of colloidal forces with tirm. *Advances in Colloid and Interface Science*, 82(1-3):93–125, 1999.

[87] M Yoda and Yutaka Kazoe. Dynamics of suspended colloidal particles near a wall: Implications for interfacial particle velocimetry. *Physics of Fluids*, 23(11):111301, 2011.

[88] Alexandre Vilquin, Vincent Bertin, Pierre Soulard, Gabriel Guyard, Elie Raphaël, Frederic Restagno, Thomas Salez, and Joshua D McGraw. Time dependence of advection-diffusion coupling for nanoparticle ensembles. *Physical Review Fluids*, 6(6):064201, 2021.

[89] C Zettner and M Yoda. Particle velocity field measurements in a near-wall flow using evanescent wave illumination. *Experiments in fluids*, 34(1):115–121, 2003.

[90] Zhenzhen Li, Loïc D'eramo, Choongyeop Lee, Fabrice Monti, Marc Yonger, Patrick Tabeling, Benjamin Chollet, Bruno Bresson, and Yvette Tran. Near-wall nanovelocimetry based on total internal reflection fluorescence with continuous tracking. *Journal of Fluid Mechanics*, 766:147–171, 2015.

[91] Minami Yoda. Super-resolution imaging in fluid mechanics using new illumination approaches. *Annual Review of Fluid Mechanics*, 52:369–393, 2020.

[92] Jeff W Lichtman and José-Angel Conchello. Fluorescence microscopy. *Nature methods*, 2(12):910–919, 2005.

[93] Bonnie O Leung and Keng C Chou. Review of super-resolution fluorescence microscopy for biology. *Applied spectroscopy*, 65(9):967–980, 2011.

[94] Yaron M Sigal, Ruobo Zhou, and Xiaowei Zhuang. Visualizing and discovering cellular structures with super-resolution microscopy. *Science*, 361(6405):880–887, 2018.

[95] Tony Wilson et al. *Confocal microscopy*, volume 426. Academic press London, 1990.

[96] Denis Semwogerere and Eric R Weeks. Confocal microscopy. *Encyclopedia of biomaterials and biomedical engineering*, 23:1–10, 2005.

[97] Kenneth N Fish. Total internal reflection fluorescence (tirf) microscopy. *Current protocols in cytometry*, 50(1):12–18, 2009.

[98] Jeffrey S Guasto and Kenneth S Breuer. Simultaneous, ensemble-averaged measurement of near-wall temperature and velocity in steady micro-flows using single quantum dot tracking. *Experiments in fluids*, 45(1):157–166, 2008.

[99] KD Kihm, Arindam Banerjee, CK Choi, and T Takagi. Near-wall hindered brownian diffusion of nanoparticles examined by three-dimensional ratiometric total internal reflection fluorescence microscopy (3-d r-tirfm). *Experiments in Fluids*, 37(6):811–824, 2004.

[100] Paul R Selvin and Taekjip Ha. *Single-molecule techniques*. Cold Spring Harbor Laboratory Press, 2008.

[101] Xu Zheng, Fei Shi, and Zhanhua Silber-Li. Study on the statistical intensity distribution (sid) of fluorescent nanoparticles in tirfm measurement. *Microfluidics and Nanofluidics*, 22(11):1–10, 2018.

[102] Andreas Manz, D Jed Harrison, Elisabeth MJ Verpoorte, James C Fettinger, Aran Paulus, Hans Lüdi, and H Michael Widmer. Planar chips technology for miniaturization and integration of separation techniques into monitoring systems: capillary electrophoresis on a chip. *Journal of Chromatography A*, 593(1-2):253–258, 1992.

[103] HA Stone, Abraham D Stroock, and A Ajdari. Engineering flows in small devices. *Annual review of fluid mechanics*, 36(1):381–411, 2004.

[104] George M Whitesides. The origins and the future of microfluidics. *nature*, 442(7101):368–373, 2006.

[105] Ali Abou-Hassan, Olivier Sandre, and Valérie Cabuil. Microfluidics in inorganic chemistry. *Angewandte Chemie International Edition*, 49(36):6268–6286, 2010.

[106] Linas Mazutis, John Gilbert, W Lloyd Ung, David A Weitz, Andrew D Griffiths, and John A Heyman. Single-cell analysis and sorting using droplet-based microfluidics. *Nature protocols*, 8(5):870–891, 2013.

[107] Curtis D Chin, Tassaneewan Laksanasopin, Yuk Kee Cheung, David Steinmiller, Vincent Linder, Hesam Parsa, Jennifer Wang, Hannah Moore, Robert Rouse, Gisele Umviligihozo, et al. Microfluidics-based diagnostics of infectious diseases in the developing world. *Nature medicine*, 17(8):1015–1019, 2011.

[108] Clement Kleinstreuer, Jie Li, and Junemo Koo. Microfluidics of nano-drug delivery. *International Journal of Heat and Mass Transfer*, 51(23-24):5590–5597, 2008.

[109] Younan Xia and George M Whitesides. Soft lithography. *Angewandte Chemie International Edition*, 37(5):550–575, 1998.

[110] Jessamine Ng Lee, Cheolmin Park, and George M Whitesides. Solvent compatibility of poly (dimethylsiloxane)-based microfluidic devices. *Analytical chemistry*, 75(23):6544–6554, 2003.

[111] Yun Seok Heo, Lourdes M Cabrera, Jonathan W Song, Nobuyuki Futai, Yi-Chung Tung, Gary D Smith, and Shuichi Takayama. Characterization and resolution of evaporation-mediated osmolality shifts that constrain microfluidic cell culture in poly (dimethylsiloxane) devices. *Analytical chemistry*, 79(3):1126–1134, 2007.

[112] Holger Becker and Laurie E Locascio. Polymer microfluidic devices. *Talanta*, 56(2):267–287, 2002.

[113] Jihong Hwang, Young Hak Cho, Min Soo Park, and Bo Hyun Kim. Microchannel fabrication on glass materials for microfluidic devices. *International Journal of Precision Engineering and Manufacturing*, 20(3):479–495, 2019.

[114] Rodrigo Martinez-Duarte and Marc Madou. Su-8 photolithography and its impact on microfluidics. *Microfluidics and Nanofluidics Handbook*, (2006):231–268, 2011.

[115] David C Duffy, J Cooper McDonald, Olivier JA Schueller, and George M Whitesides. Rapid prototyping of microfluidic systems in poly (dimethylsiloxane). *Analytical chemistry*, 70(23):4974–4984, 1998.

[116] Maziar Raissi, Alireza Yazdani, and George Em Karniadakis. Hidden fluid mechanics: Learning velocity and pressure fields from flow visualizations. *Science*, 367(6481):1026–1030, 2020.

[117] Wolfram Von Funck, Tino Weinkauf, Holger Theisel, and Hans-Peter Seidel. Smoke surfaces: An interactive flow visualization technique inspired by real-world flow experiments. *IEEE Transactions on Visualization and Computer Graphics*, 14(6):1396–1403, 2008.

[118] H H Bruun. Hot-wire anemometry: Principles and signal analysis. *Measurement Science and Technology*, 7(10), 1996.

[119] JB Abbiss, TW Chubb, and ER Pike. Laser doppler anemometry. *Optics & Laser Technology*, 6(6):249–261, 1974.

[120] Lara Adrian, Ronald J Adrian, and Jerry Westerweel. *Particle image velocimetry*. Number 30. Cambridge university press, 2011.

[121] HG Maas, A Gruen, and D Papantoniou. Particle tracking velocimetry in three-dimensional flows. *Experiments in fluids*, 15(2):133–146, 1993.

[122] Christian E Willert and Morteza Gharib. Digital particle image velocimetry. *Experiments in fluids*, 10(4):181–193, 1991.

[123] David Sinton. Microscale flow visualization. *Microfluidics and Nanofluidics*, 1(1):2–21, 2004.

[124] Ralph Lindken, Massimiliano Rossi, Sebastian Große, and Jerry Westerweel. Micro-particle image velocimetry (μpiv): recent developments, applications, and guidelines. *Lab on a Chip*, 9(17):2551–2567, 2009.

[125] Christian J Kähler, Sven Scharnowski, and Christian Cierpka. On the uncertainty of digital piv and ptv near walls. *Experiments in fluids*, 52(6):1641–1656, 2012.

[126] GK406082 Batchelor. Brownian diffusion of particles with hydrodynamic interaction. *Journal of Fluid Mechanics*, 74(1):1–29, 1976.

[127] John C. Crocker, bpass, 1997.
(https://github.com/eliasds/Matlab/blob/master/tracking/georgetown.

[128] Bo Zhang, Josiane Zerubia, and Jean-Christophe Olivo-Marin. Gaussian approximations of fluorescence microscope point-spread function models. *Applied optics*, 46(10):1819–1829, 2007.

[129] Jean-Yves Tinevez, simpletracker, 2012. (https://github.com/tinevez/simpletracker).

[130] Emmanuelle Read, Aymeric Guinaudeau, D James Wilson, Arnaud Cadix, Frédéric Violleau, and Mathias Destarac. Low temperature raft/madix gel polymerisation: access to controlled ultra-high molar mass polyacrylamides. *Polymer Chemistry*, 5(7):2202–2207, 2014.

[131] H Bessaies-Bey, J Fusier, M Hanafi, S Zhang, Mathias Destarac, S Jouenne, N Passade-Boupat, F Lequeux, J-B d'Espinose de Lacaillerie, and N Sanson. Competitive adsorption of pam and hpam on siliceous material. *Colloids and Surfaces A: Physicochemical and Engineering Aspects*, 579:123673, 2019.

[132] S Jouenne and B Levache. Universal viscosifying behavior of acrylamide-based polymers used in enhanced oil recovery. *Journal of Rheology*, 64(5):1295–1313, 2020.

[133] William W Graessley. The entanglement concept in polymer rheology. *The entanglement concept in polymer rheology*, pages 1–179, 1974.

[134] Gabriel Guyard, Alexandre Vilquin, Nicolas Sanson, Stéphane Jouenne, Frederic Restagno, and Joshua D McGraw. Near-surface rheology and hydrodynamic boundary condition of semi-dilute polymer solutions. *Soft Matter*, 17(14):3765–3774, 2021.

[135] Yongan Gu and Dongqing Li. The ζ-potential of glass surface in contact with aqueous solutions. *Journal of colloid and interface science*, 226(2):328–339, 2000.

[136] Sven H Behrens and David G Grier. The charge of glass and silica surfaces. *The Journal of Chemical Physics*, 115(14):6716–6721, 2001.

[137] Robert Vogel, Anoop K Pal, Siddharth Jambhrunkar, Pragnesh Patel, Sachin S Thakur, Eduardo Reátegui, Harendra S Parekh, Paula Saá, Adonis Stassinopoulos, and Murray F Broom. High-resolution single particle zeta potential characterisation of biological nanoparticles using tunable resistive pulse sensing. *Scientific reports*, 7(1):1–13, 2017.

[138] C Cottin-Bizonne, S Jurine, J Baudry, J Crassous, F Restagno, and E Charlaix. Nanorheology: An investigation of the boundary condition at hydrophobic and hydrophilic interfaces. *The European Physical Journal E*, 9(1):47–53, 2002.

[139] D Lasne, A Maali, Y Amarouchene, L Cognet, Brahim Lounis, and H Kellay. Velocity profiles of water flowing past solid glass surfaces using fluorescent nanoparticles and molecules as velocity probes. *Physical Review Letters*, 100(21):214502, 2008.

[140] Lawrence Korson, Walter Drost-Hansen, and Frank J Millero. Viscosity of water at various temperatures. *The Journal of Physical Chemistry*, 73(1):34–39, 1969.

[141] Madison L Sheely. Glycerol viscosity tables. *Industrial & Engineering Chemistry*, 24(9):1060–1064, 1932.

[142] Arthur Joseph Goldman, Raymond G Cox, and Howard Brenner. Slow viscous motion of a sphere parallel to a plane wall—i motion through a quiescent fluid. *Chemical engineering science*, 22(4):637–651, 1967.

[143] Lay-Theng Lee and P Somasundaran. Adsorption of polyacrylamide on oxide minerals. *Langmuir*, 5(3):854–860, 1989.

[144] Airidas Korolkovas, Cesar Rodriguez-Emmenegger, Andres de los Santos Pereira, Alexis Chenneviere, Frédéric Restagno, Maximilian Wolff, Franz A Adlmann, Andrew JC Dennison, and Philipp Gutfreund. Polymer brush collapse under shear flow. *Macromolecules*, 50(3):1215–1224, 2017.

[145] JF Joanny, L Leibler, and PG De Gennes. Effects of polymer solutions on colloid stability. *Journal of Polymer Science: Polymer Physics Edition*, 17(6):1073–1084, 1979.

[146] Sabrina Jahn, Jasmine Seror, and Jacob Klein. Lubrication of articular cartilage. *Annual review of biomedical engineering*, 18:235–258, 2016.

[147] Malcolm B Jones, GR Fulford, CP Please, DLS McElwain, and MJ Collins. Elastohydrodynamics of the eyelid wiper. *Bulletin of mathematical biology*, 70(2):323–343, 2008.

[148] Karl Perktold and Gerhard Rappitsch. Computer simulation of local blood flow and vessel mechanics in a compliant carotid artery bifurcation model. *Journal of biomechanics*, 28(7):845–856, 1995.

[149] C Alberto Figueroa, Irene E Vignon-Clementel, Kenneth E Jansen, Thomas JR Hughes, and Charles A Taylor. A coupled momentum method for modeling blood flow in three-dimensional deformable arteries. *Computer methods in applied mechanics and engineering*, 195(41-43):5685–5706, 2006.

[150] Matthias Heil and Andrew L Hazel. Fluid-structure interaction in internal physiological flows. *Annual review of fluid mechanics*, 43:141–162, 2011.

[151] Matthew Hirschhorn, Vakhtang Tchantchaleishvili, Randy Stevens, Joseph Rossano, and Amy Throckmorton. Fluid–structure interaction modeling in cardiovascular medicine–a systematic review 2017–2019. *Medical engineering & physics*, 78:1–13, 2020.

[152] Keunhwan Park, Aude Tixier, Magnus Paludan, Emil Østergaard, Maciej Zwieniecki, and Kaare H Jensen. Fluid-structure interactions enable passive flow control in real and biomimetic plants. *Physical Review Fluids*, 6(12):123102, 2021.

[153] Dongeun Huh, Benjamin D Matthews, Akiko Mammoto, Martín Montoya-Zavala, Hong Yuan Hsin, and Donald E Ingber. Reconstituting organ-level lung functions on a chip. *Science*, 328(5986):1662–1668, 2010.

[154] Johan U Lind, Travis A Busbee, Alexander D Valentine, Francesco S Pasqualini, Hongyan Yuan, Moran Yadid, Sung-Jin Park, Arda Kotikian, Alexander P Nesmith, Patrick H Campbell, et al. Instrumented cardiac microphysiological devices via multimaterial three-dimensional printing. *Nature materials*, 16(3):303–308, 2017.

[155] Sheng Xu, Yihui Zhang, Lin Jia, Kyle E Mathewson, Kyung-In Jang, Jeonghyun Kim, Haoran Fu, Xian Huang, Pranav Chava, Renhan Wang, et al. Soft microfluidic assemblies of sensors, circuits, and radios for the skin. *Science*, 344(6179):70–74, 2014.

[156] Joo Chuan Yeo, Chwee Teck Lim, et al. Emergence of microfluidic wearable technologies. *Lab on a Chip*, 16(21):4082–4090, 2016.

[157] Douglas P Holmes, Behrouz Tavakol, Guillaume Froehlicher, and Howard A Stone. Control and manipulation of microfluidic flow via elastic deformations. *Soft Matter*, 9(29):7049–7053, 2013.

[158] Felix J Meigel, Peter Cha, Michael P Brenner, and Karen Alim. Robust increase in supply by vessel dilation in globally coupled microvasculature. *Physical Review Letters*, 123(22):228103, 2019.

[159] E Virot, V Spandan, L Niu, Willem Marinus Van Rees, and L Mahadevan. Elastohydrodynamic scaling law for heart rates. *Physical Review Letters*, 125(5):058102, 2020.

[160] Jason W Rocks, Andrea J Liu, and Eleni Katifori. Hidden topological structure of flow network functionality. *Physical Review Letters*, 126(2):028102, 2021.

[161] James A Weaver, Jessica Melin, Don Stark, Stephen R Quake, and Mark A Horowitz. Static control logic for microfluidic devices using pressure-gain valves. *Nature Physics*, 6(3):218–223, 2010.

[162] Bobak Mosadegh, Chuan-Hsien Kuo, Yi-Chung Tung, Yu-suke Torisawa, Tommaso Bersano-Begey, Hossein Tavana, and Shuichi Takayama. Integrated elastomeric components for autonomous regulation of sequential and oscillatory flow switching in microfluidic devices. *Nature physics*, 6(6):433–437, 2010.

[163] Philip N Duncan, Transon V Nguyen, and Elliot E Hui. Pneumatic oscillator circuits for timing and control of integrated microfluidics. *Proceedings of the National Academy of Sciences*, 110(45):18104–18109, 2013.

[164] Daniel C Leslie, Christopher J Easley, Erkin Seker, James M Karlinsey, Marcel Utz, Matthew R Begley, and James P Landers. Frequency-specific flow control in microfluidic circuits with passive elastomeric features. *Nature Physics*, 5(3):231–235, 2009.

[165] Gabriel Guyard, Frédéric Restagno, and Joshua D McGraw. Elastohydrodynamic relaxation of soft and deformable microchannels. *Physical Review Letters*, 129(20):204501, 2022.

[166] Xiaojia Wang and Ivan C Christov. Theory of the flow-induced deformation of shallow compliant microchannels with thick walls. *Proceedings of the Royal Society A*, 475(2231):20190513, 2019.

[167] Xiaojia Wang and Ivan C Christov. Reduced models of unidirectional flows in compliant rectangular ducts at finite reynolds number. *Physics of Fluids*, 33(10):102004, 2021.

[168] Miao Liu, Jianren Sun, and Quanfang Chen. Influences of heating temperature on mechanical properties of polydimethylsiloxane. *Sensors and Actuators A: Physical*, 151(1):42–45, 2009.

[169] OS Heavens. Optical properties of thin films. *Reports on Progress in Physics*, 23(1):1, 1960.

[170] *NIST Digital Library of Mathematical Functions*. http://dlmf.nist.gov/, Release 1.1.5 of 2022-03-15. F. W. J. Olver, A. B. Olde Daalhuis, D. W. Lozier, B. I.

Schneider, R. F. Boisvert, C. W. Clark, B. R. Miller, B. V. Saunders, H. S. Cohl, and M. A. McClain, eds.

[171] EC Vermolen, MJ Haasterecht, and SK Masalmeh. A systematic study of the polymer visco-elastic effect on residual oil saturation by core flooding. In *SPE EOR Conference at Oil and Gas West Asia*. OnePetro, 2014.

[172] AR Al Hashmi, RS Al Maamari, IS Al Shabibi, AM Mansoor, A Zaitoun, and HH Al Sharji. Rheology and mechanical degradation of high-molecular-weight partially hydrolyzed polyacrylamide during flow through capillaries. *Journal of Petroleum Science and Engineering*, 105:100–106, 2013.

[173] Brian Dincau, Emilie Dressaire, and Alban Sauret. Pulsatile flow in microfluidic systems. *Small*, 16(9):1904032, 2020.

[174] P Tabeling, M Chabert, A Dodge, C Jullien, and F Okkels. Chaotic mixing in cross-channel micromixers. *Philosophical Transactions of the Royal Society of London. Series A: Mathematical, Physical and Engineering Sciences*, 362(1818):987–1000, 2004.

[175] Yousang Yoon, Seonil Kim, Jusin Lee, Jaewoong Choi, Rae-Kwon Kim, Su-Jae Lee, Onejae Sul, and Seung-Beck Lee. Clogging-free microfluidics for continuous size-based separation of microparticles. *Scientific reports*, 6(1):1–8, 2016.

[176] Sarah M McFaul, Bill K Lin, and Hongshen Ma. Cell separation based on size and deformability using microfluidic funnel ratchets. *Lab on a chip*, 12(13):2369–2376, 2012.

[177] Wenfu Zheng, Bo Jiang, Dong Wang, Wei Zhang, Zhuo Wang, and Xingyu Jiang. A microfluidic flow-stretch chip for investigating blood vessel biomechanics. *Lab on a Chip*, 12(18):3441–3450, 2012.

[178] J Murali Krishnan, Abhijit P Deshpande, and PB Sunil Kumar. *Rheology of complex fluids*. Springer, 2010.

[179] Savvas G Hatzikiriakos. Wall slip of molten polymers. *Progress in Polymer Science*, 37(4):624–643, 2012.

[180] F Brochard-Wyart, C Gay, and PG De Gennes. Slippage of polymer melts on grafted surfaces. *Macromolecules*, 29(1):377–382, 1996.

[181] Michael D Graham. Fluid dynamics of dissolved polymer molecules in confined geometries. *Annual Review of Fluid Mechanics*, 43:273–298, 2011.

université PARIS-SACLAY | ÉCOLE DOCTORALE Physique en Île-de-France (PIF)

Title: Near-surface transport of polymer solutions and time-dependent soft microfluidics
Keywords: Polymer solutions, microfluidics, TIRF microscopy, elastohydrodynamics

Abstract: Flows of polyacrylamide (PAM) solutions under micrometric confinement are experimentally studied. By combining microfluidics, evanescent wave microscopy and particle tracking velocimetry, we measure the velocity field within the first few hundred of nanometers in the vicinity of a glass surface. Our measurements allow to simultaneously access the rheological behavior of the sample, and the hydrodynamic boundary condition. While the observed shear-thinning of polymer solutions is consistent with standard measurements, the boundary conditions are shown to be non-trivial and mediated by electric charges. Neutral PAM samples display a chain-sized adsorbed layer, which shifts the no-slip plane accordingly and decreases the effective size of the channel. Conversely, anionic hydrolyzed PAM solutions show apparent slip at the wall, synonymous with permeability increase. The latter was attributed to the presence of a thin low-viscosity lubrication layer close the channel surface, due to electrostatic repulsion of polymer chains.

To further characterize flows at the scale of the microfluidic device, the flow rate and pressure are measured in real time at the inlet of the elastomeric channel. Significant deformations of the conduit cause non-linear flow rate *vs.* pressure relation, and a finite relaxation time upon pressure change, the latter attributed to a volume-storage capacity. We propose an elastohydrodynamic model to quantitatively rationalize these observations, with focus on the dynamical part of the problem. The latter is based on the lubrication equation, the local elastic response of the elastomer, and specifically takes into account the effect of the peripheral sensors.

Finally, and as a perspective, a setup able to simultaneously and dynamically achieve local microscopy and global flow measurement in complex fluids is proposed.

Titre: Transport interfacial de polymères en solution et dynamique en microfluidique déformable
Mots clés: Solutions de polymère, microfluidique, microscopie TIRF, élastohydrodynamique

Résumé: Des écoulements de polyacrylamide (PAM) en solution sont étudiés en confinement micrométrique. En utilisant microfluidique, microscopie à ondes évanescentes, et suivi de particules, nous mesurons le profil de vitesse au voisinage d'une paroi en verre. Ces données permettent d'accéder simultanément à la rhéologie du fluide, et à la condition aux limites hydrodynamique. Tandis que l'on retrouve le comportement rhéofluidifiant standard des solutions de polymères, nous montrons que la condition aux limites est complexe, et gouvernée par des effets électrostatiques. Les polymères neutres s'adsorbent à la paroi, ce qui décale le plan de non-glissement d'une distance comparable à la taille des chaines. Inversement, les PAM hydrolysés, anioniques, présentent un glissement apparent, qui s'interprète par la présence d'une fine couche de faible viscosité proche de l'interface, due à la répulsion polymère/surface.

Pour caractériser plus en détails les écoulements à l'échelle du canal entier, le débit et la pression sont mesurés en temps réel en amont de la puce élastomérique. Des déformations importantes causent une forte non-linéarité entre ces deux quantités, et sont à l'origine d'un temps de relaxation du système lors des changements de pression, attribué à des effets capacitifs. Nous proposons un modèle élastohydrodynamique pour rationaliser quantitativement ces observations, en particulier le comportement dynamique du système. Ce dernier est basé sur l'équation de lubrification, la réponse élastique locale de l'élastomère, et prend en compte les effets des capteurs.

Pour finir, et en guise de perspective, nous proposons un montage pouvant effectuer simultanément et de façon dynamique microscopie locale et mesure de débit dans les fluides complexes.